ABANT IZZET BAYSAL UNIVERSITY

THE GRADUATE SCHOOL OF NATURAL AND APPLIED SCIENCES

DEPARTMENT OF PHYSICS

THE DIFFUSION OF IRON (Fe) IN THE SUPERCONDUCTING MgB_2 POLYCRYSTALLINE SAMPLES

DOCTOR OF PHILOSOPHY

ASAF TOLGA ÜLGEN

BOLU, OCTOBER 2016

APPROVAL OF THE THESIS

THE DIFFUSION OF IRON (Fe) IN THE SUPERCONDUCTING MgB_2 POLYCRYSTALLINE SAMPLES submitted by **ASAF TOLGA ÜLGEN** in partial fullfillment of the requirements for the degree of Doctor of Philosophy in Department of Physics, **Abant Izzet Baysal University** by,

Examining Committee Members	**Signature**
Supervisor Prof. Dr. İbrahim BELENLİ Abant İzzet Baysal University	
Co-Supervisor Prof. Dr. Cabir TERZİOĞLU Abant İzzet Baysal University	
Member Prof. Dr. Ali GENCER Ankara University	
Member Prof. Dr. Osman GÖRÜR Abant İzzet Baysal University	
Member Assoc. Prof. Dr. Özgür ÖZTÜRK Kastamonu University	
Member Assoc. Prof. Dr. Mustafa AKDOĞAN Abant İzzet Baysal University	
Member Assoc. Prof. Dr. Hakan YETİŞ Abant İzzet Baysal University	

OCTOBER 13, 2016

Prof. Dr. Duran KARAKAŞ

Director, **Graduate School of Natural and Applied Sciences**

Dedicated to my lovely wife Canan and precious son Çınar Efe

DECLARATION

I hereby declare that all information in this document has been obtained and presented in accordance with academic rules and ethical conduct. I also declare that, as required by these rules and conduct, I have fully cited and referenced all material and results that are not original to this work.

Asaf Tolga ÜLGEN

ABSTRACT

THE DIFFUSION OF IRON (Fe)
IN THE SUPERCONDUCTING
MgB_2 POLYCRYSTALLINE SAMPLES
PHD THESIS
ASAF TOLGA ÜLGEN
ABANT IZZET BAYSAL UNIVERSITY GRADUATE SCHOOL OF NATURAL AND APPLIED SCIENCES
DEPARTMENT OF PHYSICS
(SUPERVISOR: PROF. DR. İBRAHİM BELENLİ)
(CO-SUPERVISOR: PROF. DR. CABİR TERZİOĞLU)

BOLU, OCTOBER 2016

The main objective of this thesis is to investigate iron (Fe) diffusion into the MgB_2 superconductor bulk samples. Diffusion of Fe has been performed at different sintering temperatures for different sintering time durations. For Fe diffusion, a 50 μm thick Fe layer was coated on MgB_2 by metal evaporation in vacuum. Experimental studies of this thesis are divided in to two parts. In the first part, the Fe diffusion in superconducting MgB_2 samples has been studied over the temperature range of 650-900°C for 1 hour. Fe coating was made on two sets of pelletized bulk samples; either after initial sintering at 800°C/1h (Set 1S) or without initial sintering (Set 1N). Effects of Fe diffusion on the crystal structure and superconducting properties of MgB_2 have been investigated by X-ray diffraction (XRD), scanning electron microscopy (SEM), infrared spectroscopy (IR) and resistivity measurements. Fe diffusion coefficients were determined for both sets from values of lattice parameter *c* and room temperature resistivity. The temperature dependence of the Fe diffusion coefficient in this temperature range is described by the Arrhenius relation. It has been found that the Fe diffusion coefficient increases with increasing sintering temperature, as expected. The plausible explanations for the observed improvement in microstructure and superconducting properties of the samples due to Fe diffusion are discussed. In the second part, coating process

was made on two sets of samples; either after initial sintering at 800°C/1h (Set 2S) or without initial sintering (Set 2N). The Fe diffusion in both sets of superconducting MgB_2 samples has been studied over the time range of 15 minutes, 30 minutes, 1 hour, 2 hours, 4 hours and 8 hours at 900°C temperature. Similar to the first part, effects of Fe diffusion on the crystal structure and superconducting properties of MgB_2 have been investigated by XRD, SEM and resistivity measurements. Fe diffusion coefficients for sintering process were determined from lattice parameter *c* and room temperature resistivity values. It has been found that the Fe diffusion coefficient decreases with increasing sintering time, as expected. Finally, since diffusion coefficient increases with increasing annealing temperature and decreasing annealing time, heat treatment processes for superconductor should be re-considered in the light of these findings. High quality superconductors in the forms of bulk, wire and tape may be produced by sintering at lower temperatures for longer durations if other parameters are optimized.

KEYWORDS: MgB_2 Superconducting Bulk Samples, Fe-diffusion, Temperature Depended Diffusion, Time Depended Diffusion and Activation Energy.

ÖZET

**POLİKRİSTAL MgB_2 SÜPERİLETKEN
ÖRNEKLERDE DEMİR (Fe) DİFÜZYONU
DOKTORA TEZİ
ASAF TOLGA ÜLGEN
ABANT İZZET BAYSAL ÜNİVERSİTESİ FEN BİLİMLERİ
ENSTİTÜSÜ
FİZİK ANABİLİM DALI
(TEZ DANIŞMANI: PROF. DR. İBRAHİM BELENLİ)
(İKİNCİ DANIŞMAN: PROF. DR. CABİR TERZİOĞLU)**

BOLU, EKİM 2016

Bu tezin asıl amacı MgB_2 süperiletken külçe örneği içerisinde Fe difüzyonunun araştırılmasıdır. Demir difüzyonu farklı tavlama sıcaklıklarında farklı ısıl işlem süreleri için gerçekleştirildi. Fe difüzyonu için 50 μm kalınlığında Fe tabakası vakum altında metal buharlaştırmayla MgB_2 üzerine kaplandı. Bu tezin kapsadığı deneysel çalışmalar iki kısma ayrılır. İlk bölümde, süperiletken MgB_2 örneklerde Fe difüzyon $650-900^{\circ}C$ sıcaklığı aralığında 1 saat ısıl işlem uygulanarak çalışılmıştır. Prenslenmiş ama hiçbir ısıl işlem yapılmamış (Set 1N) örnekler ile preslenmiş ve $800^{\circ}C$'de 1 saat ısıl işlem yapılmış (Set 1S) olmak üzere iki set külçe MgB_2 tabletler üzerine Fe kaplaması yapıldı. Fe difüzyonunun MgB_2 kristal yapısı ve süperiletken özellikleri üzerine etkileri X-ışını difraksiyonu (XRD), taramalı elektron mikroskobu (SEM), kızılötesi spektroskopi (IR) ve özdirenç ölçümleri ile incelenmiştir. Her iki set malzemeler için demir difüzyon katsayısı c örgü parametresi ve oda sıcaklığı özdirenç değerleriyle hesaplandı. Bu sıcaklık aralığında demir difüzyonu katsayısının sıcaklığa bağlılığı Arrhenius denklemiyle tanımlandı. Beklendiği gibi tavlama sıcaklığının artmasıyla Fe difüzyon katsayısının arttığı bulunmuştur. Malzemeye demir difüzyonu sayesinde süperiletkenlik özellikler ve micro yapısında gözlenen iyileşmeler tartışılmıştır. İkinci kısımda, kaplama işlemi $800^{\circ}C$'de 1 saatlık ilk sinterlemeli (Set 2S) ve ilk sinterlemesiz (Set 2N) örneklere yapıldı. MgB_2 süperiletken malzemeye demir difüzyonu $900^{\circ}C$ sıcaklıkta 15 dakika,

30 dakika, 1 saat, 2 saat, 4 saat ve 8 zaman aralıklarında çalışıldı. Birinci kısıma benzer olarak, MgB_2'nin kristal yapısı ve süperiletkenlik özelliklerine demir difüzyonu etkisi XRD, SEM ve özdirenç ölçümleriyle araştırılmıştır. Tavlama işlemi için Fe difüzyon katsayısı *c* örgü parametresi ve oda sıcaklığı özdirenç değerleriyle hesaplandı. Beklendiği gibi tavlama zamanının artmasıyla Fe difüzyon katsayısının azaldığı bulunmuştur. Sonuç olarak difüzyon katsayısının artan sıcaklıkla artması ve artan ısıl işlem süresi ile azalması süperiletken MgB_2 malzemelerin ısıl işlem uygulamalarında dikkate alınmalıdır. Yüksek kaliteli süperiletken külçe, tel/şerit üretiminde düşük sıcaklık ve geniş zaman aralığında ısıl işlem yapılmalıdır.

ANAHTAR KELİMELER: MgB_2 Süperiletken Külçe Malzeme, Demir Difüzyonu, Difüzyonun Sıcaklığa Bağlılığı, Difüzyonun Zamana Bağlılığı ve Aktivasyon Enerjisi.

TABLE OF CONTENTS

Page

ABSTRACT . . . . . **v**

ÖZET . . . . . **vii**

TABLE OF CONTENTS . . . . . **ix**

LIST OF FIGURES . . . . . **xii**

LIST OF TABLES . . . . . **xvii**

LIST OF ABBREVIATIONS AND SYMBOLS . . . . . **xix**

1. INTRODUCTION **1**

1.1 Superconductivity 2

1.2 Fundamentals of Superconductivity 4

1.3 Applications of Superconductors 7

1.4 MgB_2 Superconductor 8

1.4.1 Crystal Structure of MgB_2 9

1.4.2 Physical and Superconducting Properties of MgB_2 10

1.5 The Phase Diagram of MgB_2 Superconductors 15

1.6 Fabrication of MgB_2 Superconductors 17

2. DIFFUSION **20**

2.1 A Historical Background 20

2.2 Theory of Diffusion 21

2.2.1 Solution of Diffusion Equation 22

2.2.1.1 Thin Film Solution 22

2.2.1.2 Error Function Solution 23

2.3 Mechanisms for Diffusion 25

2.3.1 Vacancy Mechanism 26

2.3.2 Interstitial Mechanism 26
2.3.3 Interstitialcy Mechanism 27
2.3.4 Divacancy Mechanisms 27
2.4 The Various Diffusivity 28
2.5 Temperature Dependence of Diffusion 29
2.6 Pressure Dependence of Diffusion 30
2.7 Time Dependence of Diffusion 30
2.8 Diffusion of MgB_2 Material 33
3. AIM AND SCOPE OF THE STUDY 35
4. MATERIALS AND METHODS 38
4.1 Fabrication Process of MgB_2 Bulk Samples 38
4.1.1 Heat Treatment Process 39
4.1.2 Fe Coating Process of MgB_2 40
4.2 Experimental Set-up 42
4.2.1 Sample Codes for Diffusion at Different Temperatures for 1 hour 43
4.2.2 Sample Codes for Diffusion for Different Sintering Times at 900°C 44
4.3 Removal Process 47
4.4 Sample Characterization 48
4.4.1 XRD Analysis 48
4.4.2 Scanning Electron Microscopy (SEM) and Energy Dispersive Spectrum (EDS) Analysis 50
4.4.3 Current-Voltage (I-V curve) Measurements at Room Temperature 50
4.4.4 Critical Transition Temperature (T_c) 51
4.4.5 Infrared spectroscopy (IR) 54
5. RESULTS AND DISCUSSIONS 56
5.1 Introduction 56

5.1.1 Structural Analysis of MgB_2 Superconductor Pellets Before and After Fe Coating 57
5.2 Effect of Sintering Temperature on Diffusion - Sintering at Different Temperatures 60
5.2.1 Phase Analysis 60
5.2.2 Microstructural and Chemical Analysis 66
5.2.3 Electrical Resistivity Measurements 72
5.3 Effect of Sintering Time on Fe Diffusion - Sintering for Different Times 78
5.3.1 Phase Analysis 79
5.3.2 Microstructural and Chemical Analysis 84
5.3.3 Electrical Resistivity Measurements 88
5.4 Calculations of Diffusion Coefficient and Activation Energy 94
5.4.1 Temperature Dependence of Fe Diffusion into MgB_2 95
5.4.2 Time Dependence of Fe Diffusion into MgB_2 102
5.4.3 Activation Energy of Fe Diffusion into MgB_2 108
6. CONCLUSION 110
7. REFERENCES 112
8. CURRICULUM VITAE 123

LIST OF FIGURES

Page

Figure 1.1 Three dimensional periodic table for known superconducting elements. 3

Figure 1.2 History of superconductors at critical temperature increasing over years. 4

Figure 1.3 J_c, T_c and B_c phase diagram showing the relationship between the three critical parameters of a superconductor (Buckel and Kleiner, 2014). 5

Figure 1.4 a) The crystal structure of MgB_2 (Larbalestier et al., 2001), b) MgB_2 grains observed in MgB_2 powder (scale bar 30 μm) and c) MgB_2 single crystal showing hexagonal shape (Nagamatsu et al., 2001). 9

Figure 1.5 The critical surface of MgB_2 superconductor as compared with conventional low temperature superconductor (LTS). 12

Figure 1.6 The temperature-composition phase diagrams of the Mg-B system under the pressures of a) 1 atmosphere, b) 1 Torr, c) 1 mTorr and d) The pressure versus temperature phase diagram. 16

Figure 2.1 Thin-layer solution of the diffusion equation for various diffusion times (value of $0.1, 0.3$ and 1.0 s). 24

Figure 2.2 a) erf function; Gaussian error function, based on integration of the "bell shaped" curve and b) Diffusion profiles of Au in solid. 25

Figure 2.3 Vacancy mechanism of diffusion. 26

Figure 2.4 Interstitial mechanism of diffusion. 26

Figure 2.5 Interstitialcy mechanism of diffusion. 27

Figure 2.6 Divacancy mechanism of diffusion. 27

Figure 2.7 a) Schematic representation of the Arrhenius relationship between diffusivity and temperature and b) Comparison of the Au diffusivity in solid lead as reported by Roberts-Austen (1896). 30
Figure 2.8 Pressure dependence of ^{198}Au diffusion in Au single crystals at constant temperature. 31
Figure 2.9 a) Distribution for different times including, initial time t_0 and b) Time dependency of instantaneous diffusion coefficients (Luguang et al., 2013). 32

Figure 3.1 XRD patterns for a) Fe sheath and b) MgB_2 core sample. 36

Figure 4.1 Schematic illustration of fabrication process for the ex-situ MgB_2 bulk samples. 39
Figure 4.2 Temperature-Time profile for sintering of MgB_2 bulk samples. . 40
Figure 4.3 a) Schematic diagram of the deposition region and b) Photograph of the evaporation chamber. 41
Figure 4.4 MgB_2 pellets before and after Fe coating. 41
Figure 4.5 Schematic diagram showing the sample codes for annealing at different temperatures for 1 hour. 45
Figure 4.6 Schematic diagram of different sintering times at 900°C. 46
Figure 4.7 Work flow chart for each step. 47
Figure 4.8 X-ray diffraction from lattice planes (Cullity and Stock, 2001). . 49
Figure 4.9 Schematic diagram of the current-voltage measurements system at room temperature. 51
Figure 4.10 a) The closed cycle He cryostat (CRY Industries) and b) The sample holder for transport resistance measurement. 52
Figure 4.11 Illustration of different critical temperatures on resistivity vs. temperature curve T_c from a) The temperature dependence of resistivity and b) First derivative of resistivity. 53

Figure 4.12 Infrared spectroscopy (Perkin Elmer Spectrum Two). 55

Figure 4.13 Infrared spectra of Fe_2B and MgB_2 powder samples. 55

Figure 5.1 XRD patterns of MgB_2 samples before and after Fe coating. From bottom to top; as received ex-situ MgB_2 powder, sintered MgB_2 pellet, coated MgB_2 pellet and MgB_2 pellet sintered after Fe coating. . . 57

Figure 5.2 Infrared spectra of after and before Fe coated MgB_2 samples. . . 58

Figure 5.3 SEM images of a) MgB_2 powder, b) MgB_2 pellet, c) Fe coated MgB_2 (non-sintered) and d) Fe coated MgB_2 (sintered). 59

Figure 5.4 XRD patterns of bare and Fe coated MgB_2 samples for different sintering temperatures. 62

Figure 5.5 a) Lattice parameter *a*, b) Lattice parameter *c*, c) Grain size and d) FWHM value behaviours for Fe coated and bare MgB_2 samples sintered for different temperatures. 63

Figure 5.6 SEM images of Fe/Fe_2B/MgB_2 cross sectional area for SF180 sample. 67

Figure 5.7 SEM images taken from upper surface for a) SB165, b) SF165, c) SB170, d) SF170, e) SB175 and f) SF175 sample. 68

Figure 5.8 SEM images taken from upper surface for a) SB180, b) SF180, c) SB185, d) SF185, e) SB190 and f) SF190 sample. 69

Figure 5.9 Energy Dispersive X-ray Spectroscopy analysis of bare and Fe coated MgB_2 bulk samples; a) SB180, b) SF180, c) NB180 and d) NF180. 71

Figure 5.10 Resistance versus temperature curves for a) initial sintering set of bare sample (SB), b) initial sintering set of Fe coated sample (SF), c) not initial sintering set of bare sample (NB) and d) not initial sintering set of Fe coated (NF) at different annealing temperature. 72

Figure 5.11 Resistance versus temperature curves for different sintering temperatures. 74

Figure 5.12 a) T_c^{offset}, b) T_c and c) ρ_{300K} behaviours for Fe coated and bare MgB_2 samples sintered for different temperatures. 75

Figure 5.13 a) Active area fraction and b) Residual resistivity ratio value behaviours for Fe coated and bare MgB_2 samples sintered for different temperatures. 78

Figure 5.14 XRD patterns of bare and Fe coated MgB_2 samples for different sintering times. 80

Figure 5.15 a) Lattice parameter *a*, b) Lattice parameter *c*, c) Grain size and d) FWHM behaviours for Fe coated and bare MgB_2 samples sintered for different times. 82

Figure 5.16 SEM images for a) SB1590, b) SF1590, c) SB3090, d) SF3090, e)SB190 and f) SF190 sample. 85

Figure 5.17 SEM images for a) SB290, b) SF290, c) SB490, d) SF490, e) SB890 and f) SF890 sample. 86

Figure 5.18 EDS analysis for a) SB1590, b) SF1590 (Fe-diffused side), c) NB1590 and d) NF1590 (Fe-diffused side) sample. 87

Figure 5.19 Resistance versus temperature curves for a) initially sintered bare samples (SB), b) initially sintered Fe coated samples (SF), c) not initially sintered bare samples (NB) and d) not initially sintered Fe coated samples (NF) for different sintered time durations. 88

Figure 5.20 Resistance versus temperature curves for different sintering times. 89

Figure 5.21 a) T_c^{offset}, b) T_c and c) ρ_{300K} behaviours for Fe coated and bare MgB_2 samples sintered for different times. 91

Figure 5.22 a) Active area fraction and b) Residual resistivity ratio value behaviours for Fe coated and bare MgB_2 samples sintered for different times. 93

Figure 5.23 XRD patterns of Fe diffused samples of sintered between 650 and 750°C for 1 hour. 96

Figure 5.24 XRD patterns of Fe diffused samples of sintered between 800 and 900°C for 1 hour. 97

Figure 5.25 Concentration profile of Fe versus the thickness for a) SF165-NF165, b)SF170-NF170, c) SF175-NF175, d) SF180-NF180, e) SF185-NF185 and f) SF190-NF190 samples calculated by changes in lattice parameter c. 100

Figure 5.26 Concentration profile of Fe versus the thickness for a) SF165-NF165, b)SF170-NF170, c) SF175-NF175, d) SF180-NF180, e) SF185-NF185 and f) SF190-NF190 samples calculated by changes in ρ_{300K}. . . 101

Figure 5.27 XRD patterns for all steps belonging to the samples a) SF1590, b) NF1590, c) SF3090 and d) NF3090. 102

Figure 5.28 XRD patterns for all steps belonging to the samples a) SF290, b) NF290, c) SF490 and d) NF490. 103

Figure 5.29 Concentration profiles of Fe versus the thickness for a) SF1590-NF1590, b)SF3090-NF3090, c) SF290-NF290 and d) SF490-NF490 samples calculated by changes in lattice parameter c. 105

Figure 5.30 Concentration profiles of Fe versus the thickness for a) SF1590-NF1590, b)SF3090-NF3090, c) SF290-NF290 and d) SF490-NF490 samples calculated by changes in ρ_{300K}. 106

Figure 5.31 The dependence of Fe diffusion coefficient on sintering time duration; a) $D^{(1)}$ SF/Latt. prm. c, b) $D^{(2)}$ SF/ρ_{300K}, c) $D^{(3)}$ NF/Latt. prm. c and d) $D^{(4)}$ NF/ρ_{300K}. 107

Figure 5.32 Dependence of diffusion coefficient on sintering temperature. . . 108

LIST OF TABLES

Page

Table 1.1 A comparison between different kinds of superconductor materials. 7

Table 1.2 General applications of superconducting materials. 8

Table 1.3 Superconducting parameters of MgB_2 sample. 11

Table 1.4 List of added into MgB_2 superconductor compound in the literature. 14

Table 1.5 Basic properties value of Mg, B and MgB_2. 15

Table 4.1 Samples annealed at different temperatures for fixed time (1 hour). 43

Table 4.2 The coding system in different times at fixed temperature (900°C). 44

Table 5.1 Energy Dispersive X-ray Spectroscopy elemental analysis results. 60

Table 5.2 Lattice parameter a and c, grain size, FWHM, and Fe_2B peak intensity values of Set 1S and Set 1N MgB_2 samples for different sintering temperatures. 64

Table 5.3 Basic properties value of Fe element. 66

Table 5.4 Results of transport measurements of T_c^{offset}, T_c and ρ_{300K} for different sintering temperatures 73

Table 5.5 Residual resistivity ratio, difference between resistivity at 300 K and 40 K, and active area fraction of the Fe coated and bare MgB_2 samples. 77

Table 5.6 Lattice parameter a-c, grain size, FWHM, and Fe_2B peak intensity values of Set 2S and Set 2N MgB_2 samples for different sintering times. 81

Table 5.7 Transport measurement results for different sintering times showing the values for T_c^{offset}, T_c and room temperature resistivity. 90

Table 5.8 Residual resistivity ratio, resistivity difference between 300 K and 40 K, and active area fraction of Set 2S and Set 2N samples. 93

Table 5.9 Lattice parameter c (Å) and room temperature resistivity ($\mu\Omega$cm) values at successive steps. 98

Table 5.10 Fe diffusion coefficients (D) for different sintering temperatures for 1 hour. 99

Table 5.11 Lattice parameter c (Å) and room temperature resistivity ($\mu\Omega$cm) values obtained in eight steps by successive removal of thin layers. . . . 104

Table 5.12 Fe diffusion coefficients for different sintering times at 900°C. . . 107

LIST OF ABBREVIATIONS AND SYMBOLS

K	Kelvin
T_c	Critical temperature
H_c	Critical field
J_c	Critical current density
J_c(B)	In-field critical current density
λ	London penetration depth
ξ	Coherence length
B	Magnetic field
B_{c1}	Lower critical field
B_{c2}	Upper critical field
B_{irr}	Irreversibility field
ρ	Resistivity
ρ_{300K}	Room temperature resistivity
T	Temperature
I	Current
V	Voltage
R	Resistance
I_c	Transport current
Ω	Unit of resistance
a, c	Lattice parameters
cm	Centimeter
μ**m**	Micrometer
h	Hours
s	Second
min	Minute
$^{\circ}$**C**	Celsius Degree

T_c^{offset}	Temperature corresponding to offset of transition
T_c^{onset}	Temperature corresponding to onset of transition
ΔT_c	Width of transition
$\mathring{A}$	Angstrom unit
θ	Angle of diffraction
d	Inter atomic spacing
D	Diffusion coefficient
M	Magnetization
DC, dc	Direct Current
Mg	Magnesium
B	Boride
MgB_2	Magnesium Diboride
XRD	X-ray Diffraction
SEM	Scanning Electron Microscope
EDS/EDX	Energy Dispersive X-ray Spectroscopy
FWHM	Full Width at Half Maximum
LTS	Low Temperature Superconductors
HTS	High Temperature Superconductors
MRI	Magnetic Resonance Imaging
PIT	Powder In Tube
SQUID	Superconducting Quantum Interference Device
SS	Stainless Steel
YBCO	Yttrium Barium Copper Oxide
BSCCO	Bismuth Strontium Calcium Copper Oxide
SMES	Superconducting Magnetic Energy Storage
R&D	Research and Development
MAGLEV	Magnetic levitation

ACKNOWLEDGEMENTS

Many people have provided assistance and guidance throughout my PhD. At the very beginning, I must express that I owe a great deal to my advisor Prof. Dr. İbrahim Belenli for his patience, support, guidance, tolerance and supervision throughout this study.

I would express my gratitude to my Co-advisor Prof. Dr. Cabir Terzioğlu and Prof. Dr. Ali Gencer for their valuable contribution during the discussions and their support.

I would like to thank Assoc. Prof. Dr. Mustafa Akdoğan and Assoc. Prof. Dr. Hakan Yetiş for their valuable contributions at all stages of my studies. I also, thank Assist. Prof. Dr. Erhan Budak for infrared spectroscopy measurements at chemistry department.

I owe a great deal to laboratory colleague for her/his intensive help in my experimental work for XRD, SEM, EDS, resistivity measurements. I am also thankful to research assistants Arzu Kurt and Fırat Karaboğa for their friendship and invaluable support.

Special thanks to my wife Canan Ülgen for waiting with me until midnights, sharing good and bad times and drinking coffee every morning.

I am very grateful to my amazing parents: Dad (Ramazan Ülgen), Mom (Rabia Ülgen) and Brother (Kerim Ufuk Ülgen) for their love, motivating support and constant encouragement throughout my doctorate studies.

This study was financially supported by the TUBİTAK, Grant No: 113F080. Also, AIBU Research Fund Grant No: 2016.03.02.1067.

1. INTRODUCTION

The phenomenon of superconductivity is zero electrical resistance and exclusion of the interior magnetic flux happening in certain materials when cooled below a characteristic critical temperature (T_c). So these materials have exactly zero direct current electrical resistance and the Meisner effect which is associated with nearly perfect diamagnetism.

Specially, many researchers have shown that most of the elements including metals, and many metallic alloys have these properties exhibiting transition from normal state to superconducting state.

Discovery of superconductivity raised hopes for applications in magnet and energy technology and triggered plenty of interest in application areas. With these characteristics, superconductivity may have applicability in high-speed, high-sensitivity, low-voltage sensors and switches.

The industrial applications of these low critical temperature superconductors were restricted by the high cost of the liquid helium and the complicated operation of the cooling system.

In today, superconducting materials are having a considerable influence on the development of the next generation of medical services, transportation, electrical power systems, electricity distribution, communication technology and integrated circuits.

Our energy-hungry world increasingly requires new technologies with higher efficiency, in this way, superconductors are becoming indispensable materials.

1.1 Superconductivity

The effect of superconductivity was discovered over a century ago by a brilliant Dutch physicist H. Kamerlingh Onnes (1911). Onnes, a professor of physics at the University of Leiden, successfully liquefied Helium in 1908. He made experiments on the physical properties of mercury at 4.22 K temperatures an unexpected decrease in resistivity. He used liquid helium to cool down various metals and tried to find out the relation between electric resistance and temperature, found surprisingly that the resistance of mercury steeply dropped to zero at about 4.2 K. Onnes (1913) won Nobel Prize in Physics for his superconductivity research.

Thus the phenomenon of vanishing of electrical resistivity of materials below a particular low temperature has been called superconductivity and materials which exhibit this property are called superconductors. Superconductors differ from normal conductors as their electrical resistivity plunge from a finite value to zero at a specific temperature which is called superconducting transition temperature (T_c). The superconducting elements are presented in a 3D periodic table in Figure 1.1 (Rogalla and Kes, 2011). This figure shows the relative T_c of elements on the periodic table, and that high T_c elements are located at the horizontal edge of the periodic table.

In the late 1950s, two compounds were discovered to be superconductors; NbTi and Nb_3Sn (Matthias et al., 1954). These two compounds have suitable properties for applications of superconductivity, as they can carry high current densities in high magnetic fields. NbTi and Nb_3Sn superconductors have critical current densities higher than $2x10^5$ A/cm^2 in 5 T magnetic field (Barth, 2013). Superconducting technologies associated with Nb-based superconductors were soon developed.

In later years, many other superconductors have been discovered such as lead, niobium and vanadium (Stromberg and Swenson, 1962; Radebaugh and Keesom, 1965). There are many superconducting elements and a lot of superconducting compounds, while some elements only become superconducting under high pressure.

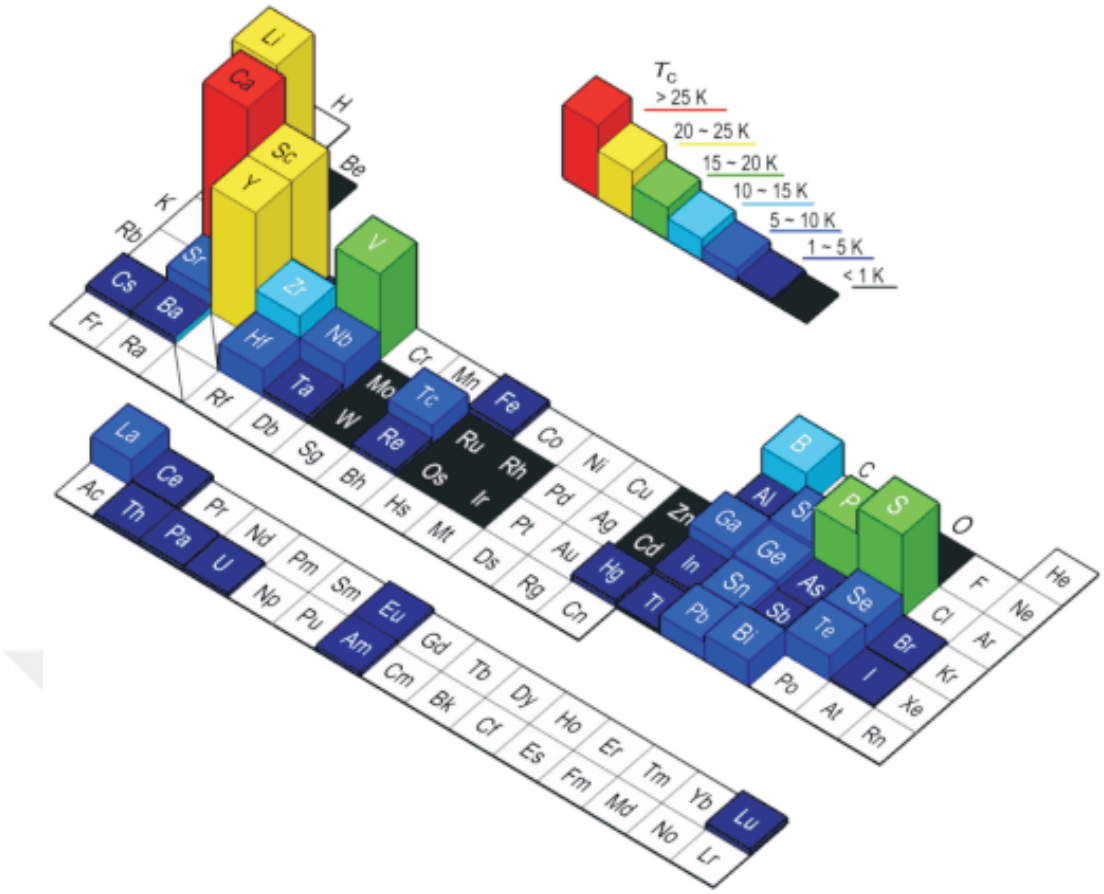

Figure 1.1. Three dimensional periodic table for known superconducting elements.

The search for new superconducting materials continued for decades and has led to discovery of the intermetallic compound lanthanum barium copper oxide (LaBaCuO) exhibiting a T_c of about 30 K by Karl Alex Muller and Johannes Georg Bednorz (1986). After a few years, bismuth and yttrium based superconductors are synthesized, and which these materials are generally known as BSCCO and YBCO respectively. Professor Jun Akimitsu (2001) discovered superconductivity at 39 K in MgB_2 and announced at the Symposium on Transition Metal Oxides in Sendai, Japan.

Figure 1.2 summarizes the discoveries of various superconductors in years versus critical temperature graph, which shows a clear trend of discovering higher temperature superconductors. After one century of this phenomena, thousands of materials including metals, alloys, binary and multi-component compounds of metals, ceramics, doped fullerenes and organic molecules are found to be superconducting with transition temperatures ranging from 4 K to 150 K (Hott et al., 2005).

Recently the new types of superconducting materials, $LaO_{1-x}F_xFeAs$ with T_c at 43K (Zhi-An et al., 2008) and SmFeAsOF with T_c greater than 50 K (Chen et al., 2008) have been discovered.

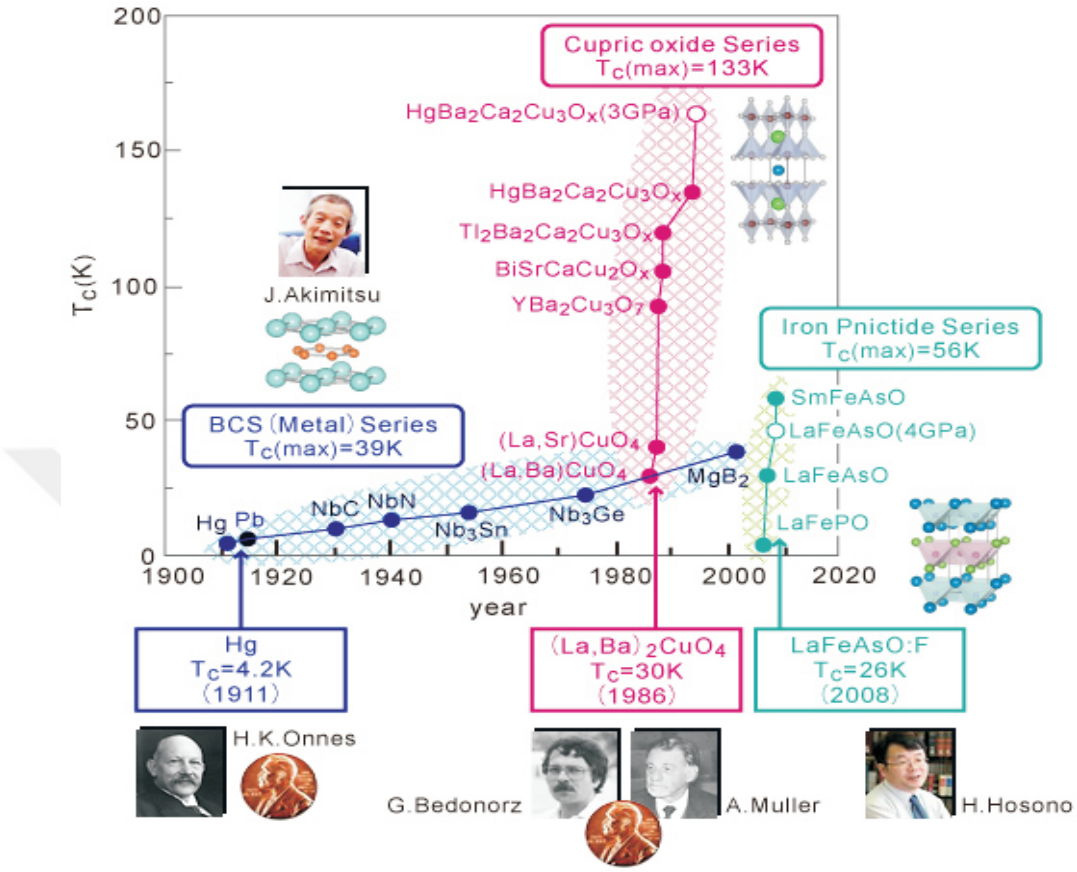

Figure 1.2. History of superconductors at critical temperature increasing over years.

1.2 Fundamentals of Superconductivity

The critical temperature, the critical current density and the critical field values of a superconductor define the boundaries of the superconducting state depicted with Figure 1.3. The superconducting materials become normal outside of this region. The boundary surface between superconducting and normal regions is called the critical surface.

In 1933, Walter Meissner and his student Robert Ochsenfeld made an important discovery which is the second fundamental property of superconductivity (Meissner and Ochsenfeld, 1933). They found that the material in superconducting state exhibits spontaneous, and complete expulsion of magnetic flux from its interior.

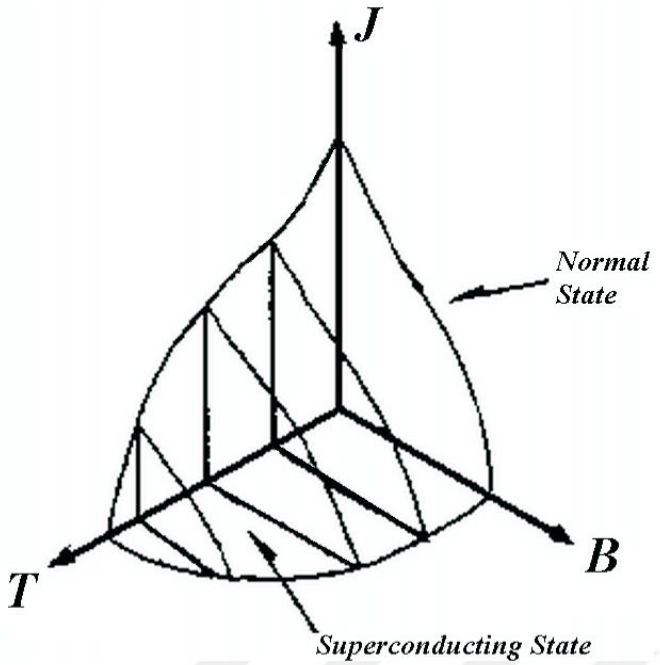

Figure 1.3. J_c, T_c and B_c phase diagram showing the relationship between the three critical parameters of a superconductor (Buckel and Kleiner, 2014).

The flux lines are expelled from the interior of the superconductor while this superconducting material makes transition from normal state to superconducting state upon cooling under a certain external magnetic field, in such a way that the magnetic field inside the superconductor is zero. This characteristic property of a superconductor is called Meissner effect.

Firtz and Heinz London have developed a set of electrodynamic equations from Maxwell's equations, so that called the London equations for Meissner effect (London, 1935). Total magnetic field exponentially decays at the surface of the superconductor within a characteristic length λ, also known as the London penetration depth.

V.L.Ginzburg and L.Landau (1950) extended the London theory by introducing the order parameter ψ, which defines the local density of super electrons $n_s = |\psi(x)|^2$. The external magnetic field does not fall to zero at the surface but decays exponentially inside the superconductor, as know this distance called penetration depth (λ). The parameter κ parameter is given by the relation $\kappa = \lambda/\xi$, where ξ is the Ginzburg-Landau coherence length.

In 1957, the first microscopic theory of the superconducting properties was proposed by three physicists J. Bardeen, L. Cooper and J.R. Schrieffer. This theory is known as the BCS Theory (Bardeen et al., 1957), which shows that superconductivity results from the interaction between electrons and surrounding ions in crystal.

In the same years, theoretical analysis of superconducting properties under magnetic field was improved by Alexei Alexeyevich Abrikosov. His results indicated that superconductors can be categorized into two types (Abrikosov, 1957). In the case of type-I superconductors, an external magnetic field higher than a B_c destroys the superconducting state and type-II superconductors have two critical fields, namely, the lower critical field (B_{c1}) and the upper critical field (B_{c2}).

Since the discovery of superconductivity, many scientists have been working to find new superconducting materials with high critical temperatures. In 1986, Johannes Georg Bednorz and Karl Alexander Müller were discovered a complex compound consisting of copper, oxygen and rare earth element (Bednorz and Müller, 1986). This invention opened the gate to discover high temperature superconductor (HTS). Two compounds of this same family, yttrium-based and bismuth-based superconductors are synthesized by Wu et al. (1987) and Maeda et al. (1988), respectively. These materials are generally known as BSCCO ceramic superconductor which includes bismuth, strontium, calcium, copper and oxygen. Both BSCCO and YBCO ceramic superconductors demonstrated high performance in magnetic field. Mercury based superconductor, HgBaCaCuO, with highest a critical temperature of 130 K has been discovered by Schilling et al (1993).

In 2001, the group of Akimitsu discovered superconductivity at 39 K in magnesium diboride (MgB_2), which is a simple metallic binary compound. MgB_2 superconductors have high T_c, I_c and B_{c2} values, as well as the large coherence length, lower anisotropy and low cost raw material for practical applications. Due to these advantages, MgB_2 superconducting materials have been a strong competitor for electric power and magnet applications at $\sim$20 K, especially for magnetic resonance imaging (MRI) magnets

which can work without liquid cryogen. A comparison of typical applied superconducting materials are listed in Table 1.1 (Tobin, 2008).

Table 1.1. A comparison between different kinds of superconductor materials.

Material	Crystal Structure	Anisotropy	T_c Kelvin	B_{c2} Tesla	B_{irr} Tesla	J_c 4.2 K A/cm^2	n-value
NbTi	BCC	Negligible	9	15	11 (at 4K)	3x10^5	80
Nb$_3$Sn	A15	Negligible	18	30	24 (at 4K)	8x10^5	30
YBCO	Layered perovskite	7	92	>100	5 – 7 (at 77K)	4x10^6	20 – 30
Bi2223	Layered perovskite	$\sim$ 50 – 100	108	>100	0.2 (at 77K)	2x10^5	20 – 30
Fe122	Layered perovskite	Negligible	35	>100	90 (at 4K)	1x10^5	20 – 30
MgB$_2$	Hexagonal	1.5 – 5	39	35	25 (at 4K)	2x10^5	30 – 50

1.3 Applications of Superconductors

Superconducting materials have a wide range of commercial, industrial and technological applications in sensor materials and in high field magnets. It is finding their applications in diverse fields, including motors and generators (Bretz, 2004), for use in a power transmission networks (Lubkin, 1996), in medicine (MRI systems), in daily scientific research (MPMS: Magnetic Properties Measurement System and PPMS: Physical Properties Measurement System), in sensitive magnetometers based on the Josephson effect and SQUIDs (Superconducting Quantum Interference Devices) (Jaklevic et al., 1964) and nuclear fusion reactors. The special application sectors of superconducting materials are tabulated in Table 1.2 (Devadas, 2015). New resource and development of superconductors will increase with critical temperature. Superconductors based of liquid nitrogen has provided industry more flexibility to utilize superconductivity as compared to liquid helium superconductors.

Table 1.2. General applications of superconducting materials.

AREA/FIELD	APPLICATIONS
Energy/Power: Generation & Storage	Generators, SMES, Superconducting bearings for flywheel storage.
Energy/Power: Distribution Magnets	Cables, Transformers, Current leads, FCLs, Motors. NMR, MRI instruments, Magnetic confinement of plasma in Fusion reactors, Particle accelerators, High field magnets.
Electronics	In microwave filters, Digital logic circuits as RSFQ, Sensor applications.
Biomedical	Detection of extremely small neuromagnetic fields, Magnetoencephalanography (MEG), Magnetocardiography (MCG).
Industrial	Magnets for shielding and separation, sensors.
R & D	Superconducting RF cavities in particle accelerators Synchrotrons and High field magnets.
Other applications	Magnetic levitation, Magnetohydrodynamics, Space applications.

1.4 MgB_2 Superconductor

The superconductivity in MgB_2 was discovered by Prof. Jun Akimitsu in 2001, although MgB_2 material was first synthesized and its structure confirmed in 1954 (Jones and Marsh, 1954). Following the announcement of superconductivity in MgB_2, many research groups all over the world started to work on this intermetallic superconductor theoretically and experimentally. High critical temperature, high critical current density, and lower costs provide advantages to these materials in terms of applicability. MgB_2 has been fabricated in various forms, such as bulks (Takano et al., 2001), single crystals (Chen et al., 2011), thin films (Petaccia et al., 2006), wires (Akdogan et al., 2015) and tapes etc.

1.4.1 Crystal Structure of MgB_2

MgB_2 has a layered and simple hexagonal AlB_2 type structure, and also it has graphite like (honeycomb) boron (B) layers that are separated by hexagonal close packed (hcp) magnesium (Mg) layers. Each Mg atom is positioned at the center of hexagons of B atoms as shown in the schematic diagram of MgB_2 in Figure 1.4a (Larbalestier et al., 2001). The metallic B layers play an important role in the superconductivity of MgB_2 (Korkus et al., 2001).

MgB_2 indicates a strong anisotropy in the $B-B$ lengths (Nagamatsu et al., 2001), so that the distance between the boron planes (c-axis) is significantly longer than the in plane $B-B$ distance (a-axis). The anisotropy which extensively affect the superconducting properties in crystal structure of MgB_2 grains (Figure 1.4b) and single crystal (Figure 1.4c) is exhibited by Kim et al (2002).

The intra-layer interatomic distances of $B-B$ and $Mg-Mg$ are 0.1780 nm and 0.3084 nm, respectively, the inter-layer interatomic distances are $B-B$ 0.17 nm $Mg-B$ 0.25 nm and $Mg-Mg$ 0.3524 nm (Jones and Marsh 1954, 1953; Vinod et al., 2007).

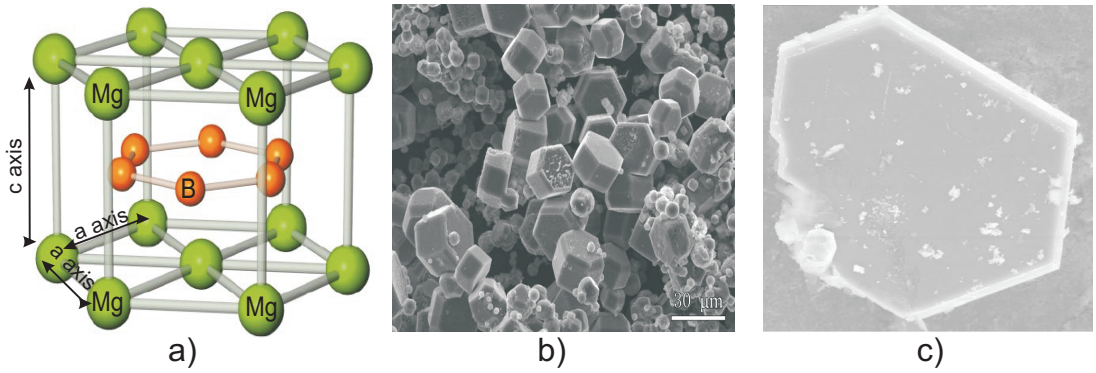

Figure 1.4. a) The crystal structure of MgB_2 (Larbalestier et al., 2001), b) MgB_2 grains observed in MgB_2 powder (scale bar 30 μm) and c) MgB_2 single crystal showing hexagonal shape (Nagamatsu et al., 2001).

Lattice parameters of hexagonal MgB_2 are $a = b = 0.3088$ nm and $c = 0.3522$ nm (Buzea and Yamashita, 2001). Laughlin and Hono (2014) have verified their results categorizing MgB_2 into a P6/mmm space group, with Mg atoms occupying (0,0,0) sites and B taking $(\frac{1}{3}, \frac{2}{3}, \frac{1}{2})$ and $(\frac{2}{3}, \frac{1}{3}, \frac{1}{2})$ sites. In crystalline forms, each Mg atom donates its electron to the boron planes.

1.4.2 Physical and Superconducting Properties of MgB_2

MgB_2 is a frangible material like the HTS materials and typical polycrystalline MgB_2 has a grain size from 10 nm to 10 μm (Rowell, 2003). Fully dense MgB_2 is rather difficult to achieve despite great efforts using different techniques, but MgB_2 wires with a density of 2.4 g/cm^3 were produced by diffusion of Mg into B fibres which compares with a theoretical density of about 2.6 g/cm^3. The MgB_2 powder at 1250°C sintering temperature and under a high pressure of 3.5 GPa led to material reaching the theoretical density (Takano et al., 2001). The anisotropy value of MgB_2 is between 1.5 and 5, but it is lower compared to the highly anisotropic HTS (Eisterer et al., 2003). On the other hand, MgB_2 bulk samples and partially oriented crystallites, the anisotropy ratio is reported to be between 1.1 and 1.7 (De Lima et al., 2001). The coherence length of this material is $5 - 12$ nm and penetration depth is $100 - 140$ nm (Finnemore et al., 2001). MgB_2 is a type II superconductor and has two superconducting gaps in the superconducting state, $\Delta_1 = 5 - 7$ meV and $\Delta_2 = 1.5 - 2.0$ meV (Iavarone et al., 2004). Table 1.3 summarizes the most important properties of MgB_2 sample (Buzea and Yamashita, 2001).

Figure 1.5 shows the relationship among T_c, J_c and B_c for superconductors MgB_2, NbTi and Nb_3Sn (Holúbek, 2008). T_c of MgB_2 superconductor is the highest among the inter-metallic superconductors, being 39 K with a transition width of about 1 K. The value of T_c depends on the crystal structure, hence, variations in the lattice parameters (a and c) will affect T_c (Ansari et al., 2013).

Table 1.3. Superconducting parameters of MgB_2 sample.

Parameters	**Values**
Critical Temperature	$T_c = 39 - 40$ K
Hexagonal Lattice Parameters	$a = b = 3.086$ Å, $c = 3.524$ Å
Theoretical Density	$\rho = 2.57$ g/cm^3
Pressure Coefficient	dT_c/dP = -1.1 – 2 K (Gpa)$^{-1}$
Carrier Density	$n_s = 1.7 - 2.8 \times 10^{23}$ holes cm^{-3}
Isotope Effect	$\alpha_T = \alpha_B + \alpha_{Mg} = 0.30 + 0.02$
Resistivity Near T_c	$\rho(40\text{ K}) = 0.4 - 16\mu\Omega$cm
Resistivity Ratio	RR=$\rho(40\text{ K})/\rho(300\text{ K}) = 1 - 27$
Upper Critical Field	$H_{c2}\|\|$ab(0) = 14 – 39 T
	$H_{c2}\|\|$c(0) = 2 – 24 T
Lower Critical Field	$H_{c1}(0) = 27 - 48$ mT
Irreversible Field	$H_{irr}(0) = 6 - 35$ T
BCS Coherence Lengths	$\xi_{ab}(0) = 3.7 - 12$ nm
	$\xi_c(0) = 1.6 - 3.6$ nm
Penetration Depths	$\lambda(0) = 85 - 180$ nm
Energy Gap	$\Delta(0) = 1.8 - 7.5$ meV
Debye Temperature	$\Theta_D = 750 - 880$ K
Critical Current Densities	J_c(4.2 K, 0 T)>10^7Acm^{-2}
	J_c(4.2 K, 4 T)=10^6Acm^{-2}
	J_c(4.2 K, 10 T)>10^5Acm^{-2}
	J_c(25 K, 0 T)>10^6Acm^{-2}
	J_c(25 K, 2 T)>10^5Acm^{-2}

Experimental results on MgB_2 show that T_c is reduced as a result of isostatic pressure (Schneider and Castro, 2005), neutron irradiation (Tarantini et al., 2006), poor crystallinity (Kumakura, 2007), strain in the lattice (Kim, 2007), chemical doping, inhomogeneity, etc. After the discovery of superconductivity in MgB_2, improving the T_c by substitutions with different radii has not given any satisfactory results. The normal state of MgB_2 is metallic and the normal state resistivity is much lower than that of other superconductors. The MgB_2 wire samples have a very low normal state resistivity (ρ_{300K}) of $\sim$10 $\mu\Omega$cm, and high residual resistivity ratio (RRR) value of 25.3 are observed by Canfield (2001). In addition, the residual resistivity ratio defined by $\rho(300K)/\rho(40K)$ was also estimated by Xu (2009).

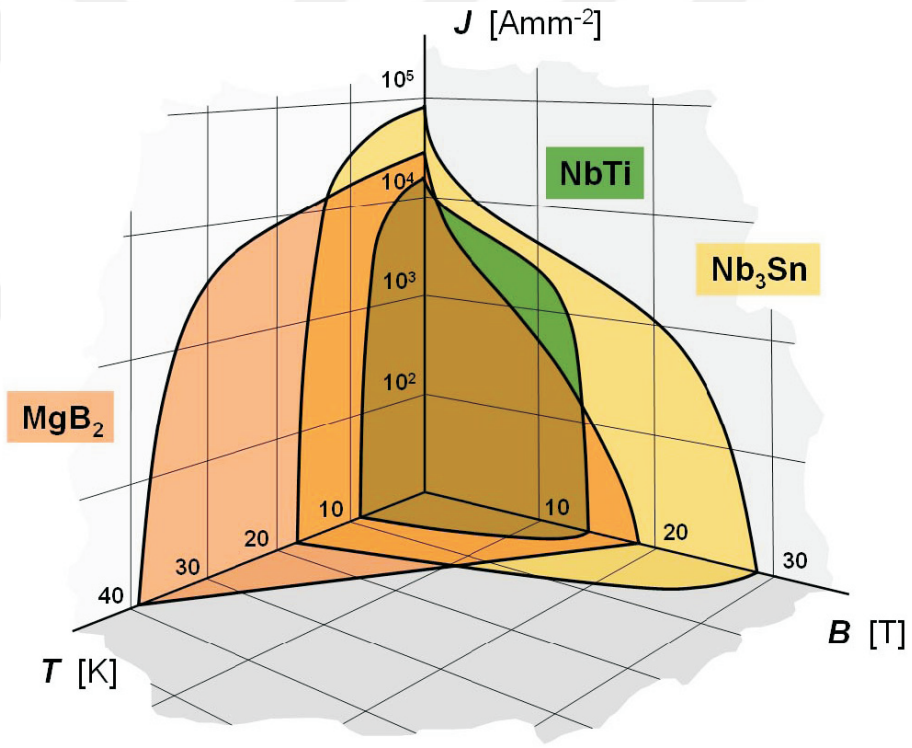

Figure 1.5. The critical surface of MgB_2 superconductor as compared with conventional low temperature superconductor (LTS).

According to the resistivity analysis by Rowell (2003), a wide range of resistivity values has been reported for MgB_2. The resistivity at room temperature varies between 20 and 100 $\mu\Omega$cm, covering all the samples types from bulk to thin films. Rowell offered a model that normal state resistivity (sensitive to inter and intergranular defects)

can be used as a measure of effective cross-sectional area for current transport in the normal and superconducting states. He proposed an equation for connectivity estimation as a practical quantity to evaluate the connectivity that is the active area fraction.

I_c or J_c is another important parameter in superconductors. I_c is a measure of the largest current which superconductor can carry without electrical resistivity. The critical current value depends on the size of the superconductors. But, J_c is widely used, which independent on the size of the superconductors, it is defined as the critical current per cross-sectional area of superconductor. For polycrystalline bulk MgB_2 samples the highest value J_c (0T, 4.2K) achieves 10^6 A/cm^2 (Vinod et al., 2006), and for MgB_2 tapes, J_c (0T, 20 K)=4.5×10^6 A/cm^2 is reported by Kumakura et al (2002).

Factors such as grain boundaries, porosity of the sample, presence of impurities, particle size distribution of precursor materials and sintering conditions have a strong effect on the critical currents in MgB_2. The grain boundaries in MgB_2 are not only transparent to current flow, but also help to improve the J_c by grain boundary pinning of magnetic flux. Porosity is one of the main factor in terms of the transport J_c in MgB_2 (Liu et al., 2003). Porosity effect is observed in the ex-situ powder process, the final high temperature heat treatment plays an important role in reducing the porosity (Shcherbakova, 2006).

MgB_2 bulk samples and partially oriented crystallites, the anisotropy ratio is reported to be between 1.1 and 1.7 (De Lima et al., 2001). Anisotropic behavior of MgB_2 superconductor material in variation of the critical field values can be observed from the planes parallel and perpendicular to the *ab*-plane. Anisotropy is very important property of superconductivity, both basic understanding of this material and practical applications. Studies on single crystals of MgB_2 have shown that the $H_{c1,c} = 27.2$ mT and $H_{c1,ab} = 38.4$ mT at zero temperature (Xu et al., 2001). MgB_2 polycrystalline superconductor shows rather low H_{c2} values, 16 T at 0 K (Habler et al., 2008). An explanation for H_{c2} performance was given by Gurevich (2007), weakly coupled, multi band BCS model and he took into account intra-band and inter-band scattering by nonmag-

netic impurities. He showed that H_{c2}(T) depends on σ and π band. When the π band is deformed, it will have higher H_{c2} at low temperatures, and total H_{c2} will show an upturn behaviour at low temperatures. The H_{c2} of a superconducting material is inversely proportional to its coherence length, ξ, so H_{c2} increases as ξ decreases (Yamamoto et al., 2005). Various kind of chemical species were added in MgB_2 superconductor materials, which include metals, borides, oxides, carbides and silicates. Table is 1.4 listed parts of the doping studies for MgB_2 superconductor material in the literature. It has been experimentally proven that C-based doping leads to significant enhancement in the superconducting properties of MgB_2 conductor. Carbon based doping results have shown that C atoms substitute for B atoms in the MgB_2 crystal structure (Yamada et al., 2006). In addition, carbon donates extra electrons and reduces the number of holes in this compound (Xi, 2008).

Table 1.4. List of added into MgB_2 superconductor compound in the literature.

Borides	**Compounds**	**Oxides**		**Metals**		**Carbon**
WB	MgH_4	Ag_2O	Ho_2O_3	Al	Pt	C and Nano-C
AlB_2	Fe_2B	ZnO	Nd_2O_3	Ag	Ru	CNT
TaB_2	$ZrSi_2$	CeO_2	Sb_2O_3	Fe	Sb	B_4C
TiB_2	$SiCl_4$	GeO_2	Co_3O_4	Ge	Sc	$C_{15}H_{12}O_2$
NiCoB	Si_3N_4	TiO_2	Fe_3O_4	Co	Te	$Li_3B_4C_2$
ZrB_2	AIN	TeO_2	Td_4O_7	Mo	Sn	$C_{16}H_2O_3N_2$
CeB_4	SiC	Bi_2O_3	Pr_6O_{11}	Mn	Ti	CaC_2
SmB_6	WSi_2	Y_2O_3	$CuFe_2O_4$	Ni	W	$C_4H_6O_4$
CaB_6N_4	FeTi	Al_2O_3	YBCO	La	Zn	$C_4H_6O_5$
VB_2	MgH_2	Eu_2O_3	Dy_2O_3	Hf	Se	BC_2
BN	CaH_2	(Bi,Pb)-2223	Bi-2212	Cr	Cu	Ti_3SiC_2
c-BN		CrO_2	—	Ba	Gd	$TiCl_3$
FeB				Pd	Re	CH_4N_2O
				Rh	Sn	
				Bi	Gr	

1.5 The Phase Diagram of MgB_2 Superconductors

As the molecular formula states, MgB_2's hcp structure is composed of a ratio of one magnesium atom to two boron atoms and the bonding between the atoms is a mix of ionic, covalent and metallic bonds (Leiro et al., 2004). The properties of the separate elements ($Mg - B$) and MgB_2 are given in Table 1.5. Phase diagram is very important

Table 1.5. Basic properties value of Mg, B and MgB_2.

Properties	**Magnesium**	**Boron**	**Magnesium diboride**
Atomic number	12	5	-
Valence	2+	3+	-
Atomic weight (amu)	24.31	10.81	-
Molecular weight (g/cm^3)	-	-	45.93
Theoretical Density(g/cm^3)	1.738	2.34	2.57
Crystal structure	bcc	Rhombohedral	hcp
Atomic Radius (nm)	0.160	0.085	-
Atomic Volume (cm^3/mol)	13.97	4.6	-
Melting Point (K)	923	2349	$\sim$2493 (at 3 Gpa)
Heat of Fusion (Kj/mol)	8.954	50.20	-
Heat of Vaporization (kJ/mol)	127.4	489.7	-
Mohs Hardness	2	9.5	-
Hardness(kg/cm^2)	-	-	1700-2800
Thermal Conductivity (J/m sec deg)	156	27.4	-
Electrical Resistivity at 20°C (Ωm)	43.9×10^{-9}	1.5×10^{4}	1.03×10^{-7}

issue for physical and chemical products. MgB_2 can be synthesized by a simple route from the reaction of B with Mg liquid, generally at a temperature above 650°C, which is the melting point of Mg. The binary phase diagram for Mg and B are shown in Figure 1.6a to Figure 1.6c (Liu et al., 2001). From the figure we can see that when the temperature is higher than 650°C and the atomic Mg and B ratio is greater than 1:2, Mg element is melt and coexists with MgB_2 solid.

If ratio $1:4 < \mathrm{Mg:B} < 1:2$ and the temperature is below 1090°C, MgB_2 coexists with MgB_4. The compound forms above 800°C from elemental powders. The phase diagram and the formation of the MgB_2 phase is effected by pressure (Figure 1.6). There are large composition windows in which Mg liquid and MgB_2 coexist. From the phase diagram, its evident that there is a big variation of processing temperature from around $650-1000$°C to from MgB_2 as the liquid phase of MgB_2 exists in 1 atm. The phase diagram for single crystal MgB_2 showing a $\mathrm{Mg}-\mathrm{MgB_2}$ eutectic at 840 K at 3 GPa and MgB_2 melting point around 2500 K (Turkevich et al., 2003; Karpinski et al., 2007).

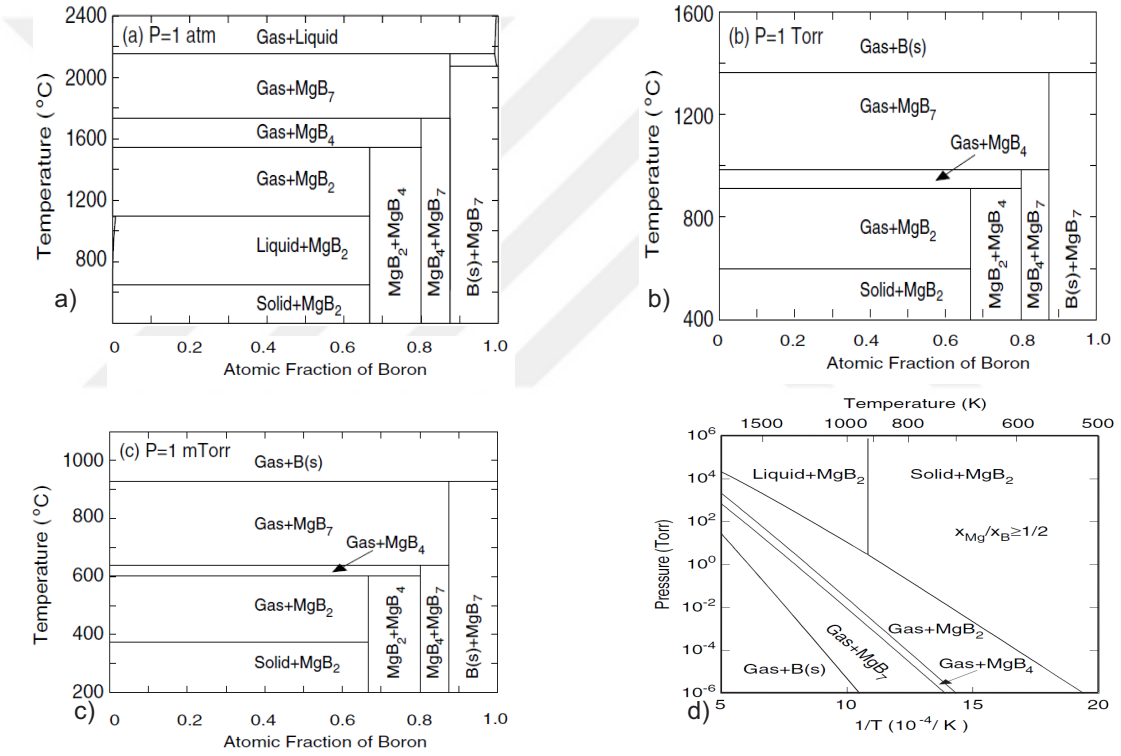

Figure 1.6. The temperature-composition phase diagrams of the Mg-B system under the pressures of a) 1 atmosphere, b) 1 Torr, c) 1 mTorr and d) The pressure versus temperature phase diagram.

1.6 Fabrication of MgB_2 Superconductors

Fabrication of MgB_2 samples in bulk, wire and tape forms is a complicated process. A number of techniques were applied for fabrication of practical MgB_2 conductors during last 15 years. Preparation of MgB_2 based superconductors using commerical MgB_2 is known as ex-situ. In the ex-situ method, commercially available reacted MgB_2 powder is used and the main advantage of the this method over in situ method is the higher density of the final product. However, the important disadvantage of this ex-situ is the poor grain connectivity (Pan et al., 2003). Planetary ball milling of the precursor powder, which leads to fine grains of MgB_2 and distributes the MgO inclusions more evenly, both have positive effects on improving the connectivity, flux pinning and J_c (Malagoli et al., 2010). Sintering at high temperature $800 - 1000^{\circ}C$ (Fischer et al., 2004) and ball milling (Suo et al., 2003) of the starting MgB_2 powder are beneficial for better grain connectivity, formation of larger number of grain boundaries, and uniform distribution of MgO impurities in the final material.

In in-situ method, high purity Mg in powder/flakes/chips and amorphous/crystalline B in powders are mixed in a stoichiometric composition, compacted to the requested form and subjected to the optimal heat treatment under argon (Ar) atmosphere for formation of MgB_2 phase (Habler et al., 2006). In-situ method offers more benefits, such as better connectivity, more efficient doping and better control over the stoichiometry, while escalating the problems of the low mass density and inhomogeneity. Mechanical alloying/high energy milling are found to enhance the formation of MgB_2 phase at relatively lower temperatures with improved superconducting properties (Senkowicz et al., 2006). High energy ball milling is efficient in reducing particle size and producing more homogeneous mixture of the ingredients.

In order to reduce the level of MgO, a number of authors have suggested replacing Mg by MgH_2 compound (Jiang et al., 2005). Since the grain boundary pinning dominates in MgB_2, formation of MgB_2 with small grains is desirable.

The size of grains can be controlled and kept small by sintering Mg+2B mixture at lower temperature ($600-650^{\circ}$C). Both ex-situ and in-site methods are used by high pressure sintering process, hot isostatic pressing process and double step sintering get highly dense MgB_2 bulk samples, etc (Prikhna et al., 2007; Wang et al., 2004; Ling et al., 2007). High pressure ($0.5-5$ Gpa) is applied in these methods during high temperature heat treatments at $700-1000^{\circ}$C. The main disadvantages are the sophisticated and costly instrumentation and limited sample dimensions. The method involves the reaction of liquid Mg with B powders in a closed metallic container (Giunchi, 2006).

Another way fabrication of high density MgB_2 is called diffusion technique, where a wire sample is first prepared with B and then Mg is made to diffuse into it during synthesis. The first superconducting MgB_2 wires were prepared by this method (Canfield et al., 2001). This process is very simple, but a long sintering time is needed to obtain sufficiently good properties. The formation of MgO is very limited in this technique, due to low MgO diffusivity. Therefore, this process offers a highly dense product with better J_c performance as a result of a larger effective cross-sectional area (Ueda et al., 2005). For practical superconductivity applications, long-length conductors are required in the form of tapes and wires. The fabrication techniques for wire and tape fabrication are the powder-in-tube (PIT) process and continuous tube forming and filling (CTFF). In the PIT technique, (in-situ or ex-situ) MgB_2 powder is packed into a tube. Heat treatment at $600-1000^{\circ}$C is usually applied to the cold processed wire to obtain superconductivity (Grasso et al., 2001). Different methods of fabrication can be used, including rotary swaging, extrusion, drawing, groove or two-axial rolling and flat rolling, which affect core density and grain connectivity (Bhatia et al., 2004; Kovac et al., 2007). The standard sheath materials are stainless steel (SS) and alloyed or pure tubes of Fe, Ni, Cu, Ag, Nb, and Ta. However, iron is material of the choice for cladding MgB_2 due to its ductility, low cost and light weight. Also compatible with (in-situ) MgB_2 up to high temperatures $T<900^{\circ}$C (Kim et al., 2006), assures wires with high density and possesses a shielding effect due to the ferromagnetic nature of Fe.

Single crystals of MgB_2 superconducting samples have been grown at ambient pressure by using Mg-self-flux method (Du et al., 2004). The most successful process has been a high pressure synthesis method at approximately 1-3 GPa and $1700 - 2200^{\circ}C$ using a graphite heater and pyrophyllite pressure medium (Lee, 2003).

The coated conductor technique is widely used for the fabrication of commercially available superconductors. High H_{c2} and J_c values in applied fields have been observed in thin films of MgB_2 superconductors (Eom et al., 2001). Abe et al. (2004) have used a processing technique called the Molten Salts Electro molten salts electroplating. Through this technique, MgB_2 can be coated to stainless steel (SS) substrates and gives higher chemical stability, plasticity and heat conductance than ceramic substrates.

2. DIFFUSION

Diffusion in solids is a fundamental topic in science of materials, solid-state physics, physical chemistry and physical metallurgy. The Latin word 'diffundere' means 'to spread out' (Mehrer, 2007), diffusion process can be defined as thermally stimulated random motion of atoms or molecules in gases, liquids and solids. Diffusion process related with the random motion of particles, this motion results in redistribution of particles moving from regions of high concentration to regions of low concentration. The diffusion is one of the best developed topics in physics.

2.1 A Historical Background

Diffusion is based on a few cornerstones, as the most important one is the Brownian motion of atoms or molecules that leads to uniform distribution if sufficient time is allocated. This kind of motion was first observed by Robert Brown in 1827 (Grey and Isaacs, 1991).

The diffusion theory was worked on by Adolf Fick (1855), who was inspired by elegant experiments on diffusion in gases and diffusion of salt in water performed by the Scotsman Thomas Graham.

The mathematical formulation of Brownian motion was done by Albert Einstein (Einstein, 1905 and 1906). The theory related the mean square displacement of atoms to the diffusion coefficient. It provided the statistical examination of diffusion and constituted a relationship between mechanics and thermodynamics. The diffusion in solid material was first studied by Roberts Austen (1896), who studied the iron-carbon phase diagram and showed the penetration of carbon inside the iron bulk.

Georg von Hevesy (1920) and co-workers performed studies of self-diffusion in liquid and solid by using a natural radioisotope of lead. The atomic diffusion in materials were detected through X-rays diffraction of crystals by Max von Laue. His experiments proved that solid matter occurs in three dimensional periodic arrangements of atoms.

The Russian physicist Jakov Ilich Frenkel presented the concept of disorder in the field of solid-state physics. He suggested that, by thermal agitation, transitions of atoms from their regular lattice sites into interstitial positions occur, leaving vacancies behind (Frenkel, 1926), this types of disorder in crystal structure is called as Frenkel disorder. Later a few years, the concept of disorder and introducing point defect thermodynamics were generalized by Wagner and Schottky (1930).

The American physicist John Bardeen was first indicated the role of correlation in defect-mediated diffusion in solids, where the defects are usually the vehicles of diffusion in a crystalline solid. If diffusion in solid would happen by random motions of the lattice atoms, the jump probabilities of atoms would be independent of the direction of the preceding jump (Bardeen and Herring, 1951) and David Turnbull carried out systematic studies of grain-boundary diffusion in solids (Hoffman and Turnbull, 1951).

Diffusion in solids is slowest, because of diffusion rates are a direct measure of the mobility of atoms. The slowness of diffusion in solids limits industrial applications to surface reactions, such as doping, carburization, sintering. Diffusion process plays a key role in the kinetics of various microstructure changes that arise during processing of metals, alloys, ceramics, semi-conductors. Technological applications of diffusion include fabrication of microelectronic devices, solid electrolytes for battery and fuel cells, surface hardening of steel through carburization, diffusion bonding and sintering.

2.2 Theory of Diffusion

The mathematical basis of the diffusion was laid by Fick, whose first law states that the rate of the transfer of diffusers through unit area is proportional to the magnitude of the

concentration gradient normal to the area. The flux of atoms in x-direction is chosen as the direction of the concentration gradient C:

$$J_x = -D\frac{\partial C}{\partial x} \tag{2.1}$$

The concentration C depends on position (x). The proportionality constant D is called the diffusion coefficient or diffusivity. Since C is expressed in terms of number of atoms per cubic meter (m^{-3}), then the unit of J_x is $m^{-2}s^{-1}$ and that of D is m^2s^{-1}. Negative sign in this formula (Equation 2.1) indicates that the concentration decreases with the distance, also using the conservation of matter. Fick derived the second fundamental law of diffusion in solids. Fick's second law is obtained by applying the continuity state to Equation 2.1;

$$\frac{\partial C}{\partial t} = D\frac{\partial^2 C}{\partial x^2} \tag{2.2}$$

From a mathematical point of view Equation 2.2 is a second order linear partial differential equation. Initial and boundary conditions are necessary for particular solutions of Fick's second law. These solutions permit the determination of D from measurements of the concentration distribution as a function of position and time.

2.2.1 Solution of Diffusion Equation

The mathematical solution of Fick's equations began with Josef Stefan and Franz Neumann (1879), they recognized the significance of boundary conditions for solutions of the diffusion equation. They give solutions for Fick's second law either as a trigonometric series or as the complementary error function.

2.2.1.1 Thin Film Solution

Thin layer is the diffusion source and solving Fick's law is subject to the condition that the total amount of plated diffuser is constant (M). Thus the diffuser layer of the sample is raised to the high temperature for diffusion to take place.

After a time (t), the distribution should be Gaussian distribution, which is expressed by

$$C(x,t) = \frac{M}{t^{1/2}}\exp\Big(-\frac{x^2}{4Dt}\Big). \tag{2.3}$$

Equation 2.3 accords to Fick's law; it is symmetrical with respect to

$x = 0, C \to 0$

$x \to \pm\infty$ for $t > 0$

and for $t = 0 \to C$ disappears everywhere, except for $x = 0$ where it is infinite. The amount of diffusing material per area (α) is constant with time according to Equation 2.3 can be expressed as;

$$\alpha = \int_{-\infty}^{+\infty} \frac{M}{t^{1/2}}\exp\Big(-\frac{x^2}{4Dt}\Big)dx. \tag{2.4}$$

The mathematical solution of that equation gives $\alpha = 2M(\pi D)^{1/2}$. The complete thin layer solution is given as;

$$C(x,t) = \frac{\alpha}{2(\pi Dt)^{1/2}}\exp\Big(-\frac{x^2}{4Dt}\Big). \tag{2.5}$$

Figure 2.1 represents Equation 2.5 for some of diffusion times, also the infinite problem is symmetrical.

The quantity $\sqrt{Dt}$, called diffusion length, is a characteristic distance for diffusion problems. The experimental determination of diffusion coefficient is by based upon Equation 2.5 and this equation can be used if $\sqrt{Dt}$ is much larger than the initial layer thickness. For many diffusion experiments the time is selected to make the penetration depth small compared to the thickness of the superconductor and semiconductor specimen (Crank, 1975).

2.2.1.2 Error Function Solution

Based on Fick's second law (Equation 2.2), the error function solution is derived by using the boundary conditions. The concentration at the unchanging surface (C_s) is constant and the concentration in bulk of the sample (C_0) is also invariant.

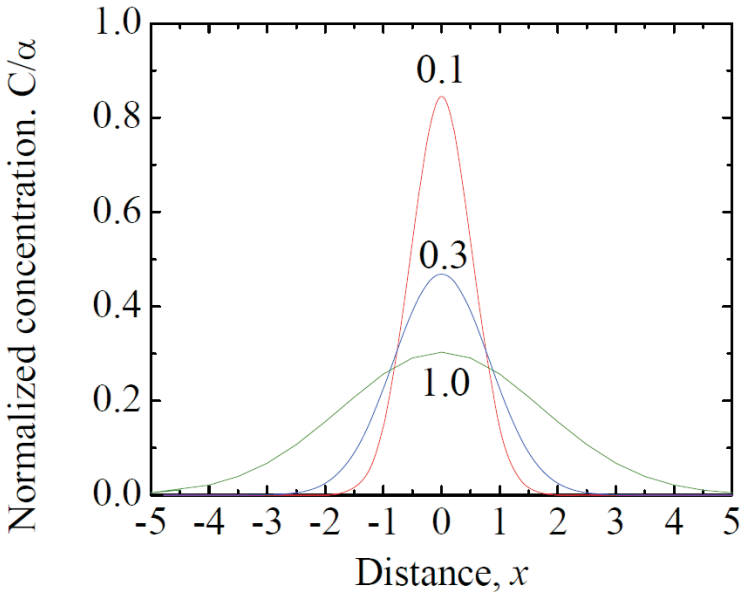

Figure 2.1. Thin-layer solution of the diffusion equation for various diffusion times (value of $0.1, 0.3$ and 1.0 s).

Thus, the sample must be large enough for an accurate solution that is;

$$C(x,t) = C_s - (C_s - C_0)\mathrm{erf}\left(\frac{x}{2\sqrt{Dt}}\right) \tag{2.6}$$

where x is the distance from the surface, D is the diffusion coefficient and t is the diffusion time. Suppose that the boundary conditions are:

$C = C_s$ for $x < 0$ at $t = 0$

$C = 0$ for $x > 0$ at $t = 0$

This problem can be easily solved and the appropriate solution is expressed as:

$$C(x,t) = C_s\left[1 - \mathrm{erf}\left(\frac{x}{2\sqrt{Dt}}\right)\right] \tag{2.7}$$

where the complementary error function is defined by

$$z = \frac{x}{2\sqrt{Dt}} \qquad \Rightarrow \qquad \mathrm{erfc}z \equiv 1 - \mathrm{erf}z \tag{2.8}$$

and

$$\mathrm{erf}z \equiv \frac{2}{\sqrt{\pi}}\int_0^z \exp(-u^2)du \tag{2.9}$$

denotes the error function. One of the general features of the erfc curve is that the value of the function is unity at $x = 0$ for all times. Figure 2.2a shows a plot of Equation 2.7, where the distance is presented in units $2(Dt)^{1/2}$.

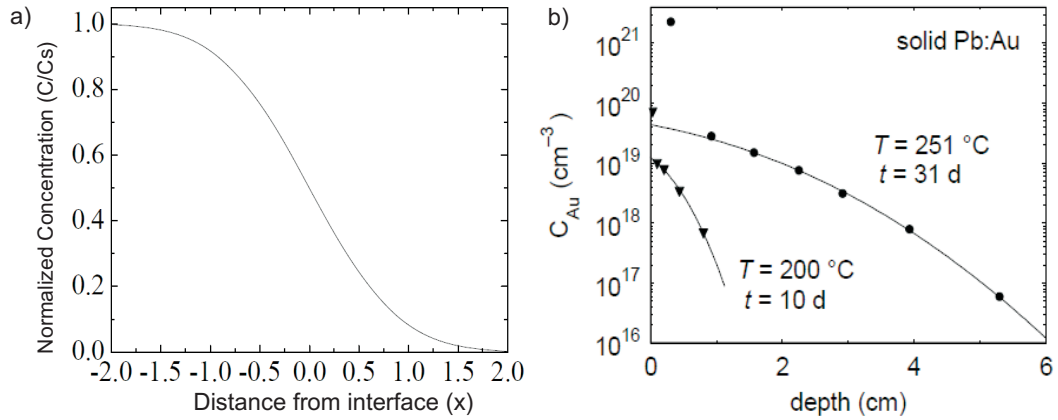

Figure 2.2. a) erf function; Gaussian error function, based on integration of the ”bell shaped” curve and b) Diffusion profiles of Au in solid.

Equation 2.7 indicates that at $x = 0$, the concentration is always $1/2C_s$ and it follows that for $x > 0$, surface concentration is kept for all times at $1/2C_s$. Figure 2.2b displays two diffusion profiles fitted by the complementary error function.

Roberts-Austen (1896) performed a series of remarkable diffusion experiments. He studied the diffusion of gold, platinum (Figure 2.2b) and rhodium in liquid lead, and diffusion of gold, silver, tin and also diffusion of gold in bismuth.

2.3 Mechanisms for Diffusion

The atoms of the crystal in a solid oscillate around their equilibrium positions. Atoms move through solids by a number of different mechanisms, such as vacancy mechanism, interstitial mechanism, interstitialcy mechanism and self-interstitial diffusion mechanism (Mehrer, 2007). Lattice diffusion process of atoms in solid phases takes place through the motion of point defects. The variation of point defects gives rise to different mechanisms of diffusion. The diffusion mechanism depends on factors such as crystal structure, solute size and intermolecular forces. The diffusion is associated with the sublattices of anions and several atomic mechanisms of diffusion in crystals have been identified in the literature.

2.3.1 Vacancy Mechanism

The diffusion process is through the vacancy mechanism, if an atom on a normal site jumps into an adjacent empty lattice site. The atoms jumping from a lattice site to other lattice site need energy, this energy comes from the thermal energy of atomic vibrations. Atom in vacancy exchange mechanism must have a vacancy on an adjacent neighboring site of the lattice or sublattice, as shown in Figure 2.3.

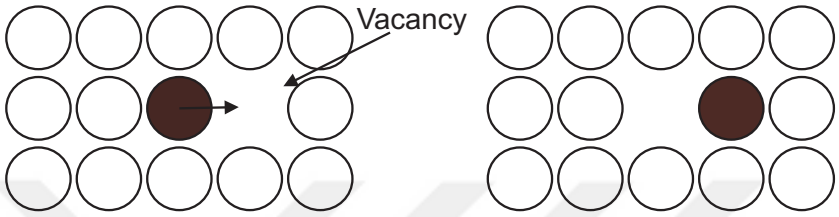

Figure 2.3. Vacancy mechanism of diffusion.

2.3.2 Interstitial Mechanism

The interstitial mechanism of diffusion is expected for atoms that normally occupy interstitial sites in a host crystal of bigger atoms, namely, indirect interstitial mechanism. The motion of the interstitial atom produce an important distortion of the lattice. This mechanism does not involve pair formation between the lattice atom and native point defects, this mechanism can give pair formation with native point defects. If the interstitial atom is smaller than the atoms on the normal lattice positions, this mechanism is possible (see Figure 2.4).

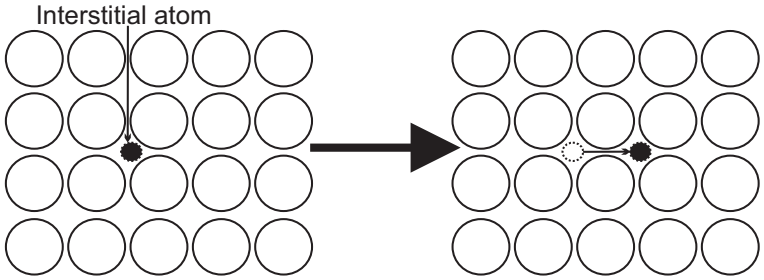

Figure 2.4. Interstitial mechanism of diffusion.

2.3.3 Interstitialcy Mechanism

The interstitialcy mechanism is associated with substitutional mechanism, and also self-interstitial atom moves into lattice site pushing the atom on that site to interstitial position and occupies the lattice site of the displaced atom, show as Figure 2.5. The interstitialcy mechanism is important for radiation induced diffusion precess.

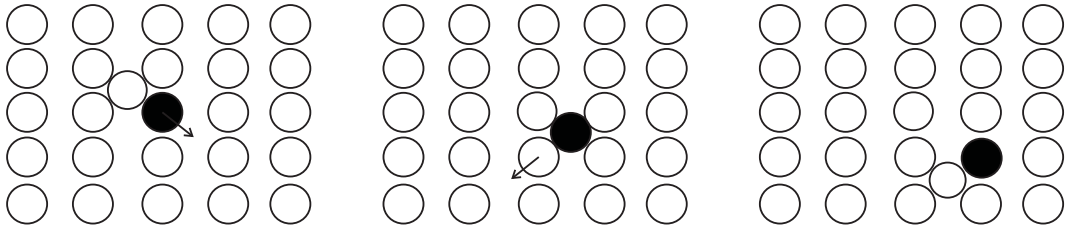

Figure 2.5. Interstitialcy mechanism of diffusion.

2.3.4 Divacancy Mechanisms

The diffusion of self-substitutional atoms in divacancy mechanisms can also happen by bound pairs of vacancies, show as Figure 2.6. The divacancies in equilibrium temperature consist of two mono-vacancies.

Otherwise, vacancy and divacancy mechanisms are very similar (Wollenberger, 1996). Vacancies are associated with dislocations and mono-vacancies are described by deformed lattice in solid.

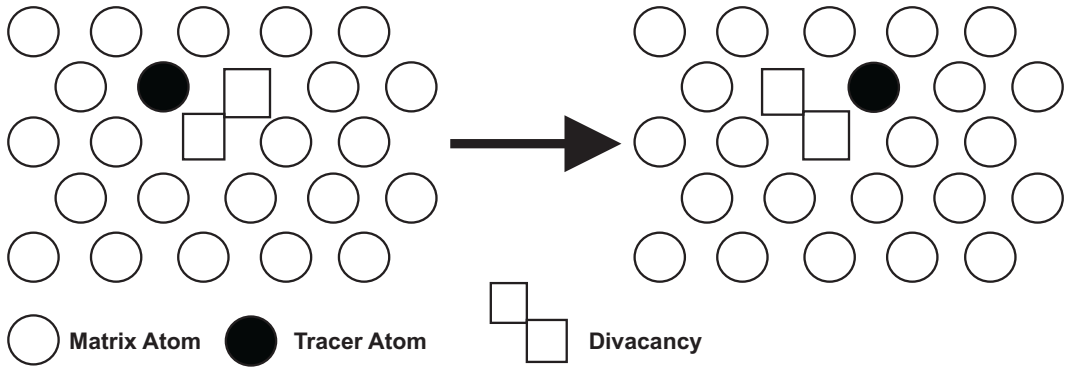

Figure 2.6. Divacancy mechanism of diffusion.

2.4 The Various Diffusivity

Diffusion process in materials is characterized by several diffusion coefficients or diffusivity. These are important parameters which demonstrate the diffusion mobility. Diffusion coefficient is given by Fick's laws, but it also exits in various other equations in physics and chemistry. In general, diffusion coefficient is predicted for a given two species and it has an SI unit of m^2/s (length^2/time).

Tracer Diffusion Coefficients

In diffusion studies with trace elements, a few diffusing species can be used as tracer for determination of diffusion coefficients. Even when the gradient in the concentration of the trace element is small, movements of atoms can be traced, and diffusion coefficient can be measured, namely, diffusion rate of these tracer atoms are called tracer diffusion coefficient.

- **Self-Diffusion Coefficient:** If the diffusion of A-atoms in a solid element A is studied, this process is self diffusion (Heitjans and Kärger, 2005). Self-diffusion issue is the basic diffusion process in a condensed matter. Self diffusion process is studied by tracer techniques.

- **Impurity Diffusion Coefficient:** When tracer diffusion coefficient of element B in pure material A is measured, it is called impurity diffusion coefficient.

Inter-diffusion (Chemical Diffusion) Coefficients

Since elements in the diffusion couple interdiffuse to each other, it is called inter-diffusion. In a binary diffusion couple atoms, the chemical composition is changing in the inter-diffusion zone. Inter-diffusion is a result of concentration gradient in the diffusion region, and composition-dependent diffusivity can be determined from concentration profiles. These profiles are analyzed by the Boltzmann-Matano method or the Sauer and Freise method (Heitjans and Karger, 2005).

Intrinsic Diffusion Coefficients

The intrinsic diffusion model can be applied by the dopant concentration which is lower than the intrinsic carrier concentration. Therefore, the diffusion rates of A and B atoms are usually different. The net effect is described by the usual Fick's laws. The intrinsic diffusion coefficients estimated from the composition profile are derived by Heumann and Walther (1957).

2.5 Temperature Dependence of Diffusion

The diffusion coefficients in solids are strongly temperature dependent and increases with raising temperature. The measurements of diffusion coefficients over temperature range is identified by Arrhenius relation;

$$D = D_0 \exp\Big(-\frac{Q}{RT}\Big). \tag{2.10}$$

The Arrhenius equation is a formula for the temperature dependence of reaction rates (Arrhenius, 1889). In Equation 2.10, D_0 is denoted as pre-exponential factor and Q as activation energy for inter-diffusion mechanism. In a Arrhenius diagram the logarithm of the diffusion coefficient is plotted versus the reciprocal temperature (1/T). For a diffusion process with a temperature-independent activation energy Q, the Arrhenius diagram is a straight line with slope $(-Q/R)$. From its intercept for $1/T \rightarrow 0$ the pre-exponential factor D_0 can be deduced, as shown in Figure 2.7.

The physical meaning of the diffusion coefficients/activation energy depends on the diffusion mechanism, type of diffusion process, and lattice geometry. The attractive and repulsive forces between solute atoms and vacancies affect the probability of a vacancy existing on a nearest-neighbor position of a solute atom in substitutional solid solutions (Mehrer, 2007). Additionally, a correlation exists between the directions of consecutive jumps and preceding jump (Balluffi et al., 2005). Such simple Arrhenius behaviour should not be a sufficient replacement, nevertheless, Equation 2.10 provides a very useful standard.

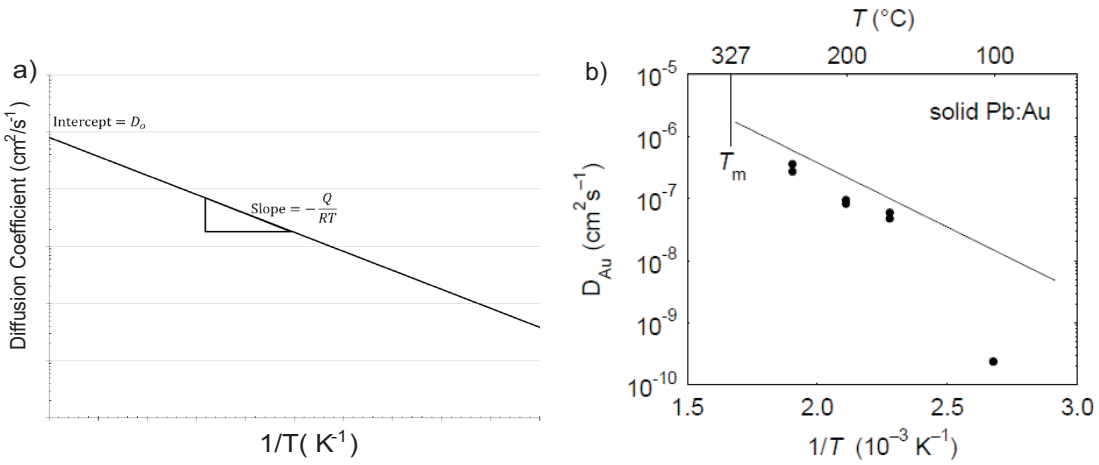

Figure 2.7. a) Schematic representation of the Arrhenius relationship between diffusivity and temperature and b) Comparison of the Au diffusivity in solid lead as reported by Roberts-Austen (1896).

2.6 Pressure Dependence of Diffusion

The variation of diffusivity with pressure P is more effective than temperature, because of the diffusivity usually decreases as the pressure is increased. The diffusivity can range from slightly to significant, while the pressure dependence of diffusion is highly variable. At a given temperature and pressure range, it can be either positive or negative, depending on the identity of the ion. As a function of pressure, the pressure dependence of diffusion were resulted by Poe and Rubie (1998). Pressure dependence of ^{198}Au diffusion in Au single crystals at constant temperature according to Werner and Mehrer (1983), as shown Figure 2.8. The diffusion coefficients in solids strongly depend on pressure, also these coefficients increase with rising pressure at constant temperature.

2.7 Time Dependence of Diffusion

A convenient starting point for this analysis is Fick's second law of diffusion, we have the following expression:

$$\frac{dC(x,t)}{dt} = D_C \frac{d^2C(x,t)}{dx^2} \tag{2.11}$$

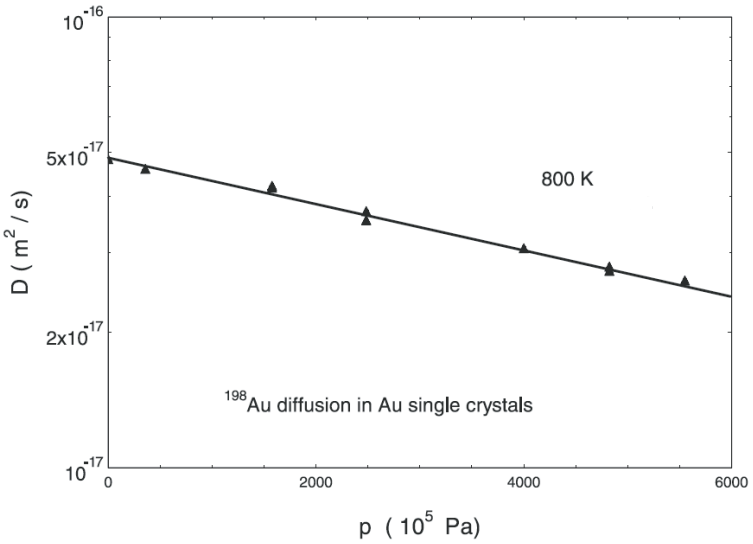

Figure 2.8. Pressure dependence of ^{198}Au diffusion in Au single crystals at constant temperature.

By solving this equation for boundary conditions, the following equation is obtained:

$$C(x,t) = C_S\left[1 - erf\left(\frac{x}{2\sqrt{Dt}}\right)\right] \tag{2.12}$$

where C_S is the concentration on the surface, and erf is the error function.

The time dependence of the diffusion coefficient is normally expressed as:

$$D(t) = D_0\left(\frac{t}{t_0}\right)^{\alpha} \tag{2.13}$$

where D_0 is the diffusion coefficient at a given time t_0, and the exponent α represents the time dependence of the diffusion coefficient. Time dependent diffusion coefficient expression is obtained by substituting Equation 2.13 into Equation 2.12, that allows the prediction based on the time dependent diffusion coefficient, given by:

$$C_x = C_S\left[1 - erf\left(x/2\sqrt{D_0 t(t/t_0)^{\alpha}}\right)\right] \tag{2.14}$$

Thus the time dependence of the diffusion coefficients can be studied by the allocation of different times for diffusion.

Theoretical considerations for the time dependence of heterogeneous diffusion have been published by Bauer et al (2009). Figure 2.9 shows the probability distribution for different times i.e., variation of concentration profile with time (Falk et al., 2004).

Figure 2.9b shows that the slope of this line can be used to calculate the diffusion coefficient (D).

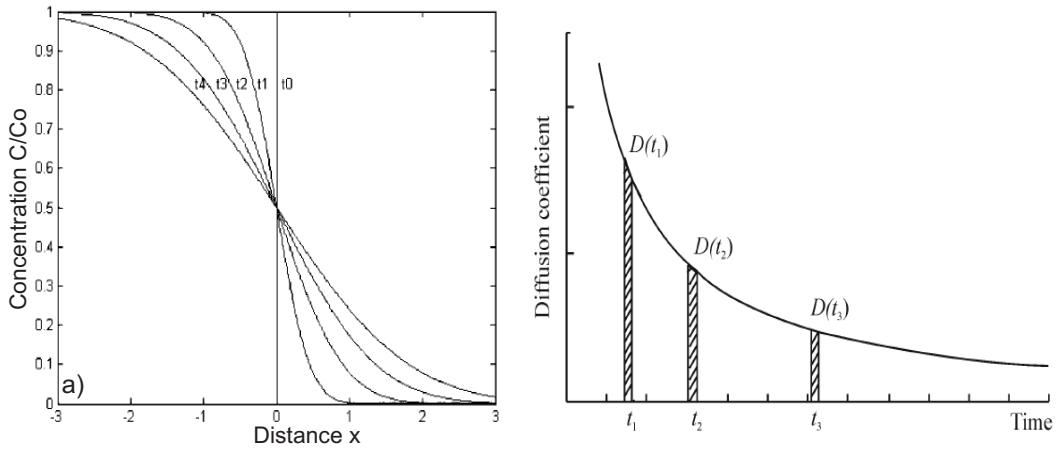

Figure 2.9. a) Distribution for different times including, initial time t_0 and b) Time dependency of instantaneous diffusion coefficients (Luguang et al., 2013).

The error function complement is used to integrate from right to left and to display the data from one to zero. This equation has been derived from statistical distribution of randomly moving molecules, atoms or ions and it is same as the solution for second Fick's law, which is based on concentration gradient and constant amount of diffusing substance. The most important experimental results, which must be explained theoretically, are as follows.

- Diffusion rate of distance/time dependence.
- Sharp concentration profile.
- Constant concentration behind the diffusion front.
- Dependence on thickness of coating.
- Filling up of voids and precipitation.
- Swelling-changes in microstructure.
- Molecular interactions-different behaviour of different compounds.

2.8 Diffusion of MgB_2 Material

The use of MgB_2 material in today's technological applications is rapidly increasing and gaining importance. Diffusion processes in the development of superconducting materials has a vital place. The diffusion is used in processing of superconductors in two essential ways (Goretta and Chen, 2000);

1. mass transport during consolidation by sintering processers
2. diffusion between superconductors and sheaths or substrates.

Diffusion is much more rapid through a liquid phase than a solid phase. The concentration of intragranular porosity is generally smallest for the samples that are sintered at the lower temperature, these samples also exhibit the slowest rates of grain growth (Goretta et al., 1992).

Sarıtekin et al. (2014) have examined physical features of Ag diffused MgB_2 superconductors such as micro-structural, mechanical and superconducting properties. They have obtained the diffusion coefficient and activation energy for Ag diffusion in MgB_2 systems by resistivity measurements. They have reported that the activation energy is ~ 1.05eV and diffusion coefficient increases from 9.34×10^{-8} to 9.58×10^{-7} cm^2/s as the sintering temperature increases from 650°C to 850°C.

Dogruer et al. (2013a) have investigated the influence of Cu diffusion on microstructural and mechanical properties of bulk MgB_2 superconductors and determined the diffusion coefficient and activation energy of Cu diffusion in MgB_2 materials. In their paper, the magnitude of the diffusion has been reported to change between 2.84×10^{-8} and 3.22×10^{-7} cm^2s^{-1} with the activation energy of nearly 1.09 eV.

According to Terzioglu et al.(2013), microstructural, superconducting and mechanical properties of the Cu diffused bulk MgB_2 superconductors depend strongly on the annealing time, and they have reported the maximum diffusion coefficient to be about 2.58x10^{-7} cm^2/s.

Altin et al. (2011) have studied the MgB_2 fabrication by diffusion-controlled three layered (B-Mg-B) technique. They determined the diffusion coefficient using Fick's law and EDX data. The coefficient diffusion of B in Mg matrix and that of Mg in B matrix was calculated as 1.66x10^{-7} and 3.14x10^{-8} cm^2s^{-1}, respectively. The highest T_c value (39.4 K) of MgB_2 material was achieved at 800°C/1h.

DeFouw et al. (2008), assays on the kinetics of MgB_2 synthesis in situ by synchrotron X-ray diffraction, using pressed compacts of $200-400$ μm magnesium powders mixed with three types of submicrometer, amorphous, high-purity boron powders. The reaction times can be defined by the diffusion controlled models of a reacting sphere with kinetics characterized by diffusion coefficients increasing with temperature from 2x10^{-13} to 3x10^{-12} cm^2s^{-1}, with activation energies of $1.2-1.5$ eV.

Samuely et al. (2007) studied electron doping and scattering effects via aluminum and carbon substitution in MgB_2. They have proved that, the decline in diffusion coefficient at the π indicates in the carbon doping, while the Al substitution leaves the sample in the clean limit. Also, an increase in the ratio of the diffusion coefficient D_σ/D_π leads shift according to the dirty limit theory.

There has been an enormous effort to improve the superconducting properties by partial substitution and diffusion in HTS (Dzhafarov et al., 1995; Prabitha et al., 2005). Dzhafarov and his group calculated the silver diffusion coefficient in superconducting samples over the different temperature by using the technique of successive removal of thin layers and measurement of the sample resistivity at room temperature.

3. AIM AND SCOPE OF THE STUDY

Motivation

The present study investigates important aspects of the interaction between MgB_2 superconductor and Fe coated layer.

Due to high superconducting transition temperature T_c, weak-link free grain coupling and low raw material cost, MgB_2 superconducting materials have been a strong competitor for electric power and magnet applications at temperatures around 20 K. However, the application brings some certain requirement on mechanical, electrical, and superconducting properties of MgB_2.

For technological applications, it is essential to fabricate high performance MgB_2 bulks and wires. When Fe or stainless steel sheathing material comes into contact with superconducting MgB_2 core, iron diffusion becomes an important issue. For brittle intermetallic high current carrying superconductors a conventional diffusion process should be more advantageous (Glowacki et al., 2001).

Figure 3.1 presents the XRD patterns of the Fe sheath removed mechanically monofilament MgB_2/Fe wire, and the remaining MgB_2 core. A diffusion layer of FeB or Fe_2B has been observed at the interface of the sheath material and MgB_2 core (Pachla et al., 2004). MgB_2, MgO, Fe, and Fe_2B were detected within the surrounding Fe sheath. The XRD results obtained will give recommendations with regard to diffusion since the Fe is used most often as the sheathing material for MgB_2.

Since iron diffusion rate into MgB_2 is a temperature and time dependent phenomenon, it will be an important parameter for sintering of MgB_2 wires/tapes. The main purpose of this work is to optimized the superconducting properties and perfor-

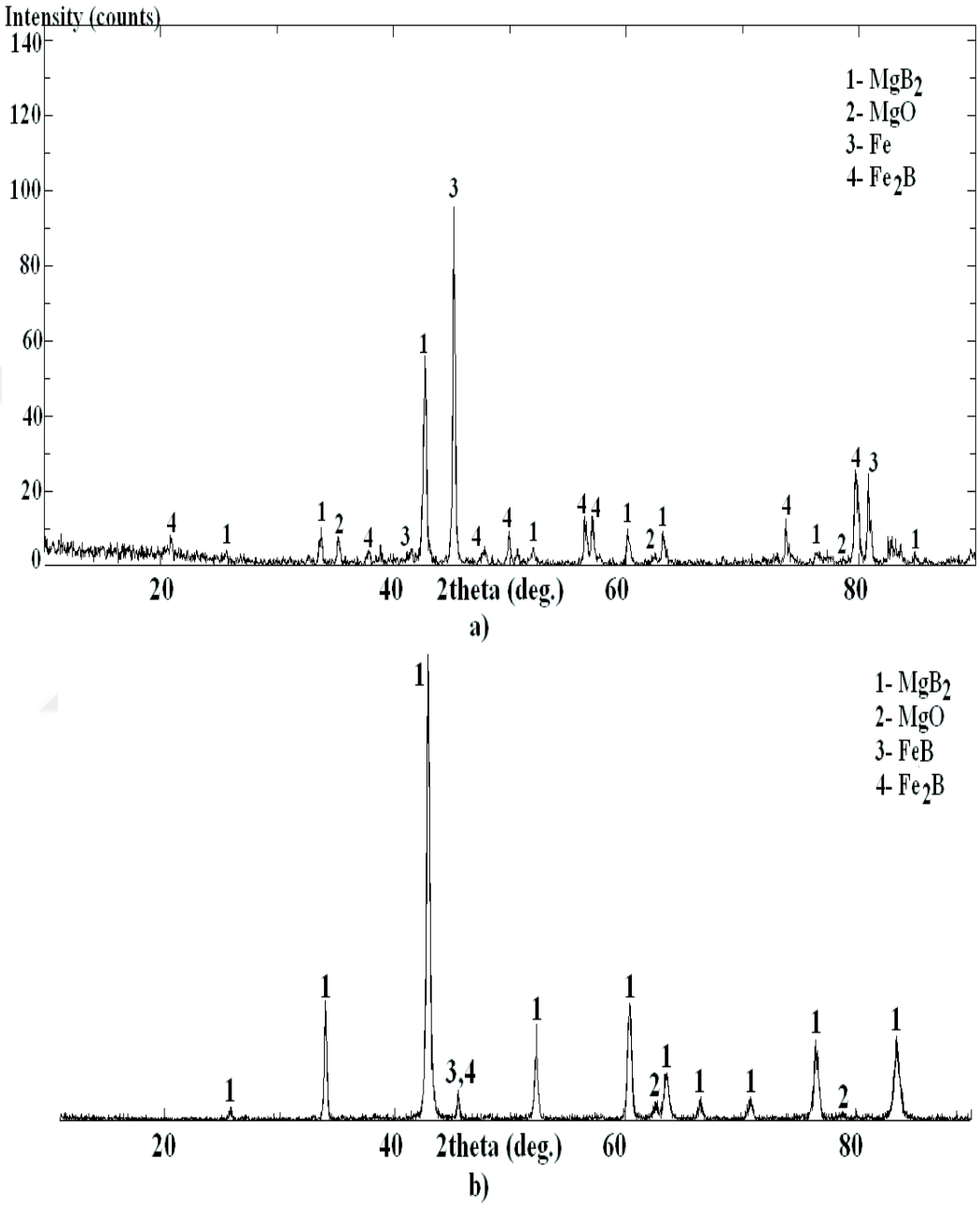

Figure 3.1. XRD patterns for a) Fe sheath and b) MgB_2 core sample.

mances by factors of heat treatment temperature and heat treatment time. At the same time, microstructural, physical and superconducting properties were investigated in ex-situ MgB_2 bulk superconductors.

The vacuum evaporation method is a simple reproducible operation in diffusion studies and it provides a controlled doping process at low concentrations. Diffusion of some metals in high-temperature superconductors have been studied by vacuum evaporation methods and reported in the literature with detailed calculations of diffusion coefficient and activation energy values (Gorur et al., 2005; Terzioglu et al., 2009; Ozturk et al., 2012).

To our knowledge of the literature, there has not been any detailed study published on the diffusion coefficient and activation energy of Fe diffusion in MgB_2 bulk samples.

In this thesis, we have studied the effect of Fe diffusion on the microstructural and superconducting properties of MgB_2 bulk superconductors. We have also determined the diffusion coefficients and the activation energies of Fe diffusion in bulk samples of MgB_2.

4. MATERIALS AND METHODS

In this chapter, fabrication process for pellets of ex-situ MgB_2 bulk samples and vacuum coating of these bulk pellets by evaporation of Fe metal are described. The coating process was applied by evaporation of Fe metal in vacuum using AUTO 306 vacuum coater (EDWARDS). Then the examination methods and techniques for the samples studied are introduced, including X-ray diffraction (XRD), scanning electron microscope (SEM), energy dispersive spectroscopy (EDS), and electrical resistivity measurements either in a closed cycled He cryostat or at room temperature.

4.1 Fabrication Process of MgB_2 Bulk Samples

All the polycrystalline MgB_2 bulk samples were fabricated by standard solid state reaction technique using high purity ex-situ powders with 99.95% purity (Alfa Easer). In order to minimize the oxidation and to produce homogeneous powder, the mixture of MgB_2 powders were mixed and grounded in agate mortar for 30 minutes in a glove box under Ar atmosphere. After that, these powders were further ball-milled under high purity Ar atmosphere for 3 hours. The powders were pressed into rectangular bars of 25x4x2 mm^3 with a pressure of 400 MPa ambient conditions.

This pressing process to obtain rectangular shaped samples was carried out in air in order to increase their density and the connection surface area of the grains. The amount of powder used for every sample was about 0.6 g each time. The fabrication process is shown schematically in Figure 4.1.

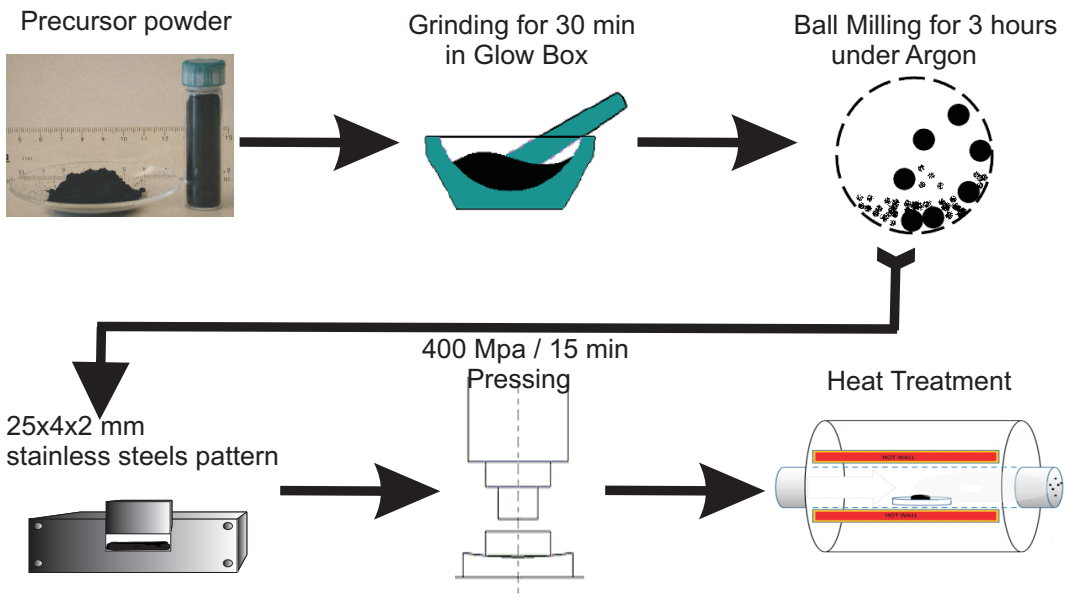

Figure 4.1. Schematic illustration of fabrication process for the ex-situ MgB_2 bulk samples.

4.1.1 Heat Treatment Process

The MgB_2 bulk samples were annealed either for 1 hour at different temperatures of 650°C, 700°C, 750°C, 800°C, 850°C, and 900°C (see, Table 4.1) or for different durations of 15 minutes, 30 minutes, 1 hour, 2 hours, 4 hours and 8 hours at 900°C (see, Table 4.2). Heat treatments were performed under Ar gas at 5-10 bar pressure using a horizontal tube furnace (Protherm-Model PTF12/75/200). For annealing process of the bulk samples, a stainless steel tube with vacuum and Ar gas inlets was used.

After placing the samples of MgB_2, the steel tube was evacuated to remove the air inside, then the tube was filled with Ar at 3 bar pressure and re-evacuated. This process of washing with Ar gas was repeated 3 times. After washing operation is completed completed, the tube was filled with 5 bar of Ar pressure at room temperature. The Ar pressure inside the sintering chamber of the tube increased up to more than 10 bar.

Set temperature of the system was determined measuring the real temperature inside the steel tube at the position where the samples are placed and then the furnace was set to the determined temperature for heat treatments.

The heating and cooling rates are adjusted to be 5°C/min. A temperature-time profile for the annealing of MgB_2 bulk are shown in the Figure 4.2. The temperature profile along this furnace was determined with a thermocouple and calibrated. The profile can be summarized as having three parts, as

1. Between 0 and t_1; 'Heating Period' which includes heating from room temperature to the sintering temperature (T_s).

2. Between t_1 and t_2; 'Sintering Duration' which the furnace is kept at a constant temperature.

3. Between t_2 and t_3; 'Cooling Period' which includes fall of temperature down to room temperature.

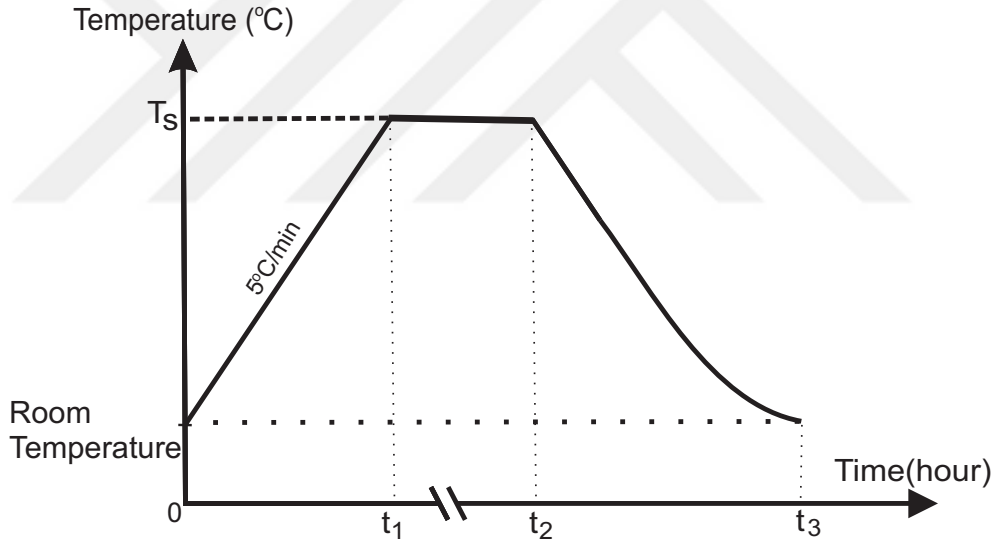

Figure 4.2. Temperature-Time profile for sintering of MgB_2 bulk samples.

4.1.2 Fe Coating Process of MgB_2

Coating is applied on bulk pellets by evaporation of Fe metal films using EDWARDS-Auto 306 Vacuum Coating Systems under $1x10^{-4}$ Pa vacuum. As shown in Figure 4.3, the Auto 306 is designed for physical vapour deposition processes under high vacuum. Resistance evaporation is often simplest, and most effective deposition technique.

In this technique, commonly used metals such as iron, chromium, silver, gold and many others are readily evaporated. Figure 4.3b show that single resistance source for filament/boat evaporation.

An about 50 μm thick coated layer was deposited by Fe evaporation on wide face (25x4 mm^2) of the samples using tantalum boat with 0.1 mm thickness. For each evaporation process, a 15 cm long iron wire with a diameter of 0.1 mm (∼0.01 g) was used (Alfa Easer, purity 99.99%). The photographs in Figure 4.4 show surfaces of Fe coated and un-coated (Bare) MgB_2 bulk samples on the aluminum grid.

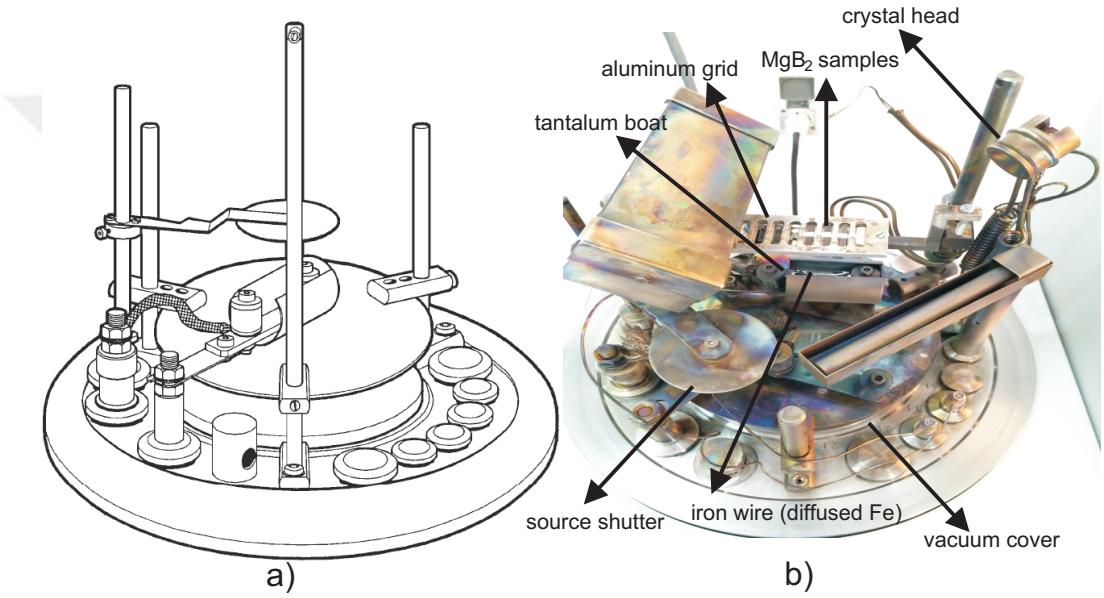

Figure 4.3. a) Schematic diagram of the deposition region and b) Photograph of the evaporation chamber.

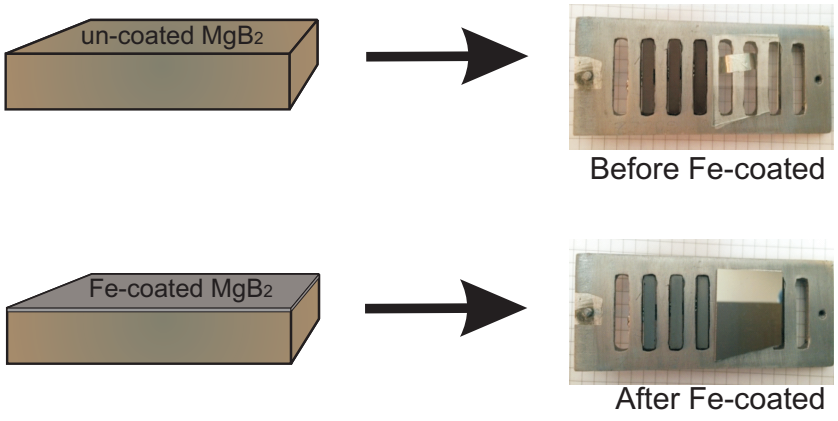

Figure 4.4. MgB_2 pellets before and after Fe coating.

4.2 Experimental Set-up

Fe coating process on the polycrystalline superconducting MgB_2 pellets were applied either on initially sintered pellets or on pressed pellets without initial sintering. The pelletized MgB_2 bulk samples were divided into two groups.

The pellets in one group were sintered at 800°C for 1 hour, in order to obtain larger and connected grains, this process is called initial sintering. The pellets of the other group were used without initial sintering.

We prepared four sets of pelletized MgB_2 bulk samples for our experiments. Each set contained Fe coated and bare bulk pellets for comparison. The bare samples of Set 1N sintered at the same temperatures for 1 hour are coded as NB165, NB170, NB175, NB180, NB185 and NB190, as in all samples, the last two digits indicate sintering temperature.

In these codings, S stands for initial sintering, N for no initial sintering, F for Fe coating and B for not coated bare sample. Samples of Set 1 and Set 2 were used for sintering temperature and sintering time experiments, respectively. Details are as follows:

- **Set 1S**; initially sintered samples (Fe coated or bare) used for different sintering temperature experiments,
- **Set 1N**; not initially sintered samples (Fe coated or bare) used for different sintering temperature experiments,
- **Set 2S**; initially sintered samples (Fe coated or bare) used for different sintering time experiments,
- **Set 2N**; not initially sintered samples (Fe coated or bare) used for different sintering time experiments.

4.2.1 Sample Codes for Diffusion at Different Temperatures for 1 hour

In the Table 4.1 and Figure 4.5, Fe coated MgB_2 samples of Set 1S were sintered at different temperatures of 650°C, 700°C, 750°C, 800°C, 850°C, and 900°C for 1 hour. These samples are denoted as SF165, SF170, SF175, SF180, SF185 and SF190, the last two digits indicating sintering temperature.

Likewise, bare samples of Set 1N were sintered at the same temperatures and are denoted as SB165, SB170, SB175, SB180, SB185 and SB190. Similarly, Fe coated MgB_2 bulk samples of Set 1N were sintered at 650°C, 700°C, 750°C, 800°C, 850°C and 900°C for 1 hour and herein after denoted as NF165, NF170, NF175, NF180, NF185 and NF190, respectively.

Table 4.1. Samples annealed at different temperatures for fixed time (1 hour).

Samples Code for Set 1S	Time (hour)	Temp. (°C)	Initial Sintering 800°C/1h	**Samples Code for Set 1N**	Time (hour)	Temp. (°C)	Initial Sintering 800°C/1h	Coating Process
SB165	1hr	650	√	**NB165**	1hr	650	**X**	No
SF165	1hr	650	√	**NF165**	1hr	650	**X**	Yes
SB170	1hr	700	√	**NB170**	1hr	700	**X**	No
SF170	1hr	700	√	**NF170**	1hr	700	**X**	Yes
SB175	1hr	750	√	**NB175**	1hr	750	**X**	No
SF175	1hr	750	√	**NF175**	1hr	750	**X**	Yes
SB180	1hr	800	√	**NB180**	1hr	800	**X**	No
SF180	1hr	800	√	**NF180**	1hr	800	**X**	Yes
SB185	1hr	850	√	**NB185**	1hr	850	**X**	No
SF185	1hr	850	√	**NF185**	1hr	850	**X**	Yes
SB190	1hr	900	√	**NB190**	1hr	900	**X**	No
SF190	1hr	900	√	**NF190**	1hr	900	**X**	Yes

4.2.2 Sample Codes for Diffusion for Different Sintering Times at 900°C

Coated and bare bulk samples annealed at 900°C for experiments on sintering time. Sintering time durations in these experiments are 15 minutes, 30 minutes, 1 hour, 2 hours, 4 hours, or 8 hours as given in Table 4.2 and Figure 4.6. The coated samples of Set 2S were sintered at different temperatures and they are denoted as SF1590, SF3090, SF190, SF290, SF490 and SF890, the last two digits indicating sintering temperature as explained before and the preceding numeral(s) indicate(s) sintering time. Likewise, the bare samples are presented as SB1590, SB3090, SB190, SB290, SB490 and SB890. Similarly, Fe coated samples of Set 2N are denoted as NF1590, NF3090, NF190, NF290, NF490, NF890, and the bare ones as NB1590, NB3090, NB190, NB290, NB490, NB890.

Table 4.2. The coding system in different times at fixed temperature (900°C).

Samples Code for Set 2S	Time (min) (hour)	Temp. (°C)	Initial Sintering 800°C/1h	**Samples Code for Set 2N**	Time (min) (hour)	Temp. (°C)	Initial Sintering 800°C/1h	Coating Process
SB1590	15 min	900	√	**NB1590**	15 min	900	**X**	No
SF1590	15 min	900	√	**NF1590**	15 min	900	**X**	Yes
SB3090	30 min	900	√	**NB3090**	30 min	900	**X**	No
SF3090	30 min	900	√	**NF3090**	30 min	900	**X**	Yes
SB190	1 hr	900	√	**NB190**	1 hr	900	**X**	No
SF190	1 hr	900	√	**NF190**	1 hr	900	**X**	Yes
SB290	2 hr	900	√	**NB290**	2 hr	900	**X**	No
SF290	2 hr	900	√	**NF290**	2 hr	900	**X**	Yes
SB490	4 hr	900	√	**NB490**	4 hr	900	**X**	No
SF490	4 hr	900	√	**NF490**	4 hr	900	**X**	Yes
SB890	8 hr	900	√	**NB890**	8 hr	900	**X**	No
SF890	8 hr	900	√	**NF890**	8 hr	900	**X**	Yes

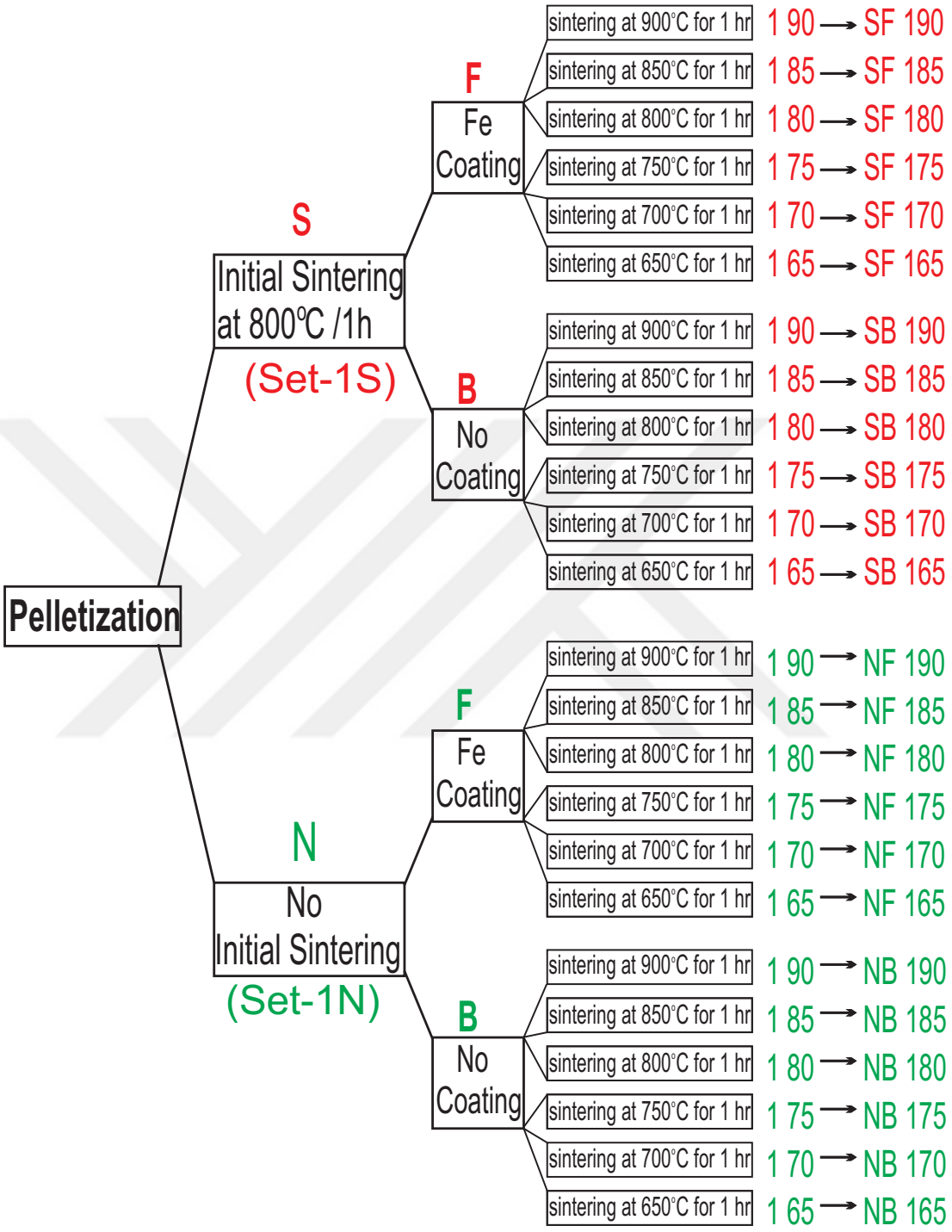

Figure 4.5. Schematic diagram showing the sample codes for annealing at different temperatures for 1 hour.

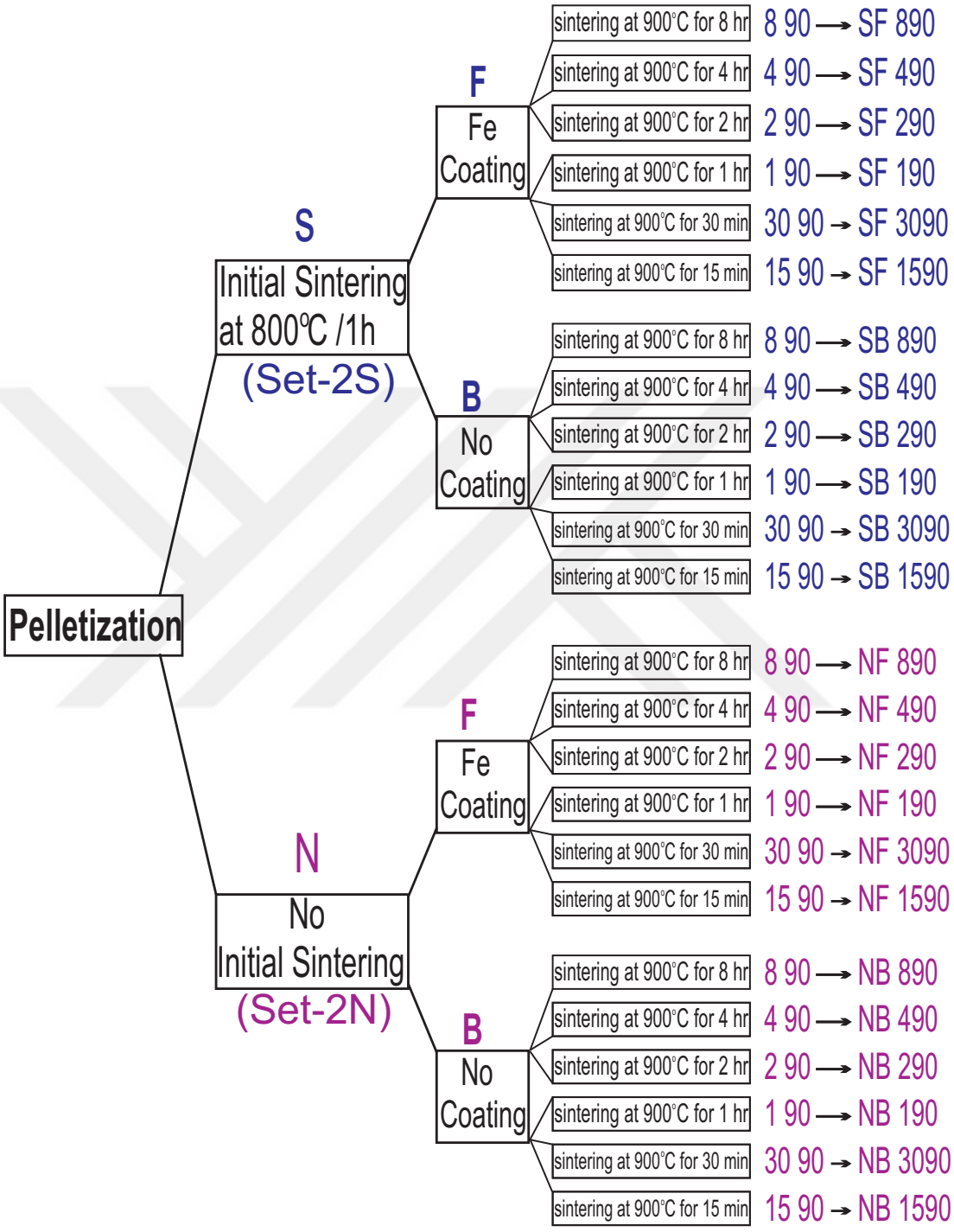

Figure 4.6. Schematic diagram of different sintering times at 900°C.

4.3 Removal Process

For each set of MgB_2 samples, removal of surface layer was achieved by rubbing against an unused fine grinding paper (P2000 and P3000) under 1.5 N weight. By applying constant weight and rubbing on an unused grinding paper just once for constant length, we achieved almost equal removals of 25 μm layer from the coated surface (Figure 4.7).

XRD and room temperature measurements for determination of diffusion coefficients were repeated after each removal of $\sim$25 μm layer. Ground surface of the sample was cleaned after grinding process with pressurized air stream before XRD and resistivity measurements at room temperature.

Following the cleaning process, room temperature resistivity of the sample was measured using four point contact configuration. In the following step, XRD pattern of the sample was obtained. These steps were repeated eight times in order to study the depth profile on the Fe coated surface, down to a depth of 200 μm in 8 steps.

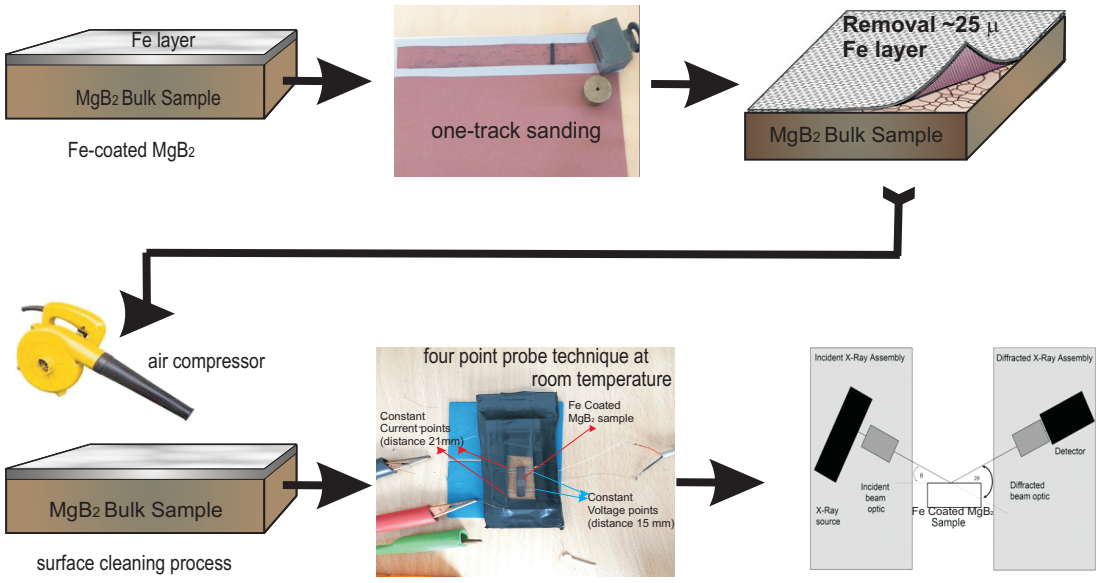

Figure 4.7. Work flow chart for each step.

4.4 Sample Characterization

4.4.1 XRD Analysis

X-ray diffraction was used to study on the crystal structures of samples. We used x-ray diffractometer (Rigaku Multi-Flex 2kW diffractometer) to determine the phase type, phase composition and the lattice parameters a and c of the Fe coated MgB_2 samples. We used X-ray radiation emitted by Cu target with characteristic wavelength (K_α) for the radiation is $\lambda = 1.5406$ Å. XRD data were collected from $2\theta = 10^\circ$ to 90° with a constant scan speed of 5°/min and step increment of 0.02° at room temperature.

The XRD measurements of the commercial MgB_2, Fe_2B and Fe powders used in preparation of the MgB_2 sample, were also made for comparison. The corresponding XRD patterns are given in Figure 4.8. The peaks marked by miller indices belong to MgB_2 and a small amount of MgO impurity phase was observed and marked on XRD patterns by "o".

Recent studies show that pure Fe_2B nanoparticle was achieved mechanochemicaly (Simsek, 2014 and Mustapic et al., 2010). Some FeB_2 peaks marked by "♯" also appear in the XRD patterns of our samples. The presence of FeB_2 peaks in XRD pattern of Fe coated MgB_2 samples are observed for all annealing temperatures. We note that the MgO impurity phase is also seen in the XRD pattern of commercial MgB_2 powder. Other phase formations such as MgB_4, MgB_7 and MgB_{12} were not found in the XRD patterns of the samples processed using different temperatures and times.

The lattice parameters a and c were calculated from the positions of the (100)&(110) and (101)&(002) MgB_2 peaks, respectively. The accuracy in determining the lattice parameters a and c was ± 0.001 Å. Wide-angle x-ray scattering is a common method for the determination of the average grain size of the microstructure of a real crystalline structure. Advanced methods like the Warren-Averbach analysis can be used for determination of a volume averaged and an area averaged mean grain size (Warren, 1990).

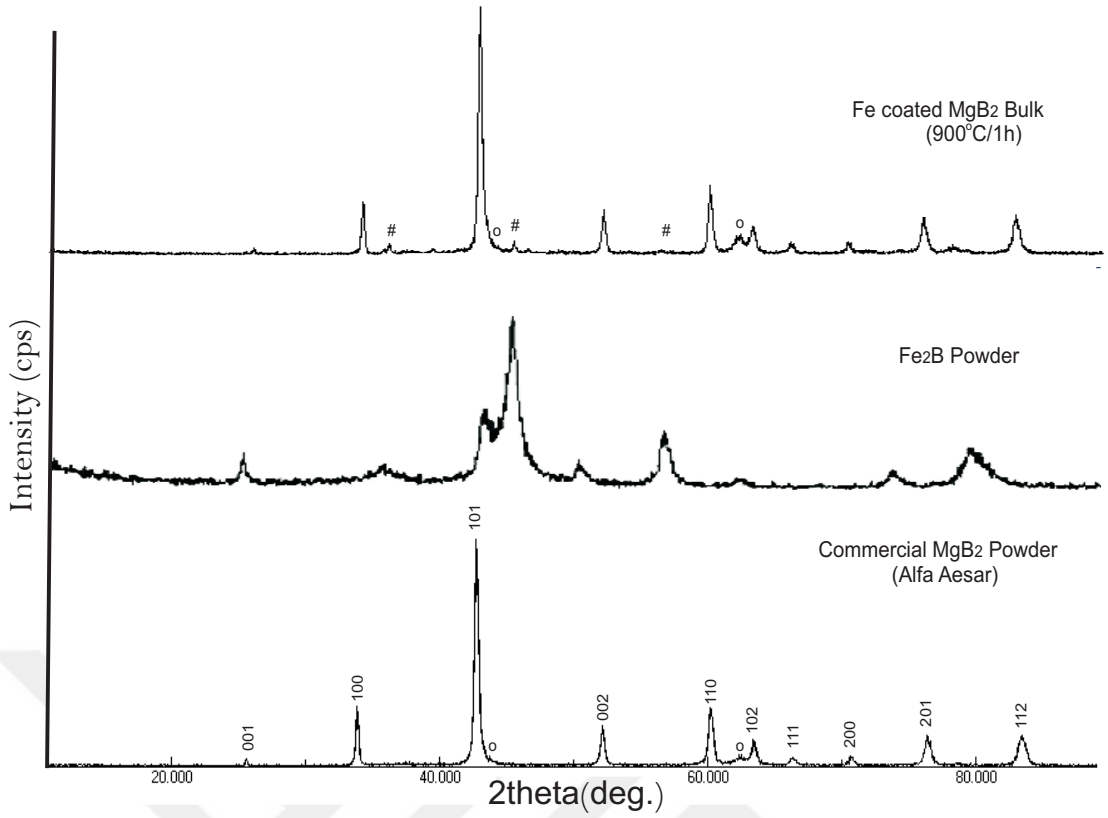

Figure 4.8. X-ray diffraction from lattice planes (Cullity and Stock, 2001).

The crystallite size of the samples were also estimated from XRD patterns using the Scherrer equation in the angstrom scale

$$d = \frac{k\lambda}{\beta \cos\theta_0}. \tag{4.1}$$

The average size of a crystal in the broadening region is defined as in Equation 4.1, where d is the thickness of the crystal, k is a constant, β means the full width at half maximum (FWHM) and θ_0 is the angular position of the peak maximum.

Besides, Warren formula is given by

$$\beta^2 = \beta^2_{\text{observed}} - \beta^2_{\text{reference}}, \tag{4.2}$$

where $\beta_{\text{reference}}$ denotes the half width of the standard material in radians.

4.4.2 Scanning Electron Microscopy (SEM) and Energy Dispersive Spectrum (EDS) Analysis

Scanning Electron Microscope (SEM) is a standard analytical tool for evaluating morphological characteristics of materials like, homogeneity, porosity and roughness. The surface morphology, grain size estimation of bare and Fe coated MgB_2 samples were investigated by the JEOL 6390-LV scanning electron microscope. The instrument is also equipped with Energy Dispersive Spectroscopy (EDS).

The EDS provides qualitative identifications of the chemical elements existing in the superconducting samples. SEM and EDS measurements were carried out at room temperature under vacuum using accelerating voltage of 20 kV at various magnifications.

SEM in a combination with EDS were used in order to carry out investigations on the stoichiometry and the chemical content of our Fe coated/diffused MgB_2 samples. These EDS results were compared with XRD patterns in which Fe_2B and MgO peaks were identified.

4.4.3 Current-Voltage (I-V curve) Measurements at Room Temperature

Current-voltage (I-V curves) measurements were performed at room temperature. The experimental setup used for the room temperature resistivity measurements is illustrated in Figure 4.9 and electrical resistivity of the MgB_2 superconducting samples were calculated from I-V curves. Current run through the sample was between 0 A and 0.5 A with increments of 0.01 A. All measurements were conducted under PC control via IEEE-488 interface. Keithley-2182A (nano-voltmeter) and Keithley-2700 (current source) were used to record the sample's voltage and to run the test current. The nano-voltmeter was triggered for a maximum resolution of 61/2 digits.

The dimensions of the Fe coated MgB_2 samples were carefully measured with a micrometer to calculate the cross sectional area after every grinding on a sand paper for removal of 25 micron surface layer. The measurements of room temperature resistivity, namely ρ_{300K}, were performed on all samples applying 2.94 N pressure for better mechanical contact. We determined resistance (R) of the samples from I−V curves by linear curve fitting and calculated resistivity values.

Room temperature resistivities of Fe coated and bare MgB_2 superconductor samples were measured. Dept profile for all Fe coated samples was obtained for determination of diffusion coefficient. Only one bare sample was studied for depth profile by successive removal of layers from the surface in order to compare with the coated samples. Moreover, the diffusion coefficient of Fe diffusion into MgB_2 was studied by determination of resistivity at room temperature after the successive removal of thin layers from the surface.

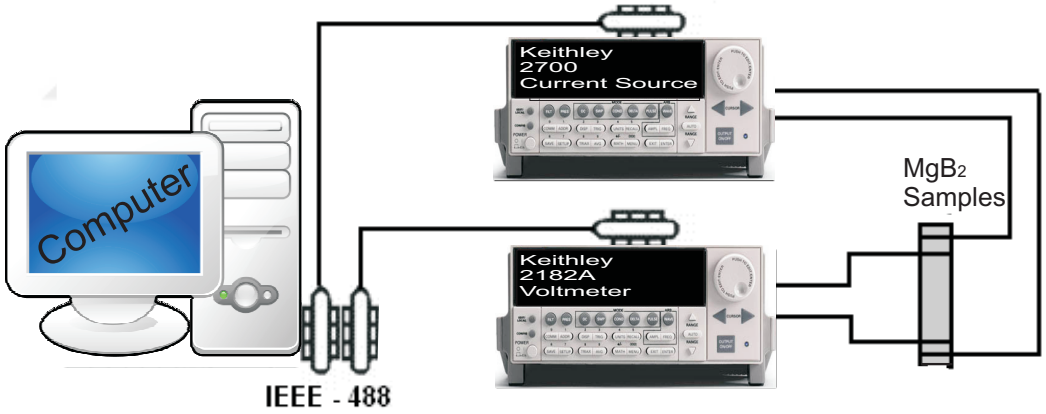

Figure 4.9. Schematic diagram of the current-voltage measurements system at room temperature.

4.4.4 Critical Transition Temperature (T_c)

Measurement of resistance versus temperature is standard method for transport critical temperature measurements (Figure 4.11). The resistivity measurements of the bulk samples were carried out by standard four probe technique.

Both voltage and current contacts were made with silver paint to minimize the contact resistance. MgB_2 samples with and without Fe coating were placed into closed cycle cryostat after making the contacts (see, Figure 4.10). We measured temperature dependence of resistivity running 50 mA dc test current through the samples in the temperature range from 10 to 45 K. A Keithley 220 programmable current source and a Keithley 2182A nanovoltmeter were used. All the data were recorded by Labview software.

T_c^{offset} is defined as highest temperature with zero resistivity and T_c is determined using first derivative of the resistivity as a function of temperature where it has maximum value. The nanovoltmeter was triggered for a maximum of 61/2 digits, and its buffer was read directly within the integration time of 1000 ms, in order to reduce any artificial effects and improve accuracy. The measured MgB_2 sample voltage value was the average value of 5 readings for each data point. The sample holder is shown in Figure 4.10b. The distance between current leads and voltage leads are 21 mm and 15 mm. Figure 4.11 shows the definition of different T_c values based on the resistive transport measurement method.

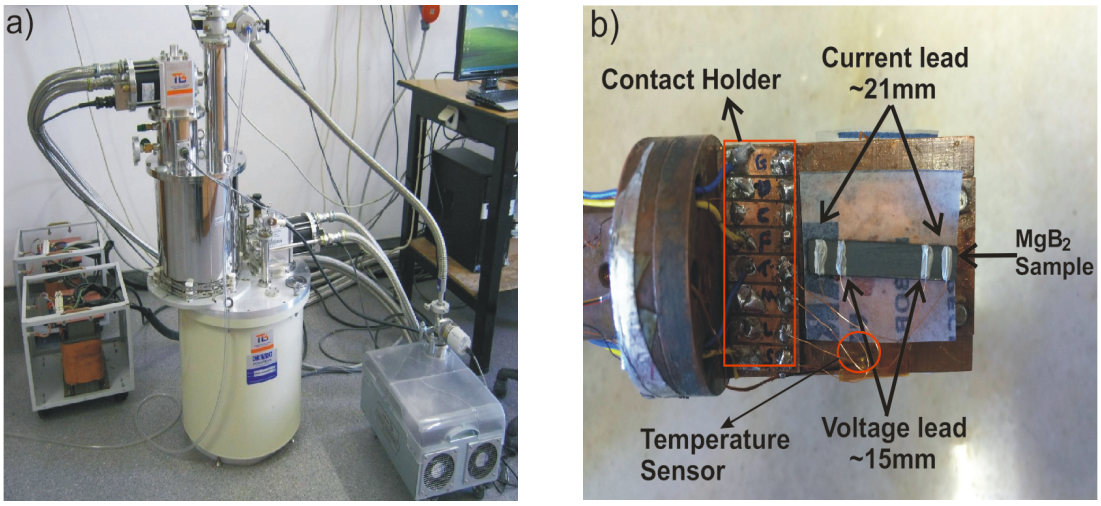

Figure 4.10. a) The closed cycle He cryostat (CRY Industries) and b) The sample holder for transport resistance measurement.

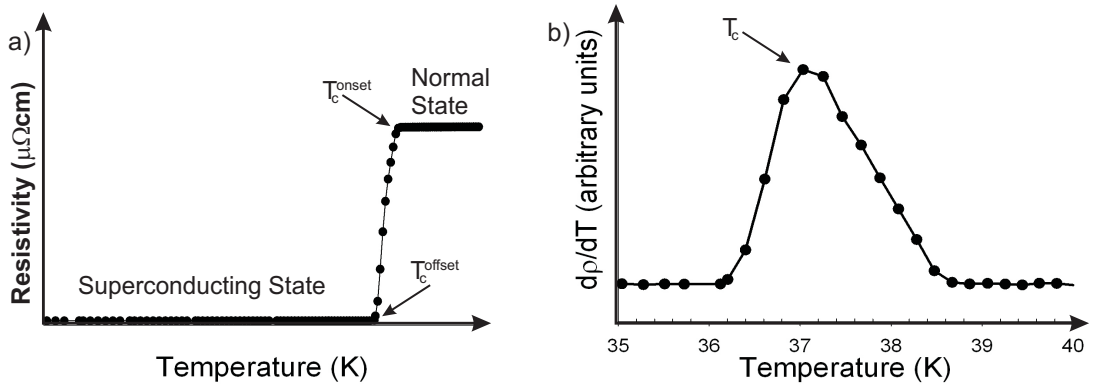

Figure 4.11. Illustration of different critical temperatures on resistivity vs. temperature curve T_c from a) The temperature dependence of resistivity and b) First derivative of resistivity.

The residual resistivity, ρ_0 is an indicator of the impurity scattering effects and it is defined as the resistivity value just before the transition, it is usually taken as the resistivity at 40 K for bulk MgB_2 samples. Resistivity begins to drop sharply at the onset critical temperature and it is measured as zero at offset critical temperature within the accuracy of the voltmeter. In order to convert voltage to resistivity the calculation is made as following:

$$\rho = \frac{R \cdot A}{L} = \left(\frac{V}{I}\right) \times \left(\frac{A}{L}\right) \tag{4.3}$$

where ρ is the resistivity, V is potential difference measured between voltage points, I is the current run through the sample, L is the distance between the voltage contacts and A is the cross sectional area of the sample, all in SI units.

The active cross-section area fraction (A_F) was calculated from the resistivity, ρ, from Rowell's model, using the following equations:

$$A_F = \frac{\rho_{ideal}}{\rho_{(300K)} - \rho_{(40K)}} \tag{4.5}$$

where ρ_{ideal} is the resistivity of a fully connected sample made from high purity sources, although, ρ_{ideal} of Rowell (2003) and Jiang et al. (2006) assumed 4.3 and 7.3 $\mu\Omega$cm, respectively. In addition, the residual resistivity ratio (RRR) is given by

$$RRR = \rho_{(300K)} / \rho_{(40K)}. \tag{4.6}$$

The critical temperature was determined as the temperature at which the derivative of the resistivity with respect to temperature was maximum, as can be seen Figure 4.11b. In the normal state (above T_c), all the samples showed metallic behaviour.

4.4.5 Infrared spectroscopy (IR)

Infrared spectroscopy is a very useful instrument that principally evaluate the individual frequencies of atoms between 10^{12} to 10^{13} Hz (West, 1999). The separate vibration modes of a sample can be aroused by the appropriate frequency in consequence of the atomic bonds in different environments absorb varying intensities and at varying sequences.

IR spectroscopy (Figure 4.12) is based on collecting absorption information and analyzing it in the form of a spectrum. Each frequency of absorbed IR radiation (peak) is correlated to bonds within the analyzed compound in the range of 4000 cm^{-1} to 400 cm^{-1}.

The method is suitable for detecting impurities characterizing borides and indicate presence of iron borides (Fofanov, 2006), as shown in Figure 4.13, where a broad band at around 1600 cm^{-1} was observed for Fe_2B crystalline.

With IR spectroscopy, a quite weak broad band from 1100 to 1300 cm^{-1} and a more sharp one at 700 cm^{-1} was detected for the iron boride samples (Joubert and Shirk, 1968; Avaeva and Kravchenko, 1972). Additionally, Figure 4.13 (blue line) show the IR spectroscopy result of sintered (900°C/1h) MgB_2 ex-situ powder sample.

Figure 4.12. Infrared spectroscopy (Perkin Elmer Spectrum Two).

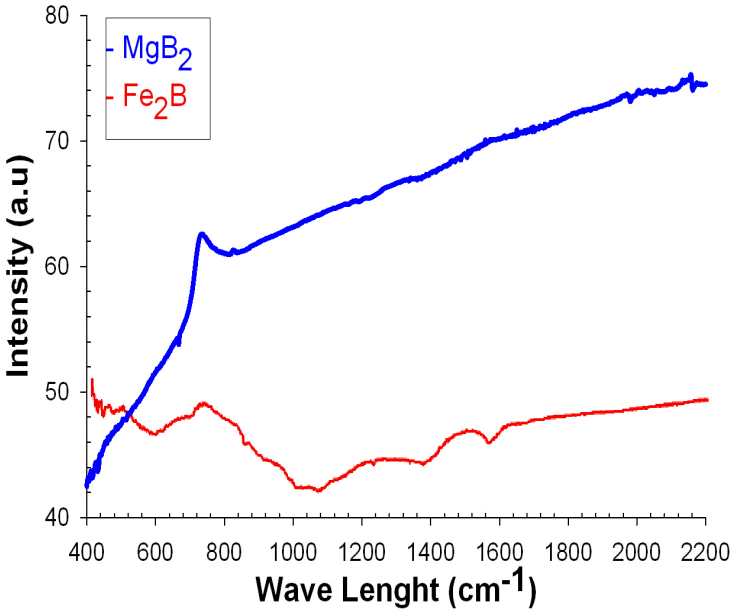

Figure 4.13. Infrared spectra of Fe_2B and MgB_2 powder samples.

5. RESULTS AND DISCUSSIONS

5.1 Introduction

The first part of this chapter is about studying the effect of sintering temperature on diffusion of Fe into MgB_2 bulk samples. For the first part of experiments, sintering temperature values were selected as 650°C, 700°C, 750°C, 800°C, 850°C, and 900°C while the duration of sintering was kept fixed as 1 hour. Low temperature measurements were used to examine superconducting properties and room temperature electrical measurements were performed to investigate Fe diffusion into MgB_2 body. Diffusion of Fe was also studied by calculating lattice parameters from XRD analysis. These XRD patterns were taken from progressively deeper layers on the Fe coated surface of the bulk MgB_2 pellets.

In second part, diffusion of Fe into the bulk of Fe coated MgB_2 pellets was studied for different sintering times at a fixed sintering temperature of 900°C. This annealing time values were chosen as 15 minutes, 30 minutes, 1 hour, 2 hours, 4 hours, and 8 hours. The experimental procedure used in this second part of the investigation was same as the first part. Time dependence of diffusion coefficient for Fe coated MgB_2 was also calculated in the same manner.

Finally, temperature dependence of diffusion coefficient for Fe coated MgB_2 bulk samples was separately calculated using the variations in lattice parameter c and room temperature resistivity values calculated from progressively deeper layer of coated samples.

5.1.1 Structural Analysis of MgB_2 Superconductor Pellets Before and After Fe Coating

The aim of this part is to investigate whether Fe goes into the structure of MgB_2 bulk superconductor sample with coating process or not by using XRD, IR, SEM and EDS analysis. Result of XRD of the following examples which are non-sintered MgB_2 ex-situ powder (black line), sintered MgB_2 pellet (red line), non-sintered Fe coated MgB_2 (blue line), and sintered Fe coated MgB_2 (green line) that can be seen in Figure 5.1.

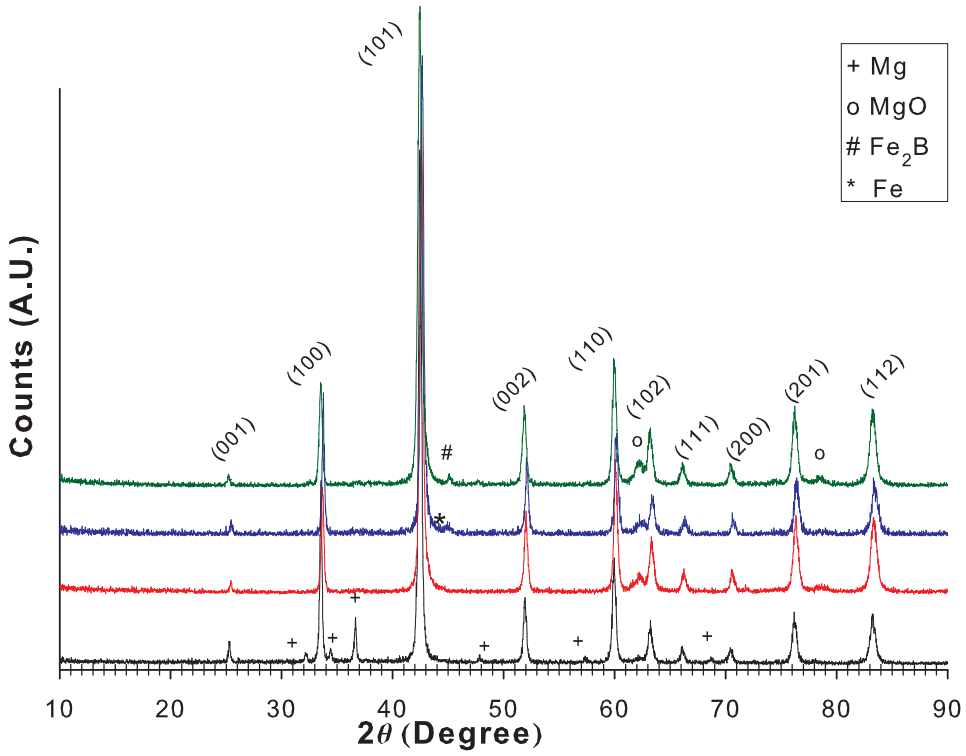

Figure 5.1. XRD patterns of MgB_2 samples before and after Fe coating. From bottom to top; as received ex-situ MgB_2 powder, sintered MgB_2 pellet, coated MgB_2 pellet and MgB_2 pellet sintered after Fe coating.

Although remarkable free Mg elements are detected in MgB_2 ex-situ powder, we have observed phases of MgO and MgB_2 after heat treatment. In addition, it is found that the intensity of the XRD peaks belonging to MgO phase increases after sintering process. XRD pattern of Fe coated MgB_2 sample taken before sintering has a peak of Fe, while after sintering, Fe coated MgB_2 sample has either Fe_2B or FeB peaks.

The intensity of the Fe_2B peak (FeB) located around $2\theta = 45°$ increases with sintering temperature to some extend, and free B present in the sample or B allocated from the structure of MgB_2 can form this compound by reacting with Fe, since any XRD peak cannot arise from a Mg-Fe compound which not chemically possible.

To support the result of XRD, samples were examined by using infrared spectroscopy the results of which can be seen in Figure 5.2 where MgB_2 ex-situ powder (black line), pellet (red line), non-sintered Fe coated MgB_2 (blue line) and sintered Fe coated MgB_2 (green line) represent curves of IR spectrum.

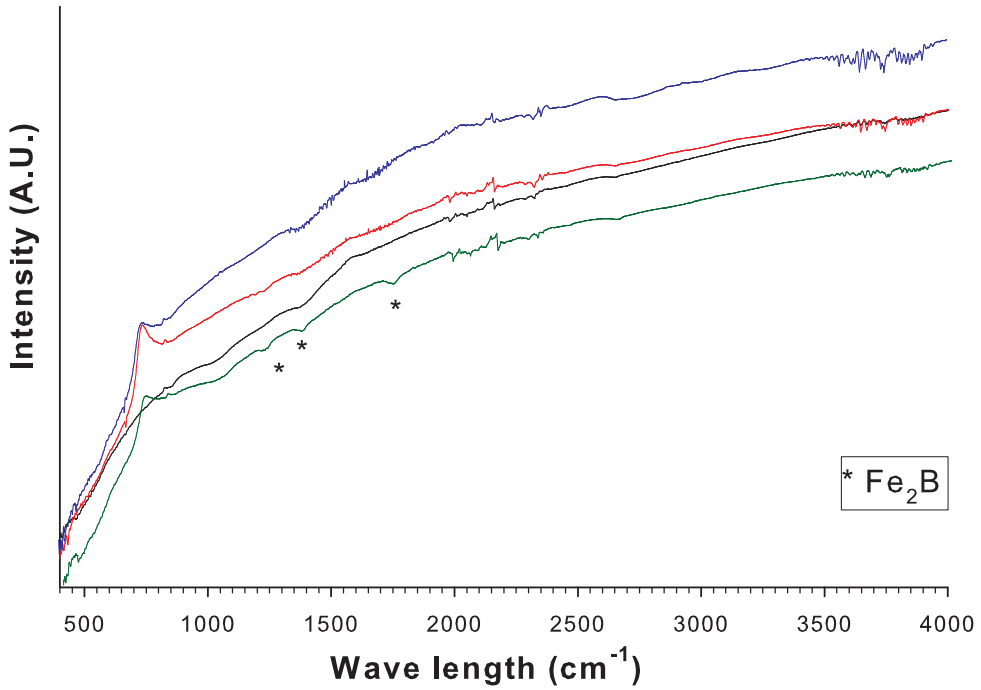

Figure 5.2. Infrared spectra of after and before Fe coated MgB_2 samples.

According to the result of IR, it is found that there is no change in spectrums of sintered/non-sintered MgB_2 sample and also non-sintered/Fe coated MgB_2 sample, while three quite weak broad band are determined at 1100, 1300, and 1700 cm^{-1} for the Fe coated/sintered MgB_2 pellet. In literature, it is known that the interaction between Fe and B substantiates between 1000 cm^{-1} and 1700 cm^{-1} for studies related with FeB and Fe_2B (Joubert and Shirk, 1968; Avaeva and Kravchenko, 1972) and the frequency 400 cm^{-1} would be preferable to make more sensitive measurements.

We have presented results of SEM and EDS measurements of the same samples in Figure 5.3 and Table 1.1, respectively. Sintered/non-sintered Fe coated MgB_2 are denser as presented in the photograph of SEM.

The significant feature in EDS results is that elevated amount of oxygen in Fe coated MgB_2 samples for all processing conditions ranges between 9.932 and 13.073. Also it is found that after heat treatment, weight percent of Fe increases while there exist a reduction in the percentage of Mg and B elements. The reason for this observation may be interaction of free B present in MgB_2 ex-situ powder with Fe or decomposition of MgB_2 producing B and Mg atoms which react with Fe and O atoms, respectively.

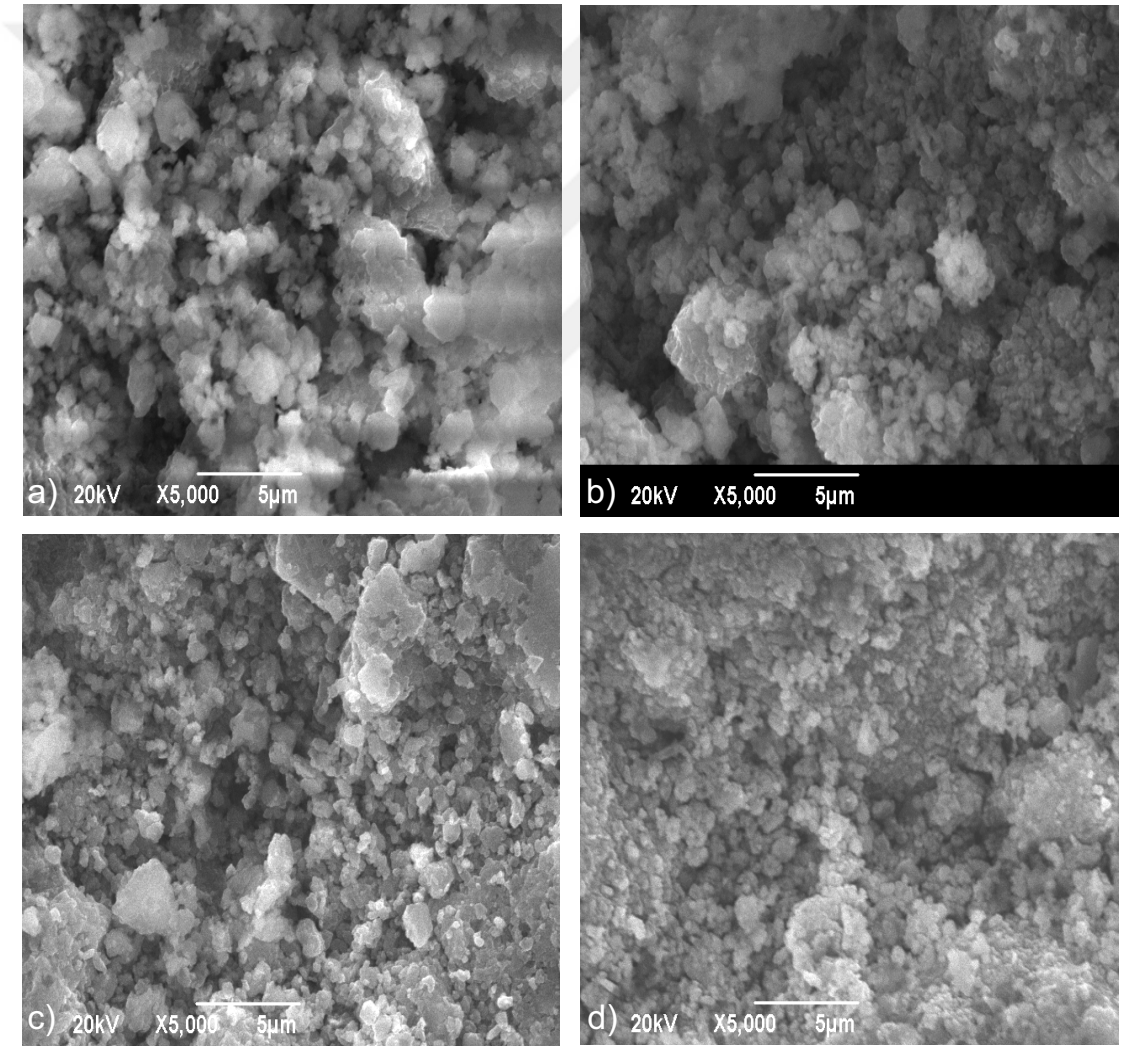

Figure 5.3. SEM images of a) MgB_2 powder, b) MgB_2 pellet, c) Fe coated MgB_2 (non-sintered) and d) Fe coated MgB_2 (sintered).

Table 5.1. Energy Dispersive X-ray Spectroscopy elemental analysis results.

Samples	**B** Elt. Conc wt.%	**O** Elt. Conc wt.%	**Mg** Elt. Conc wt.%	**Fe** Elt. Conc wt.%	Total Conc wt.%
MgB_2 Powder	72.552	4.778	22.671	—	100
MgB_2 Pellet	62.369	7.736	29.860	—	100
Fe coated/Non-sintered	54.156	9.932	29.615	4.979	100
Fe coated/Sintered	59.873	13.073	21.462	5.592	100

5.2 Effect of Sintering Temperature on Diffusion - Sintering at Different Temperatures

Pelletized bulk samples were divided into two groups. The first group was subjected to initial sintering at 800°C for 1 hour, codes of these samples start with S if this initial heat treatment is applied. The second group was used for further experiments as pelletized, codes of these samples start with N if this initial heat treatment is not applied. Also, second letter in the coding is either F for Fe coated samples or B for the bare samples which were not coated.

At this stage, each group was divided into two sub groups, either with or without Fe coating, in order to compare the effect of sintering temperature on Fe diffusion (see, Table 4.1 and Figure 4.5). In this section, we have given the details on the effect of Fe coating on the samples sintered at different temperatures.

5.2.1 Phase Analysis

Figure 5.4 presents the XRD patterns of Fe coated and bare MgB_2 bulk samples. These measurements were taken from the free outer surface of MgB_2 sintered pellets, bare or Fe coated. For studying the effect of sintering temperature, initially sintered samples of the first group (Set 1S) in this figure are indicated with the red line if Fe coated

(SF group) and with the black line if they are bare samples (SB group). On the other hand, for the effect of different sintering temperature, samples of second group (Set 1N) which are not sintered initially, Fe coated MgB_2 pellets are indicated as green line (NF group) and bare MgB_2 pellets are indicated as blue line (NB group).

Phase purity, lattice parameters and grain size were determined using these XRD results. They show the Bragg reflections of the hexagonal MgB_2 structure, plus some additional peaks which represent Fe_2B, MgO and Mg phases. Moreover, the peaks near 44°, 62° and 78° belonging to MgO are seen in these samples. XRD peak belonging Fe_2B phase in MgB_2 pellet only appears near 45°, and intensities of XRD peaks belonging to Fe_2B phase are tabulated in Table 5.2. Due to the reaction between B and Fe atoms (Li et al., 2011), presence of Mg and Fe_2B have been observed in our Fe coated samples. Existence of Fe_2B reveals that either un-reacted B reacts with Fe or B atoms in the MgB_2 grains break away and form Fe_2B phase. These discussions are further supported by appearance of Mg with higher sintering temperatures, especially at 900°C.

Besides the impurity phase of Fe_2B (Novosel et al., 2010-2012), there may be other forms of Fe in the system, as FeB (Pachla et al., 2004). The appearance of Fe_2B and increased amount of MgO phase indicate that some extent a reaction between Mg and O occurred during annealing process.

Table 5.2 shows the lattice parameters *a* and *c*, grain size and FWHM value of Fe coated and bare MgB_2 bulk samples for different sintering temperatures. The refinement results reveal that changes in lattice parameter *a* is not significant. The value of the lattice parameter *a* of coated and bare samples sintered at all temperatures fluctuate around 3.08 Å, decreasing with increasing sintering temperature up to 800°C then becoming largest at 850°C, as seen from the Figure 5.5a.

On the other hand, the value of lattice parameter *c* varies between 3.516 Å and 3.538 Å for these samples and Fe coated samples have higher *c* parameters for all sintering temperatures. The behaviour of lattice parameter *c* for Fe coated samples follows par-

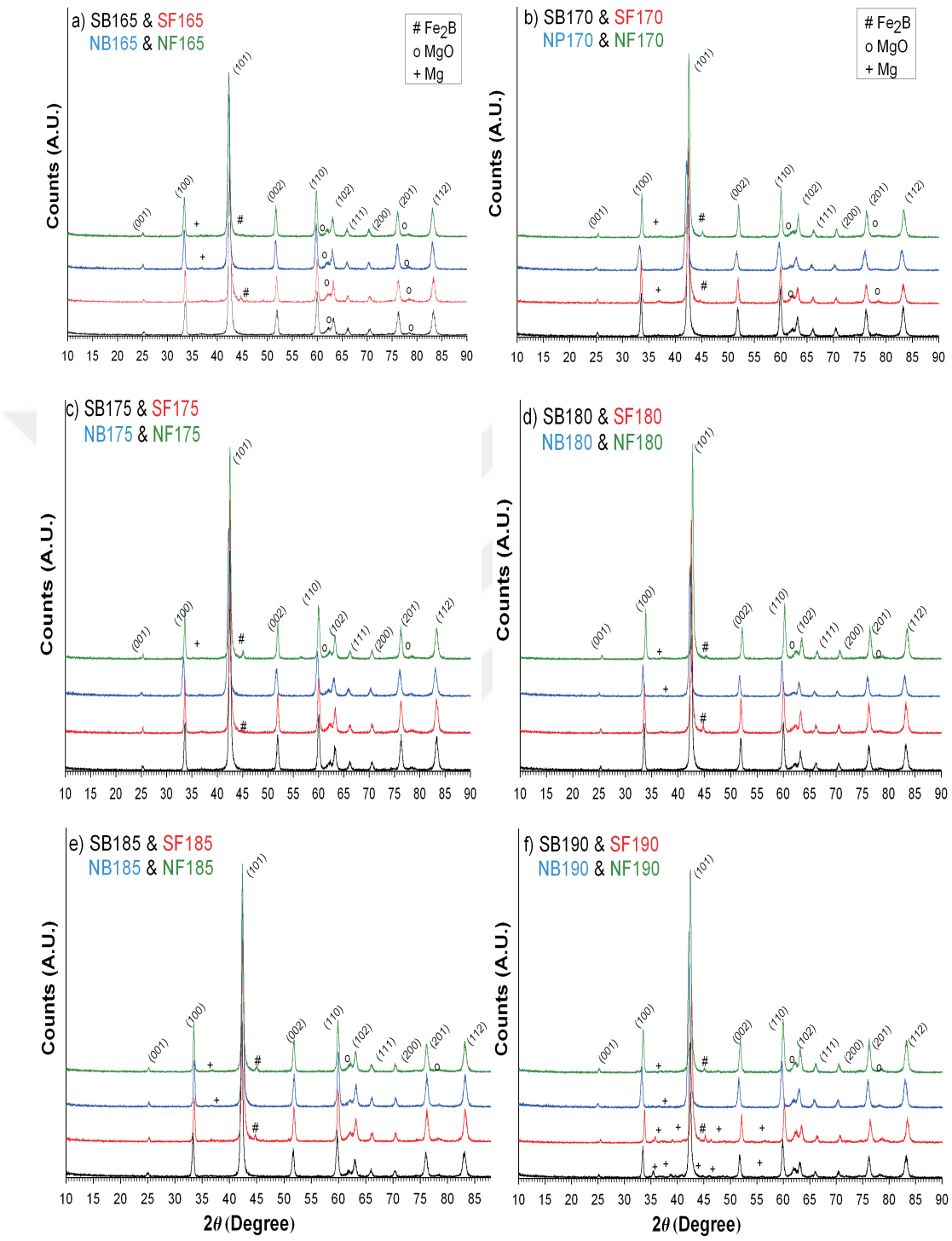

Figure 5.4. XRD patterns of bare and Fe coated MgB_2 samples for different sintering temperatures.

allel curves in the cases of initially sintered and not initially sintered samples, similar parallel behaviour is also seen in Figure 5.5b bare samples. Lattice parameter *c* slightly decreases with increasing sintering temperature up to 750°C for all samples, then for sintering temperature of 800°C, it increases for initially sintered samples and decreases for other samples. With increase of sintering temperature to 850°C, *c* parameter becomes maximum for all sets of samples then sharply declines with further increase of sintering temperature to 900°C. Effect of Fe diffusion on *c* parameter has similar sintering temperature dependence for all samples with or without initial sintering. Analysis of the full width at half maximum (FWHM) offers considerable information on the crystallite size and lattice strain in the sample. Among the XRD peaks, (101) diffraction peak was chosen for FWHM analysis in Table 5.2. The grain size and strain can be estimated from the FWHM value. This value is related to the crystallinity and lattice distortion.

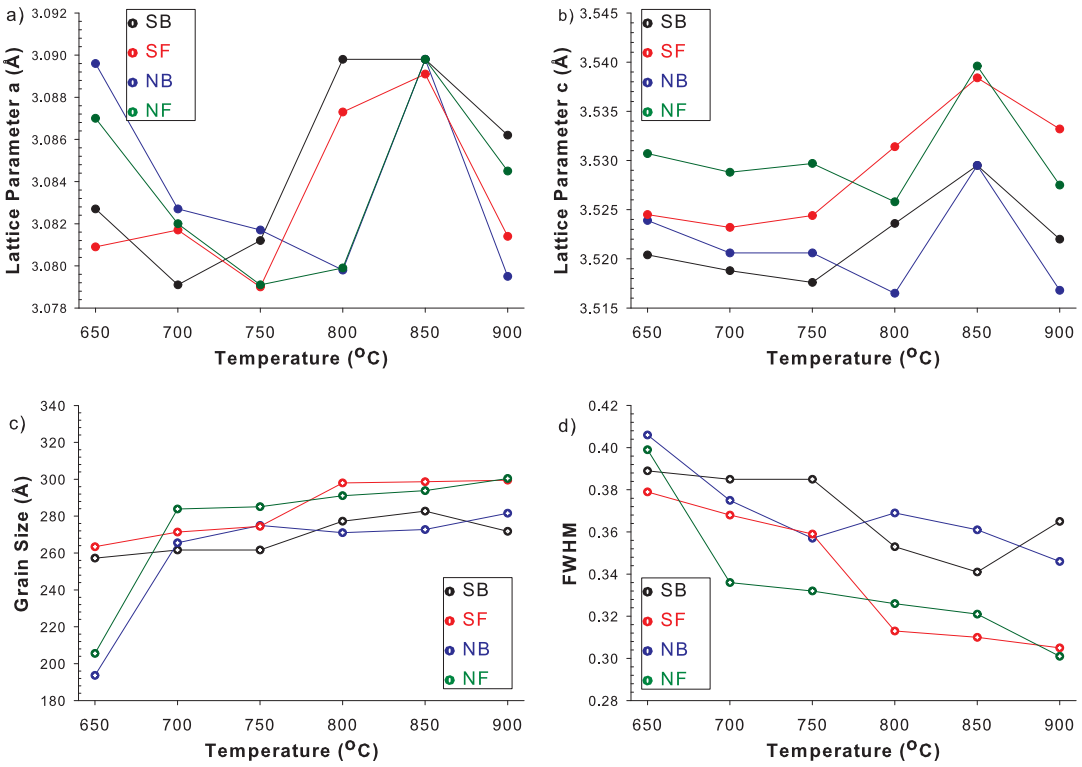

Figure 5.5. a) Lattice parameter *a*, b) Lattice parameter *c*, c) Grain size and d) FWHM value behaviours for Fe coated and bare MgB_2 samples sintered for different temperatures.

Table 5.2. Lattice parameter a and c, grain size, FWHM, and Fe_2B peak intensity values of Set 1S and Set 1N MgB_2 samples for different sintering temperatures.

MgB_2 Samples for Set 1S	Lattice Parameter a (Å)	Lattice Parameter c (Å)	Grain Size (Å)	FWHM Value (°)	Fe_2B peak Intensity (a.u)	**MgB_2 Samples for Set 1N**	Lattice Parameter a (Å)	Lattice Parameter c (Å)	Grain Size (Å)	FWHM Value (°)	Fe_2B peak intensity (a.u)
SB165	3.083	3.520	257.24	0.382	—	**NB165**	3.089	3.524	193.65	0.406	—
SF165	3.081	3.525	263.40	0.379	145	**NF165**	3.087	3.531	205.57	0.397	108
SB170	3.079	3.519	261.66	0.380	—	**NB170**	3.082	3.521	265.55	0.375	—
SF170	3.082	3.523	271.36	0.368	164	**NF170**	3.082	3.529	283.86	0.336	225
SB175	3.081	3.518	261.66	0.380	—	**NB175**	3.081	3.521	274.95	0.357	—
SF175	3.079	3.524	274.46	0.359	165	**NF175**	3.080	3.530	285.12	0.332	275
SB180	3.089	3.523	277.25	0.353	—	**NB180**	3.080	3.516	271.02	0.369	—
SF180	3.087	3.531	298.02	0.313	258	**NF180**	3.070	3.526	291.10	0.326	137
SB185	3.089	3.529	282.72	0.341	—	**NB185**	3.089	3.529	272.72	0.361	—
SF185	3.089	3.538	298.65	0.310	262	**NF185**	3.089	3.540	293.80	0.321	204
SB190	3.086	3.522	271.78	0.365	—	**NB190**	3.079	3.517	281.59	0.346	—
SF190	3.082	3.533	299.49	0.305	273	**NF190**	3.084	3.528	300.43	0.301	175

Lower value of FWHM for the NF190 samples (0.301°) gives evidence of strain effects that have occurred. The FWHM values decrease with increasing the annealing temperature from 650°C to 900°C for 1 hour, as can be seen in Figure 5.5d. FWHM values for the bare samples also decrease with increasing sintering temperature but not as much as Fe coated samples. This behaviour of the MgB_2 samples can be explained by the improvement of crystallinity with increasing the annealing temperature, resulting in increasing grain size (Kim et al., 2006) and in the case of Fe coating an additional contribution from lattice strain.

Average grain size of a crystal in the broadening region is defined by Equation 4.1. The grain size values of samples sintered at different temperatures were calculated from XRD patterns and these values were given in Table 5.2. It is found that the NF190 and SF190 samples have largest grain size ($\sim$300 Å), and the differences between Fe coated and bare samples are apparent. This indicated the suitability of lower temperature annealing for obtaining smaller grains which is beneficial for magneto-transport property of MgB_2 superconductors. Grain size values of samples NB165 and NF165 are significantly smaller than that of other samples due to low sintering temperature of 650°C and, additionally, grain size of NF165 is somehow larger than that of NB165. All of the samples of Set 1S including the ones sintered at 650°C have grain size values above 257 Å since the all the samples of this set were initially pre-sintered at 800°C for 1 hour. Furthermore, grain size of Fe-diffused MgB_2 material compared to ones sample is larger indicating Fe coating/diffusion causes grain size to increase. The grain sizes of the both sets are found to become larger with increasing sintering temperature as seen in Figure 5.5c.

For instance, iron is by far the most reactive element in its group, the ionic radius of Fe^{+2} is 0.076 nm, while that of Fe^{+3} is 0.065 nm. The increase of *c*-axis length with Fe coating may be due to the smaller size of the Fe^{+3} ion or Fe^{+2} ion. However, it is very difficult to understand the increase in the *c* parameter. Table 5.3 shows the chemical properties of iron atoms.

Iron atoms or iron ions within MgB_2 lattice structure may both be disturbing (distorting), because of its ionic radius is smaller than the atomic radius.

Table 5.3. Basic properties value of Fe element.

Properties	**Value**
Atomic number	26
Period/Group	4/8
Electron configuration	$1s^2\ 2s^2\ 2p^6\ 3s^2\ 3p^6\ 4s^2\ 3d^6$
Atomic weight (amu)	55.845
Theoretical Density(g/cm^3)	7.874
Crystal structure	fcc
Atomic Radius (nm)	0.126
Atomic Volume (cm^3/mol)	7.1
Melting Point (K)	1811
Electrical Resistivity at 20°C (Ωm)	9.7×10^{-8}
Magnetic ordering	ferromagnetic

On the other hand, the intra-layer interatomic distances between atoms of $B-B$ and $Mg-Mg$ are 0.1780 nm and 0.3084 nm, respectively. Although, the inter-layer interatomic distances are $B-B$ 0.17 nm, $Mg-B$ 0.25 nm and $Mg-Mg$ 0.3524 nm. When interatomic distances and ionic radius of Fe ions are considered, it is quite possible to speculate that Fe atoms may occupy interstitial positions.

5.2.2 Microstructural and Chemical Analysis

The micrograph in Figure 5.6 shows the fractured cross-section of SF180. As seen in this figure, Fe layer is apparent on coated surface as well as Fe_2B phase beneath the surface. Also, Fe coating thickness of about 50 μm is seen in this micrograph. The surface morphology of the Fe coated and bare samples of MgB_2 sintered at different temperatures for 1 h were observed by SEM are displayed in Figure 5.7 and Figure 5.8.

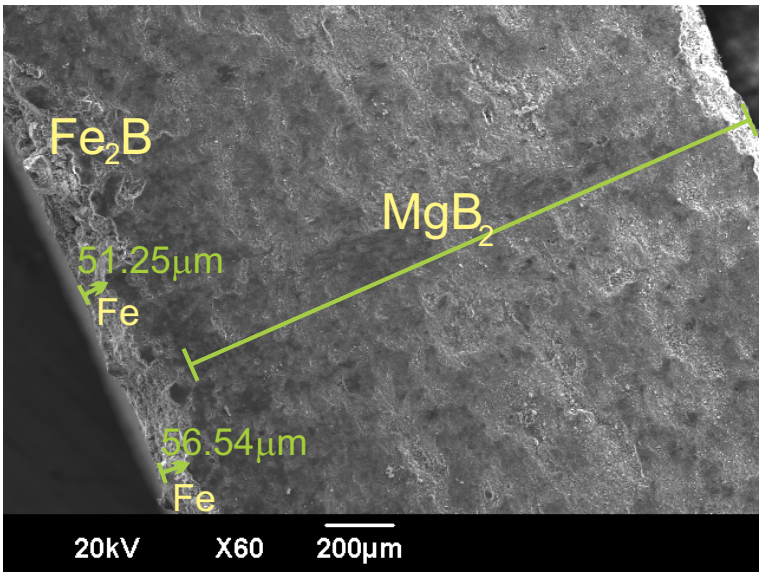

Figure 5.6. SEM images of $Fe/Fe_2B/MgB_2$ cross sectional area for SF180 sample.

Among the samples prepared, the broadest grain size ($\sim$ 300Å) was indeed observed for the sample sintered at 900°C for 1 hour. SEM show micrographs that surface morphology, grain connectivity and grain size of the Fe coated samples improved with increasing sintering temperature. The improvement of crystallinity is associated with better grain connectivity of the MgB_2 grains. The microstructure of Fe coated samples are remarkably different from bare samples, for example, NF190 and SF190 samples have good grain connectivity, better surface and low porosity and they are denser than other samples.

The SEM images given in Figure 5.7b, Figure 5.7d and Figure 5.7e display the Fe-diffused surface of the samples sintered at 650-750°C for 1 hour, while bare samples are displayed in the Figure 5.7a, Figure 5.7c, and Figure 5.7e. Also, Figure 5.8a to Figure 5.8f represent surface micrographs of the samples SB180, SF180, SB185, SF185, SB190, and SF190.

Since the samples of Set 1S and Set 1N group have similar micro-structures, only micrographs related to the samples of Set 1S group are given with initial sintering. The outer surfaces of coated samples are denser than bare samples and they have more uniform surface appearance when the annealing temperature is between 800 and 900°C.

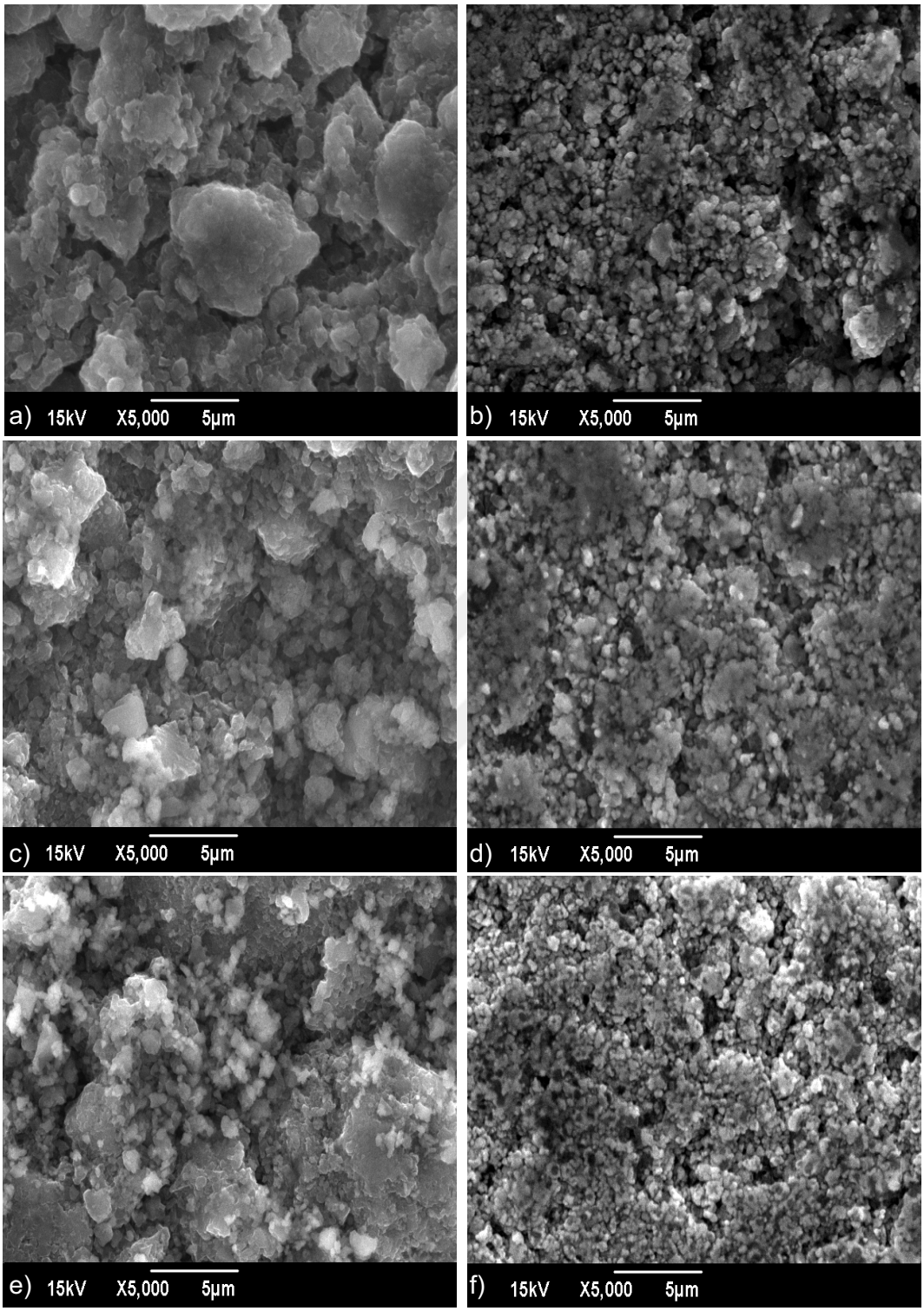

Figure 5.7. SEM images taken from upper surface for a) SB165, b) SF165, c) SB170, d) SF170, e) SB175 and f) SF175 sample.

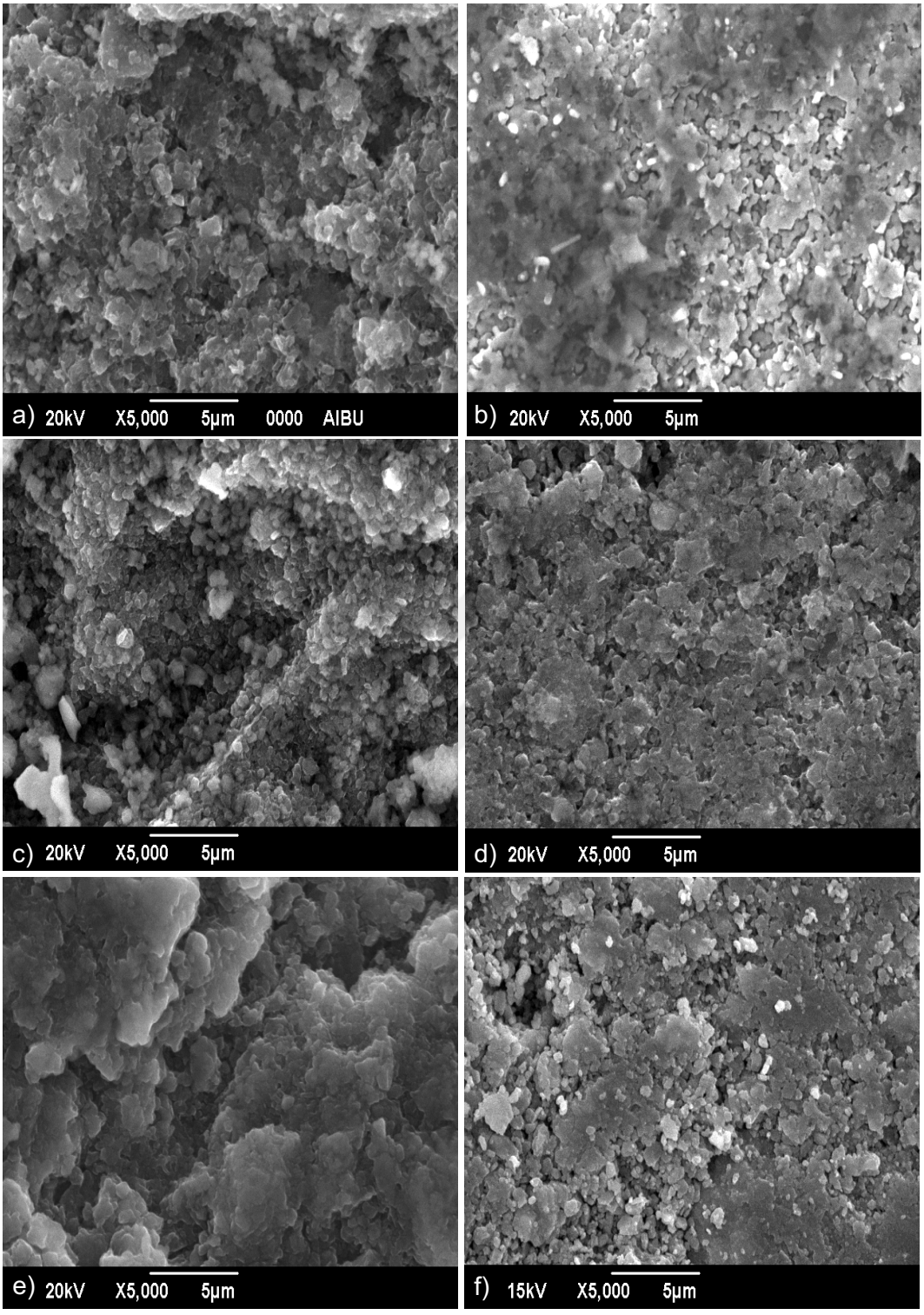

Figure 5.8. SEM images taken from upper surface for a) SB180, b) SF180, c) SB185, d) SF185, e) SB190 and f) SF190 sample.

These findings may be due to prevention of Mg loss from the outer surface during sintering because of Fe layer. Also, the grain structure and morphology seem to be different in these Fe coated samples where the grains have merged into big clusters. Therefore, based on the SEM observations, it seems that the Fe coated samples are denser and have better connected grains than the bare ones. As the sintering temperature increases, the grain size increases (Figure 5.5c) and surface of the sample becomes smoother.

Figure 5.9 shows the EDS results of Fe coated and bare MgB_2 bulk superconductor of both groups. Other samples show similar behaviour as samples annealed at 800°C for 1 hour in EDS analysis. EDS analysis were performed in order to determine the chemical content of these samples at upper surface where Fe coating was or was not applied.

The EDS results showed that the oxygen content is increased in Fe coated MgB_2 bulk samples. Initially sintered bare samples which were annealed at 800°C for 1 hour were found to contain 6.3 wt% oxygen, and in the case of all the other parameters for Fe coated sample are identical, oxygen and Fe contents were respectively 15.1 wt% and 10.3 wt%. For Set 1N group (without initial sintering), bare sample annealed at 800°C for 1 hour was found to have oxygen 6.3 wt%, and Fe coated sample (all other parameters are same) had 9.0 wt% oxygen content and 7.7 wt% Fe content at the upper surface. These EDS results are compatible with XRD patterns in which Fe_2B, Mg and MgO peaks were observed as seen in Figure 5.4.

EDS analysis for both groups shows that coating process caused the amount of oxygen to increase on coated side of the samples after final sintering. In the case of Fe coated samples, the sample without initial sintering has lower Fe content at the Fe coated surface in comparison to initially sintered sample. This fact shows that Fe atoms migrate into MgB_2 less easily when the grains are bound by sintering.

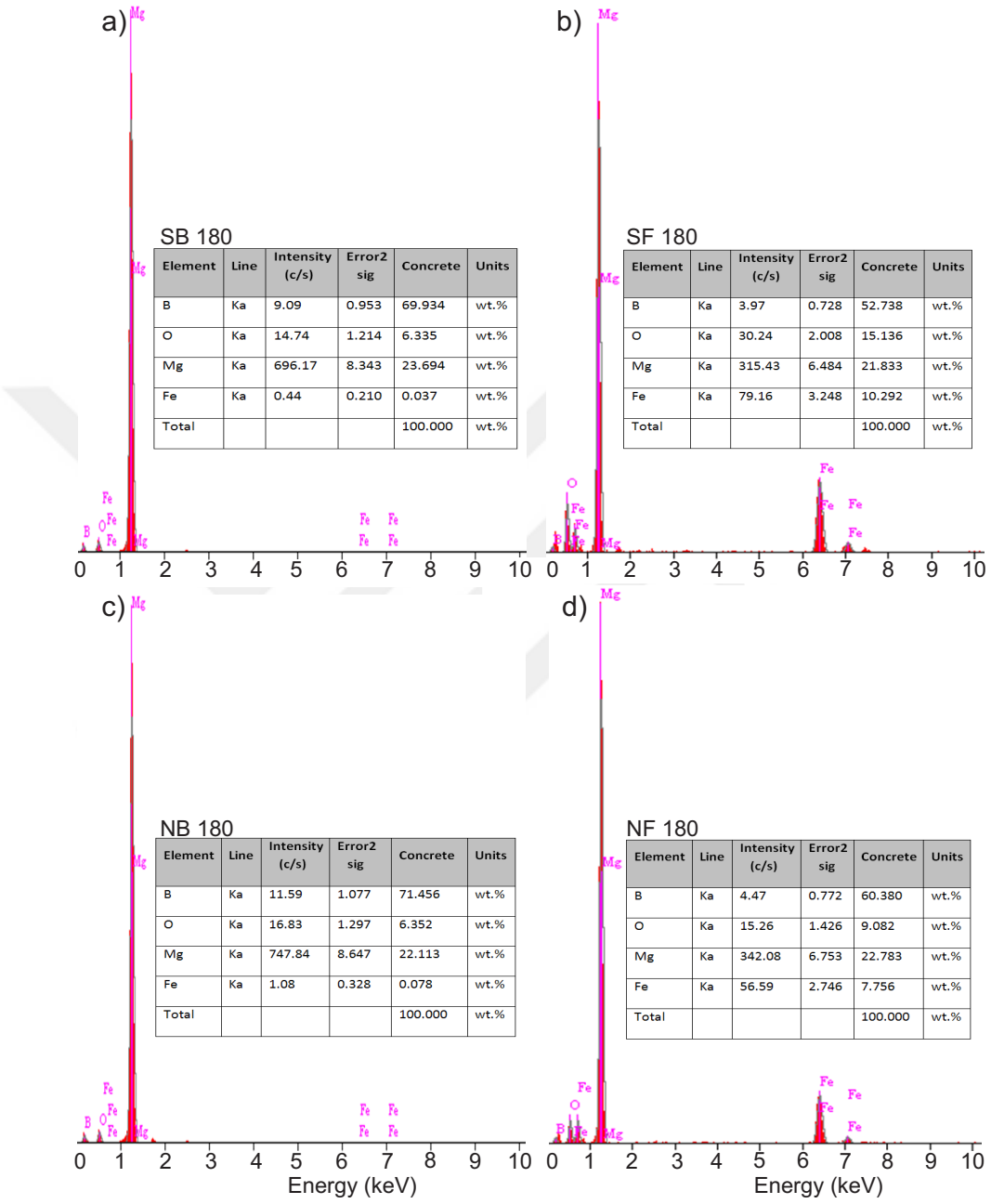

Figure 5.9. Energy Dispersive X-ray Spectroscopy analysis of bare and Fe coated MgB_2 bulk samples; a) SB180, b) SF180, c) NB180 and d) NF180.

5.2.3 Electrical Resistivity Measurements

The measured resistance curves need to be converted to resistivity by taking sample dimensions and measurement configuration into account in order to compare the data obtained from different samples. The length, width and thickness of the samples were measured by a micrometer easily due to rectangular sample geometry. Temperature dependence of samples resistance was measured to determine transition temperature of the Fe coated and bare MgB_2 samples. In order to investigate the influence of Fe diffusion on superconducting properties of MgB_2 superconductor materials, electrical resistivity measurements were performed in a temperature range of $10-45$ K. Figure 5.10 shows the temperature variation of the resistivity of bare and coated samples for different sintering temperatures, the inset in this figure magnifies the transition region.

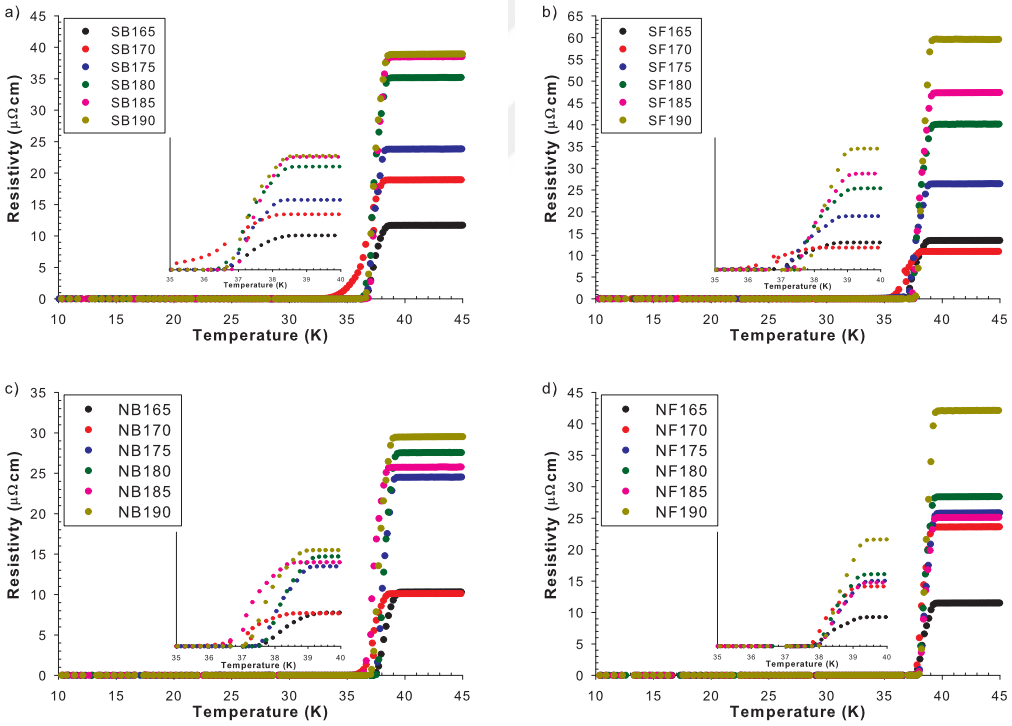

Figure 5.10. Resistance versus temperature curves for a) initial sintering set of bare sample (SB), b) initial sintering set of Fe coated sample (SF), c) not initial sintering set of bare sample (NB) and d) not initial sintering set of Fe coated (NF) at different annealing temperature.

R-T curves, in Figure 5.10 are re-grouped with respect to their processing routes, given in Figure 5.11. Residual resistivity before transition becomes progressively higher as the sintering temperature increases. Bare samples without initial sintering (NB) have the lowest residual resistivity for all sintering temperatures and as general tendency, magnitudes of residual resistivity become larger in the order of NB, NF, SB and SF. This increment in resistivity is in contrast with the literature results, due to increased inter-band and intra-band scattering in the σ and π bands (Xi, 2008; Kim et al., 2012). Normal state resistivity just above the transition is higher for Fe coated samples, considering that the resistivity of iron lower than MgB_2 at those temperatures, higher resistivity in Fe coated samples is seemingly due to chemical interactions between Fe atoms and MgB_2 bulk superconductor. T_c^{offset}, T_c and ρ_{300K} of both sets are given in Table 5.4 and Figure 5.12.

Table 5.4. Results of transport measurements of T_c^{offset}, T_c and ρ_{300K} for different sintering temperatures

Set 1S	T_c^{offset}	T_c	ρ_{300K}	**Set 1N**	T_c^{offset}	T_c	ρ_{300K}
Samples	(K)	(K)	($\mu\Omega$cm)	**Samples**	(K)	(K)	($\mu\Omega$cm)
SB165	36.12	37.03	40.5	**NB165**	37.02	37.93	35.7
SF165	36.44	37.17	43.9	**NF165**	37.46	38.06	37.4
SB170	35.30	36.77	45.7	**NB170**	36.17	37.17	37.0
SF170	35.58	37.29	51.4	**NF170**	37.61	38.19	41.4
SB175	36.26	37.09	48.3	**NB175**	37.09	37.82	37.7
SF175	36.63	37.31	55.7	**NF175**	37.62	38.22	40.5
SB180	35.94	37.02	57.8	**NB180**	37.30	37.94	39.0
SF180	37.18	37.56	68.6	**NF180**	37.50	38.13	47.2
SB185	36.59	37.23	58.2	**NB185**	35.96	37.02	40.7
SF185	37.14	37.61	71.8	**NF185**	37.55	38.17	43.0
SB190	36.18	37.04	59.8	**NB190**	36.63	37.49	41.2
SF190	37.28	37.90	82.0	**NF190**	37.78	38.20	57.6

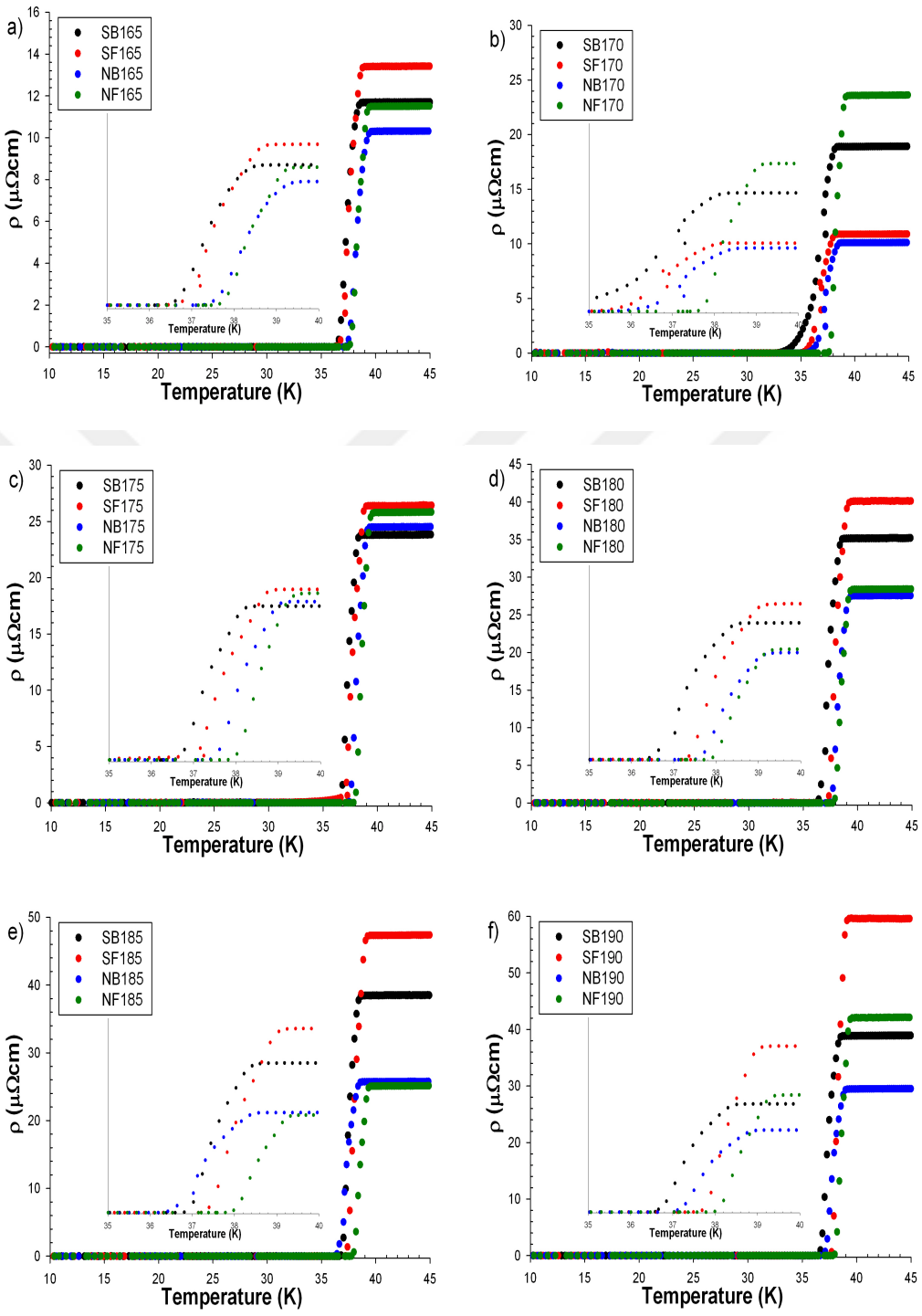

Figure 5.11. Resistance versus temperature curves for different sintering temperatures.

We observed a slight increase in T_c due to Fe coating process. This is an important result since Fe doping causes T_c reduction in MgB_2 (Zhou and Dou, 2010). Some parameters, such as sintering temperature, sintering time, coated material and chemical interaction at the interface may also affect T_c and T_c^{offset} values. These values of the Fe coated samples are higher than those of the bare samples, when all other processing parameters are same.

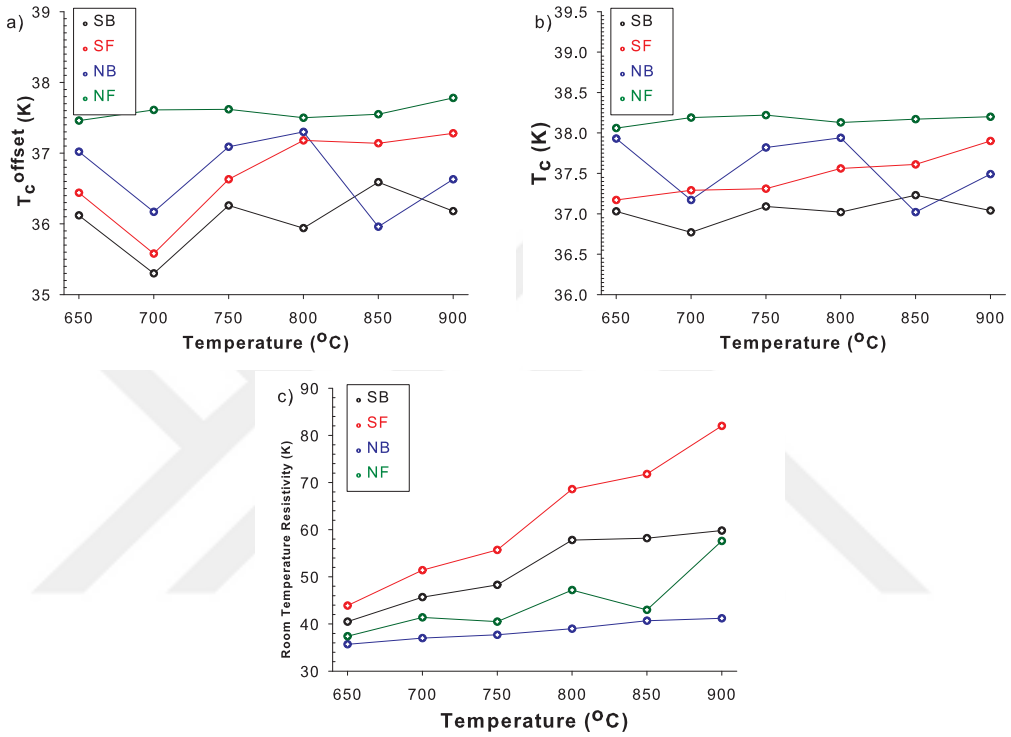

Figure 5.12. a) T_c^{offset}, b) T_c and c) ρ_{300K} behaviours for Fe coated and bare MgB_2 samples sintered for different temperatures.

The resistivity of the Fe coated and bare MgB_2 samples at room temperature was found to have values from 35.7 $\mu\Omega$cm to 82.0 $\mu\Omega$cm, which is reasonable when compared to the values between 10 and 100 $\mu\Omega$cm given in literature for pollycrystalline MgB_2 bulk samples (Putti et al., 2003; Jiang et al., 2006). The measured T_c values were 37 K and 38 K. All the samples show metallic behaviour in the normal state above transition. The ρ_{300K} values of all samples were calculated from I$-$V curves measured at room temperature. For Fe coated samples (SF and NF), values of ρ_{300K} are higher than bare ones (SB and NB) irrespective of sintering temperature.

Despite this fact, critical offset temperatures of Fe coated samples are higher for every sintering temperature. This effects is more pronounced in samples initially sintered before coating and/or sintered at higher temperatures. Diffusion of iron seems to be more critical for resistive superconducting transition temperatures in initially sintered samples. As the annealing temperature increases, room temperature resistivity values of initially sintered bare and Fe coated samples (SB and SF) increased from 40.5 $\mu\Omega$cm to 82.0 $\mu\Omega$cm. The room temperature resistivity of NB group samples showed a minor dependence on sintering temperature. Room temperature resistivity of initially sintered and Fe coated (SF) samples have the strongest sintering temperature dependence. Since the samples of NF (no initial sintering, Fe coated) and SB (initial sintering, bare) exhibited similar behaviors in this respect indicating that both Fe coating and initial sintering have an enhancing effect on room temperature resistivity of the samples. The room temperature resistivity values of NB and NF samples increase from 35.7 $\mu\Omega$cm and 37.4 $\mu\Omega$cm to 41.2 $\mu\Omega$cm and 57.6 $\mu\Omega$cm, respectively. Apparently Fe diffused samples exhibit higher rates of increase.

Fe coated samples have higher room temperature resistivity compared to bare samples. This increase may be attributed to the modified grain boundary properties. So, this behaviour of the MgB_2 samples may be explained by the improvement of crystallinity with increasing the annealing temperature, resulting in increasing grain size (Kim et al., 2006).

Additionally, this improvement might be due to coupling between the Fe coated superconducting grains (Jiang et al., 2008) and/or Fe-stimulated grain growth through partial melting of MgB_2. Larger grains and smaller grain orientation lead to an increased critical temperature.

Table 5.5 summarizes the residual resistivity ratio (RRR), difference between resistivity at 40 K and 300 K ($\Delta\rho$), and active area fraction (A_F) for the Fe coated and bare MgB_2 samples. In addition, as explained by Rowell, the connectivity also plays a major role in determining the resistivity of MgB_2.

Table 5.5. Residual resistivity ratio, difference between resistivity at 300 K and 40 K, and active area fraction of the Fe coated and bare MgB_2 samples.

Set 1S	RRR	$\Delta\rho$	A_F	**Set 1N**	RRR	$\Delta\rho$	A_F
Samples		($\mu\Omega$cm)		**Samples**		($\mu\Omega$cm)	
SB165	3.462	28.8	0.149	**NB165**	3.466	25.4	0.169
SB170	4.193	34.8	0.124	**NB170**	3.663	26.9	0.160
SB175	2.029	24.5	0.176	**NB175**	1.539	13.2	0.326
SB180	1.637	22.5	0.191	**NB180**	1.423	11.6	0.371
SB185	1.516	19.8	0.217	**NB185**	1.578	14.9	0.289
SB190	1.537	20.9	0.206	**NB190**	1.397	11.0	0.368
SF165	3.276	30.5	0.141	**NF165**	3.252	25.9	0.166
SF170	2.245	28.5	0.151	**NF170**	1.754	17.8	0.242
SF175	2.110	29.3	0.147	**NF175**	1.359	10.7	0.402
SF180	1.711	28.5	0.151	**NF180**	1.645	18.5	0.232
SF185	1.518	24.5	0.176	**NF185**	1.713	17.9	0.240
SF190	1.376	22.4	0.192	**NF190**	1.368	15.5	0.277

In order to explain the connectivity between grains, A_F values are estimated for the samples annealed at different temperatures. The estimated A_F values vary between 0.124 to 0.402, the highest value was obtained for the NF175 sample indicates the better connection in MgB_2 grains (Yeoh et al., 2007), while SB170 had lowest value as shown in Figure 5.13a. As a general behaviour, initial sintering reduces A_F values in both Fe coated and bare samples regardless of sintering temperature. Also, NF175 sample had lowest $\Delta\rho$ and RRR values and highest T_c value of 38.22 K as shown in Figure 5.13b. $\Delta\rho$ values of Fe coated samples are smaller compared to bare samples and in all groups of samples, it is reduced by increasing sintering temperature. RRR values of samples which were sintered at temperatures of 650°C, 800°C, 850°C and 900°C were close to each other. There is a large variation in the RRR values of the samples belonging to different groups when sintered at 700°C and 750°C, as seen in Figure 5.13b.

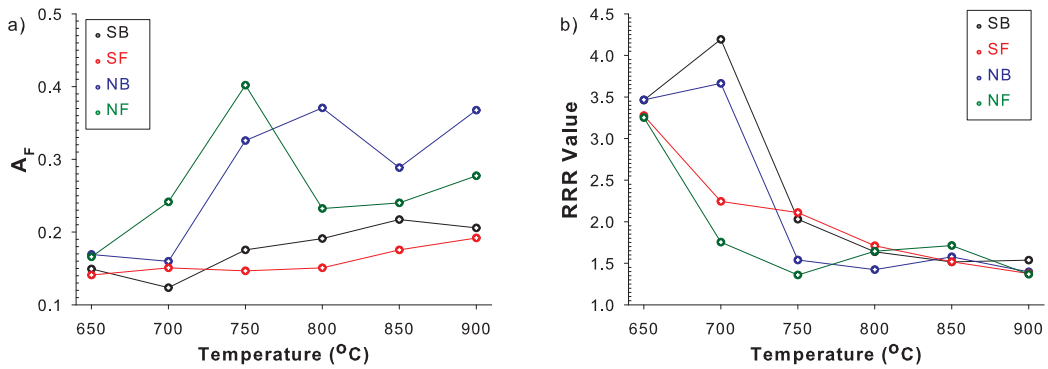

Figure 5.13. a) Active area fraction and b) Residual resistivity ratio value behaviours for Fe coated and bare MgB_2 samples sintered for different temperatures.

The difference is a significant for sintering temperature of 700°C and less significant for 750°C. We do not have any explanation for these differences. Increased electrical conductivity may have resulted in a higher A_F for NF175 samples (see, Figure 5.13a).

The RRR, the ratio of the resistivity at 300 K to that at 40 K, reflects the degree of electron scattering. When the electron scattering has a high value, it causes a reduction in the RRR. The RRR values obtained for the Fe coated samples were smaller than that of the bare sample (Figure 5.13b). Therefore, the variations in the resistivity of the bare and coated samples depend on the grain connectivity factor.

5.3 Effect of Sintering Time on Fe Diffusion - Sintering for Different Times

Pelletized bulk samples were divided into two groups, similar to different sintering temperature groups. The first group was initial sintered at 800°C for 1 hour, codes of the samples start with letter S if this initial heat treatment is applied, if not, they start with letter N. At this stage each group was divided into two sub groups in order to compare the effects sintering time on Fe diffusion (see Table 4.2 and Figure 4.6). Second letter in the coding is either letter F for Fe coated samples or letter B for the bare samples which were not coated.

In this section, we have given the details of samples sintered for different time durations of 15 minutes, 30 minutes, 1 hr, 2 hours, 4 hours and 8 hours at 900°C.

In order to understand the effect of sintering time on Fe diffusion, we performed XRD, SEM-EDS analysis, and low temperature and room temperature electrical measurements on polycrystalline MgB_2 samples before and after Fe diffusion. Hereafter, the studied samples will be referred as the samples without initial sintering (Set 2N) and the samples with initial sintering (Set 2S), respectively.

The effects of different sintering durations on Fe diffusion into MgB_2 are assessed by a comparing the experimental results of the samples belonging to different groups with various processing conditions.

5.3.1 Phase Analysis

Room temperature XRD patterns taken from the upper wide the surface of the Fe coated and bare samples annealed for different time durations are shown in Figure 5.14. Phase purity, the lattice parameters (a and c) and grain sizes were determined from these XRD patterns. Additionally, these XRD patterns show all the Bragg reflections of the hexagonal MgB_2 structure, plus some additional peaks which represent Fe_2B, MgO and Mg phases.

Fe particles have been reported to react with B to form FeB and Fe_2B and to be homogeneously distributed within the matrix of bulk samples (Dou et al., 2005). In our experiments, intensity of Mg peaks increases with rising sintering time for both groups. The main peak belonging the Fe_2B phase in MgB_2 pellets appear near 45° (2θ), and intensities of these peaks are tabulated in Table 5.6.

Presence of Fe_2B and Mg were observed in Fe coated samples due to the reaction between B and Fe atoms. Intensity of Fe_2B peaks has a tendency to decrease as the sintering duration is extended with an accompanying increase in intensity of Mg peaks.

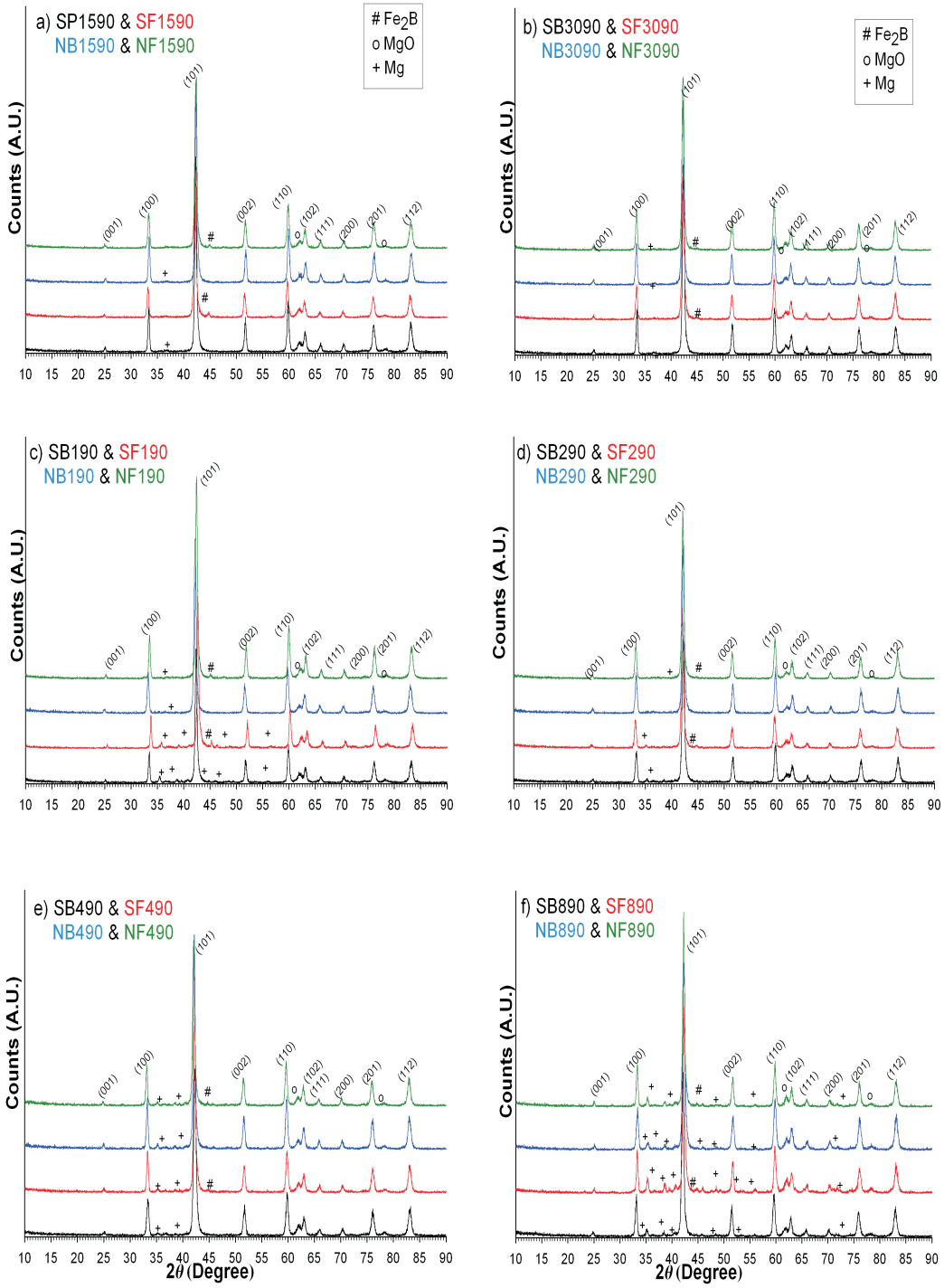

Figure 5.14. XRD patterns of bare and Fe coated MgB_2 samples for different sintering times.

Table 5.6. Lattice parameter *a*-*c*, grain size, FWHM, and Fe_2B peak intensity values of Set 2S and Set 2N MgB_2 samples for different sintering times.

MgB_2 Samples for Set 2S	Lattice Parameter *a* (Å)	Lattice Parameter *c* (Å)	Grain Size (Å)	FWHM Value (°)	Fe_2B peak Intensity (a.u)	**MgB_2 Samples for Set 2N**	Lattice Parameter *a* (Å)	Lattice Parameter *c* (Å)	Grain Size (Å)	FWHM Value (°)	Fe_2B peak intensity (a.u)
SB1590	3.088	3.523	199.51	0.402	—	**NB1590**	3.089	3.520	195.64	0.404	—
SF1590	3.089	3.531	218.56	0.387	198	**NF1590**	3.089	3.529	219.10	0.386	139
SB3090	3.089	3.526	211.21	0.391	—	**NB3090**	3.088	3.521	203.65	0.399	—
SF3090	3.087	3.536	220.20	0.385	128	**NF3090**	3.087	3.531	215.57	0.390	103
SB190	3.086	3.522	271.78	0.365	—	**NB190**	3.075	3.516	281.59	0.346	—
SF190	3.081	3.533	299.49	0.305	273	**NF190**	3.084	3.527	300.43	0.301	175
SB290	3.084	3.535	292.84	0.324	—	**NB290**	3.086	3.526	298.56	0.311	—
SF290	3.089	3.548	298.96	0.307	122	**NF290**	3.088	3.539	299.87	0.303	120
SB490	3.087	3.526	298.70	0.309	—	**NB490**	3.087	3.531	300.40	0.301	—
SF490	3.087	3.539	302.08	0.296	115	**NF490**	3.087	3.547	309.41	0.289	102
SB890	3.077	3.526	202.66	0.400	—	**NB890**	3.079	3.526	206.27	0.396	—
SF890	3.079	3.520	202.79	0.400	112	**NF890**	3.079	3.524	209.56	0.395	101

This fact is a clear indication for Fe substitution in MgB_2, first B atoms (either un-reacted or in MgB_2 structure) react with Fe atoms to from Fe_2B phase causing Mg content to increase then Fe atoms replace Mg atoms in the MgB_2 structure causing further increase in Mg phase. The values of lattice parameter *a* and lattice parameter *c* are given in Table 5.6. As can be seen in Figure 5.15b, a slight increase in lattice parameter *c* is observed as sintering time increases up to 4 hours at 900°C for all samples, coated or bare, while c axis shrinks again for annealing duration of 8 hours. Lattice parameter *c* for different groups of samples posses different values, in the order of NB, SB, NF, SF from smallest to largest and c parameters of the Fe coated samples are larger. A similar behaviour was also observed in RRR values. The difference becomes smaller when the sintering duration is extended to 8 hours.

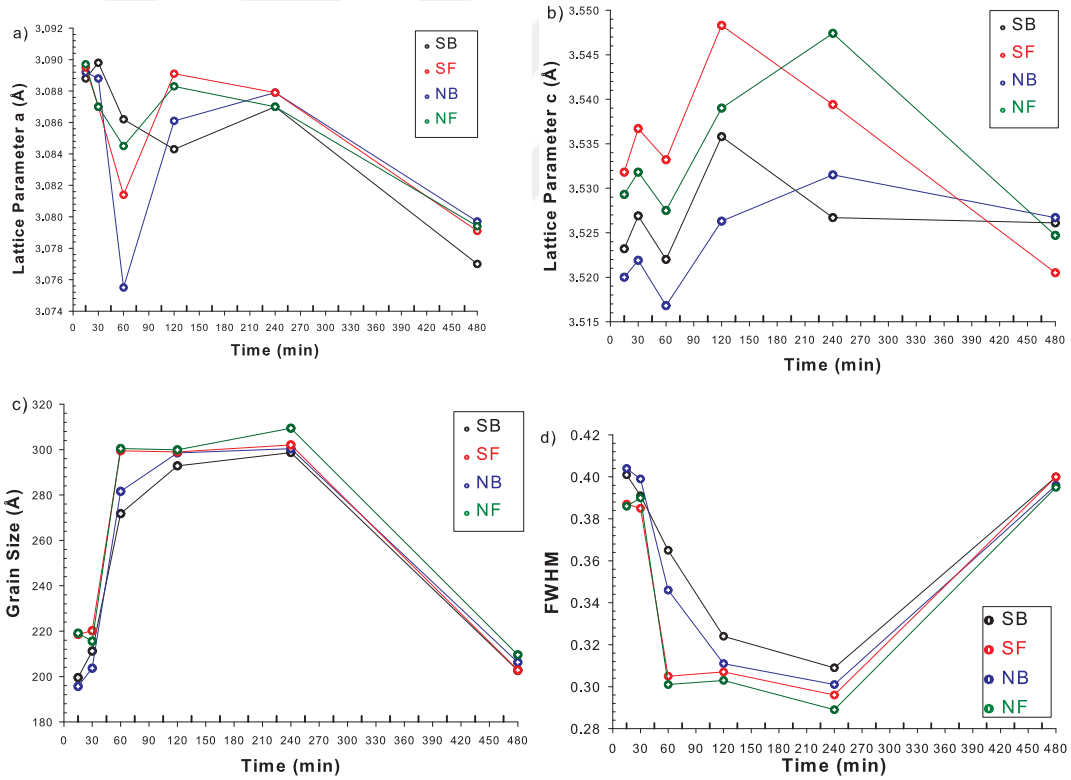

Figure 5.15. a) Lattice parameter *a*, b) Lattice parameter *c*, c) Grain size and d) FWHM behaviours for Fe coated and bare MgB_2 samples sintered for different times.

The grain size values of all samples were calculated as explained in the experimental chapter and the values obtained are displayed in Table 5.6 and Figure 5.15c.

The grain size is found to increase with increasing sintering duration from 15 minutes to 4 hours, then decreases for 8 hours. The reason for the fact that the lattice parameter c and grain size of the samples sintered for 8 hours have decreased to almost original values needs further attention. The surface of the Fe coated MgB_2 samples have smoother and denser appearance indicating that random grain growth in these samples are appreciably suppressed by the presence of Fe layer on the outer surface of the bulk samples. The grain size value calculated from XRD patterns are highest for NF490 (309 Å) and SF490 (302 Å) samples. Even though the differences in grain sizes are small for 2 hours and 4 hours sintering durations, grain sizes of Fe coated samples are significantly larger than those of bare samples. Increasing sintering time gave rise to grain growth in all samples up to 4 hours but main grain growth took place between 30 minutes and 1 hour. After 1 hour, little increase in the grain size was observed in bare samples but almost no increase in Fe coated samples. Analysis of the FWHM offers considerable information on the lattice strain in the sample. Among the XRD peaks, (101) diffraction peak was chosen for FWHM analysis and lattice strain was estimated from the FWHM values which are related to the lattice distortion. Lower value of FWHM for the SF490 samples (0.296°) gives evidence of strain effects that have occurred due to changes originate from Fe diffusion. This behaviour of the MgB_2 samples can be explained by the improvement of crystallinity with increasing the annealing time, resulting in increasing grain size. The FWHM values decrease with increasing the sintering time from 15 minutes to 4 hours for 900°C, as can be seen in Figure 5.15d. On the other hand, the sample NB1590 has highest value of FWHM (0.404°) gives evidence of strain effects, consequently, it has a smallest grain size of about 195.64 Å.

In the light of these findings we may argue that reaction kinetics during sintering is subject to progressive change, that is starting and end products of chemical reactions are different at different parts sintering duration. All these chemical reaction activities are mostly related to impurities and grain boundary regions since the main MgB_2 structure remain intact even after 8 hours of sintering.

5.3.2 Microstructural and Chemical Analysis

The surface morphology of the Fe coated and bare samples annealed for different sintering times were examined by SEM and the surface micrographs are displayed in Figure 5.16 and Figure 5.17. According to the results of the SEM investigation, it is found that the surface morphology, grain connectivity and grain size of the Fe coated samples improve with increasing sintering time up to 4 hours then decline (SB890, SF890, NB890 and NF890). The improvement of crystallinity is associated with better connectivity of the MgB_2 grains.

The SEM images given in Figure 5.16b, Figure 5.16d and Figure 5.16e display the Fe diffused surface of the samples sintered for 15 minutes 30 minutes and 1 hour at 900°C, while bare samples are displayed in the Figure 5.16a, Figure 5.16c, and Figure 5.16f. Also, Figure 5.17a to Figure 5.17f show surface micrographs for the SB290, SF290, SB490, SF490, SB890, and SF890 samples, bare samples being on the left and Fe coated ones on the right.

Figure 5.18 shows the EDS results of Fe coated and bare MgB_2 bulk superconductor for SB1590, SF1590, NB1590 and NF1590 samples. EDS analysis were done to obtain the chemical composition at the surface of the Fe coated samples. The total Mg, B, Fe and O contents in samples were determined from EDS spectrum. For this analysis of initially sintered samples, SB1590 was found to have 7.7 wt% oxygen content, and SF1590 10.9wt% oxygen content. Bare sample NB1590 was found to have 6.3 wt% oxygen, while NF1590 6.9wt% and oxygen. These results show that Fe coating and initial sintering cause higher oxygen content at the surface. Fe content at the coated surface was different for initially sintered and not initially sintered samples after sintering at 900°C for 15 minutes. This is probably due to slower diffusion of Fe atoms when the Fe coated samples are subjected to initial sintering prior to coating process. The sample annealed at 900°C for 8 hours shows more signs of partial melting due to high sintering temperature and long sintering duration.

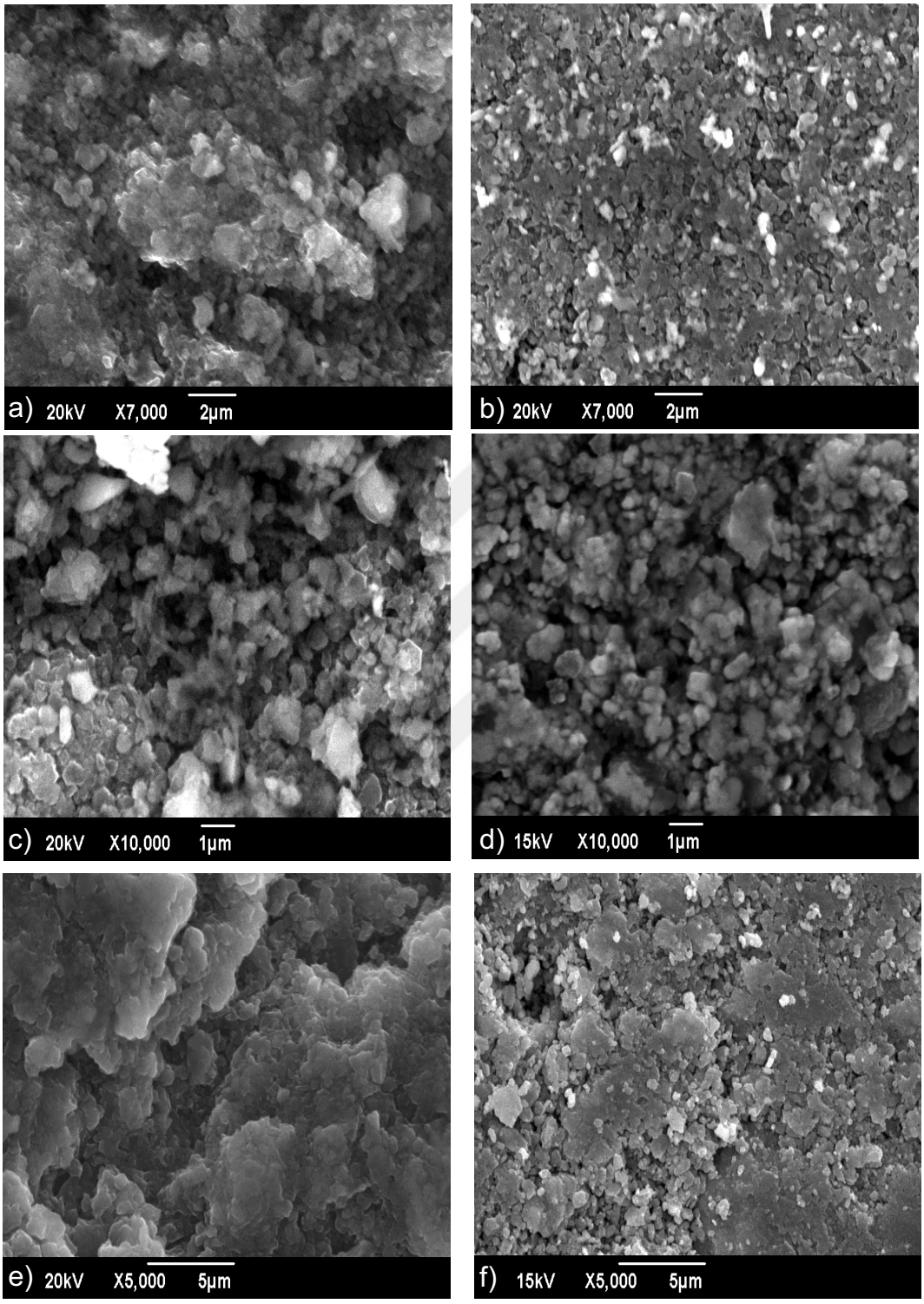

Figure 5.16. SEM images for a) SB1590, b) SF1590, c) SB3090, d) SF3090, e)SB190 and f) SF190 sample.

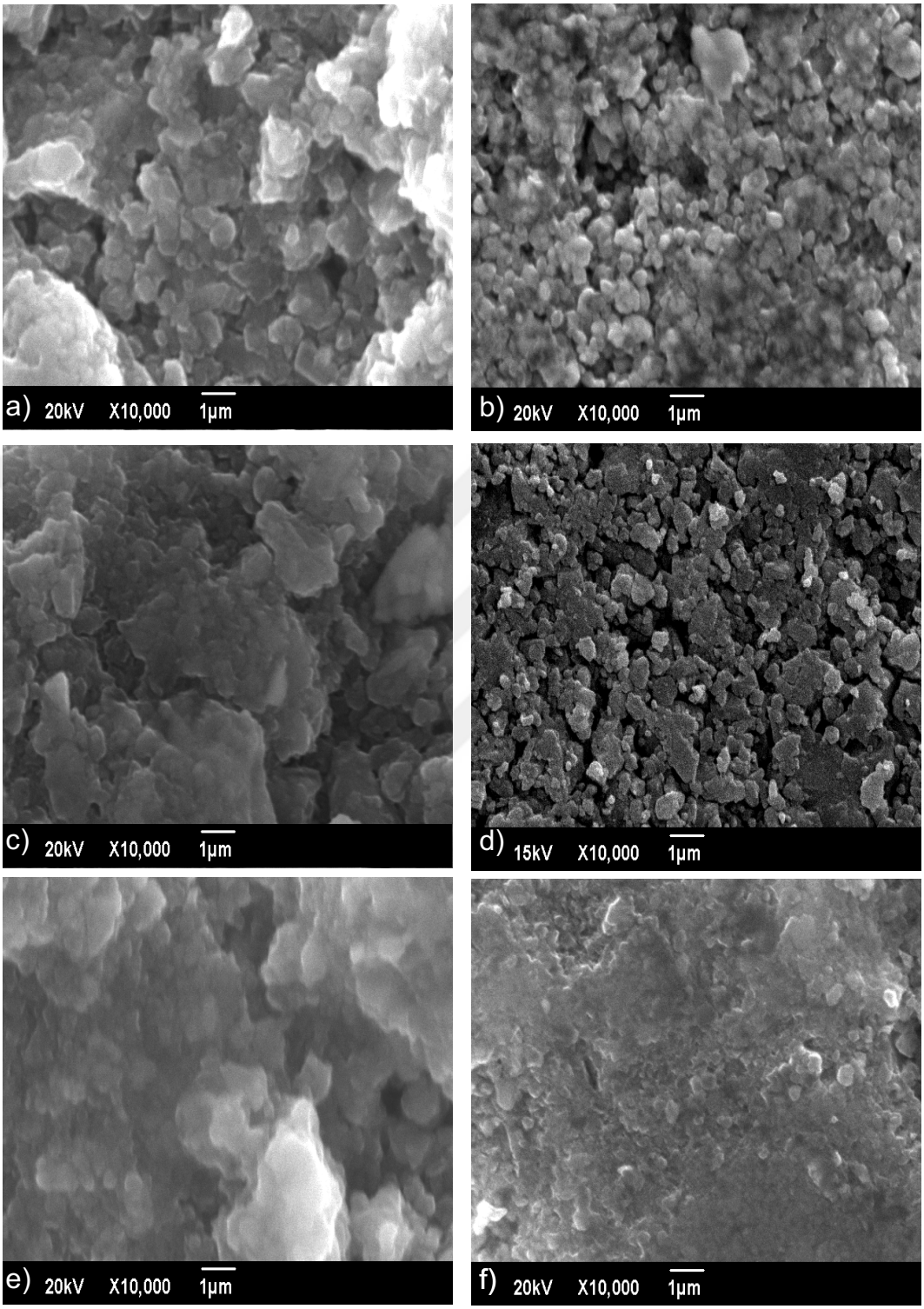

Figure 5.17. SEM images for a) SB290, b) SF290, c) SB490, d) SF490, e) SB890 and f) SF890 sample.

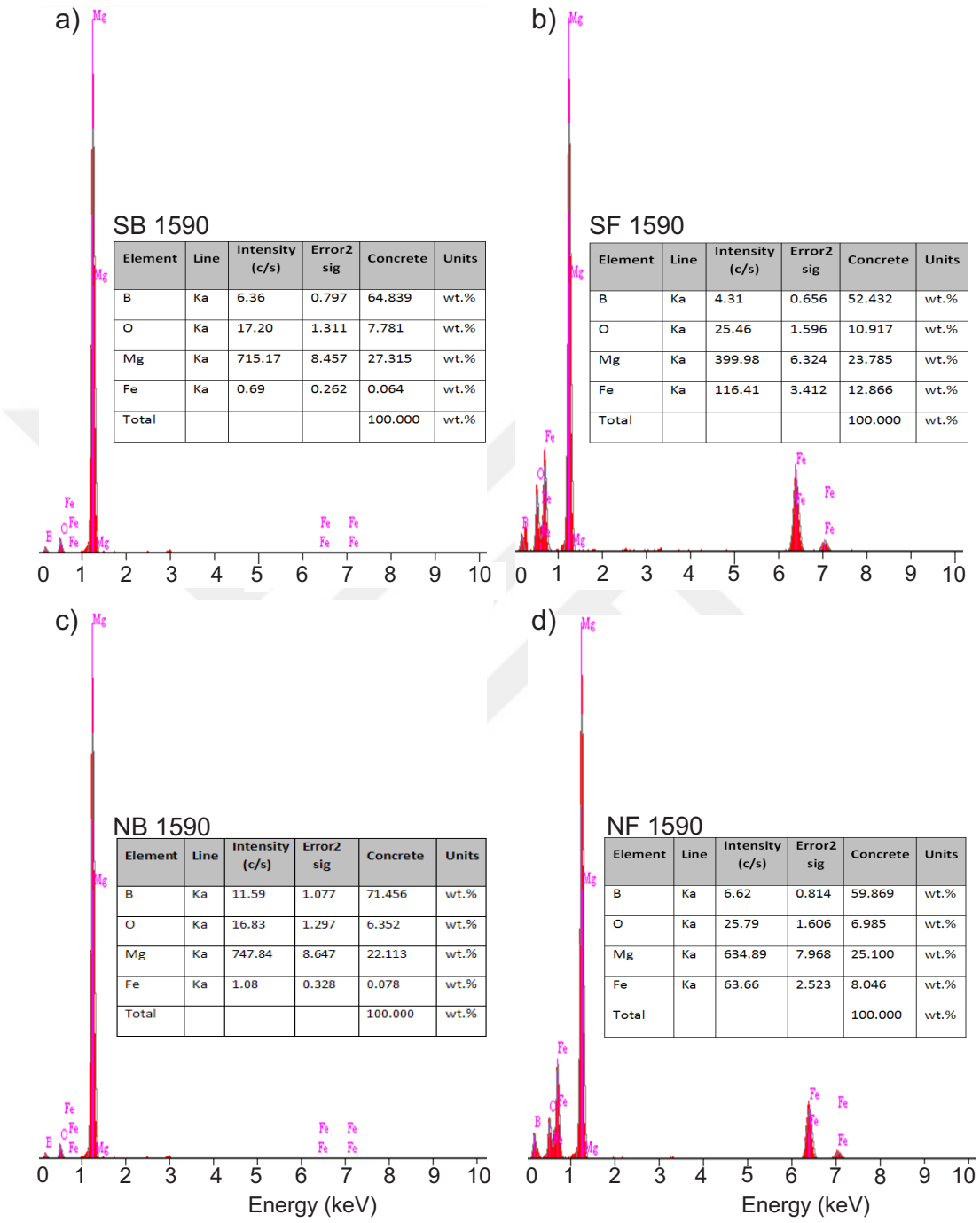

Figure 5.18. EDS analysis for a) SB1590, b) SF1590 (Fe-diffused side), c) NB1590 and d) NF1590 (Fe-diffused side) sample.

5.3.3 Electrical Resistivity Measurements

To investigate the effect of Fe coating on the superconducting properties of MgB_2 samples, we performed electrical resistivity measurements. These measurements were performed in the temperature range of 10 - 45 K. Figure 5.19 shows the resistivity variation with temperature for different sintering time durations. The inset magnifies the resistive transition region, in order to show more details. R-T curves, in Figure 5.19 is re-grouped with respect to their processing routes, given in Figure 5.20.

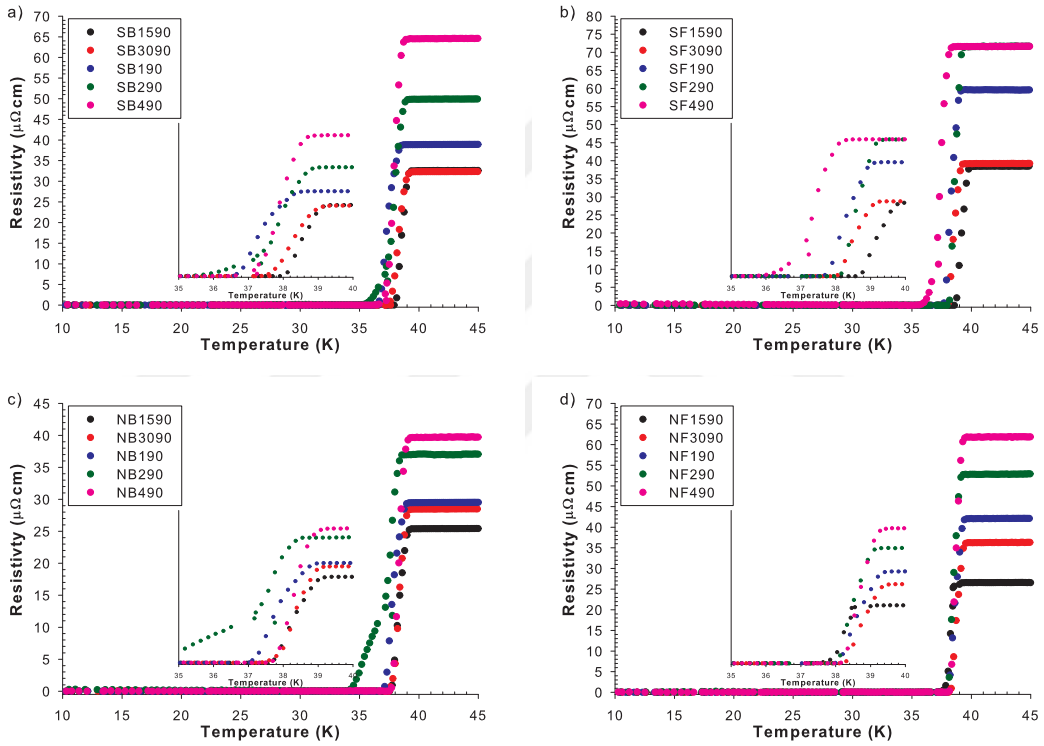

Figure 5.19. Resistance versus temperature curves for a) initially sintered bare samples (SB), b) initially sintered Fe coated samples (SF), c) not initially sintered bare samples (NB) and d) not initially sintered Fe coated samples (NF) for different sintered time durations.

The T_c^{offset}, T_c and 300 K resistivity of both sets given in Table 5.7 for different sintering times. Only a slight increase in T_c is observed due to Fe coating. Samples were mounted on the holder of the cryostat and room temperature resistivity values of all samples were calculated from I−V curves obtained.

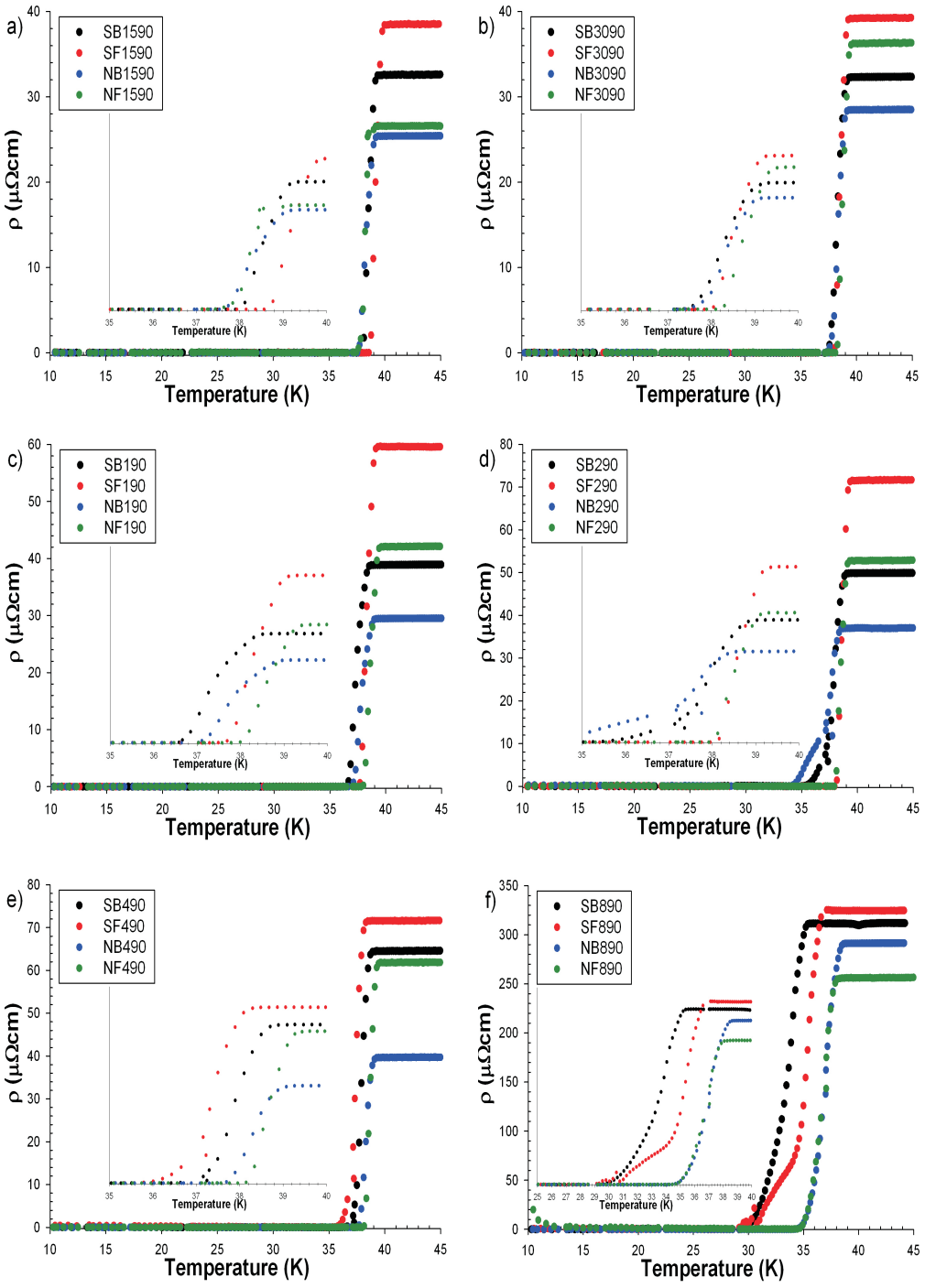

Figure 5.20. Resistance versus temperature curves for different sintering times.

Table 5.7. Transport measurement results for different sintering times showing the values for T_c^{offset}, T_c and room temperature resistivity.

Set 2S	T_c^{offset}	T_c	ρ_{300K}	**Set 2N**	T_c^{offset}	T_c	ρ_{300K}
Samples	(K)	(K)	($\mu\Omega$cm)	**Samples**	(K)	(K)	($\mu\Omega$cm)
SB1590	37.91	38.53	39.8	**NB1590**	37.13	38.04	33.0
SF1590	37.93	38.56	45.6	**NF1590**	37.74	38.16	38.4
SB3090	37.14	37.95	43.8	**NB3090**	37.22	38.19	35.9
SF3090	37.55	38.26	57.2	**NF3090**	37.89	38.50	43.6
SB190	36.18	37.04	59.8	**NB190**	36.63	37.49	41.2
SF190	37.28	37.90	82.0	**NF190**	37.78	38.20	57.6
SB290	35.25	37.85	60.1	**NB290**	34.46	37.17	44.7
SF290	37.75	38.37	84.4	**NF290**	37.71	38.12	63.5
SB490	36.63	37.69	63.3	**NB490**	37.49	38.30	47.0
SF490	36.00	37.31	95.4	**NF490**	37.76	38.34	71.4
SB890	30.27	32.75	514.1	**NB890**	34.33	36.26	444.9
SF890	30.09	33.61	471.5	**NF890**	34.35	36.29	453.3

As can be seen Figure 5.21, T_c^{offset}, T_c and ρ_{300K} values of Fe coated samples are higher and the difference widens up to 2 hours sintering duration then disappears. When the sintering duration is extended to 4 hours and 8 hours, Fe coating becomes ineffective and the effect of initial sintering becomes dominant with higher dominance in the case of 8 hours sintering. Furthermore, Fe coating lessens the deteriorating effect of initial sintering when sintering time is 8 hours long. Initially sintered and Fe diffused MgB_2 sample has higher T_c and lower ρ_{300K} than initially sintered bare sample which can be explained by noting the role of Fe in connecting the superconducting grains.

40 K resistivity of Fe coated samples are higher than bare ones for all sintering times, when the initial sintering is applied. Without initial sintering, 40 K resistivity of Fe coated samples do not follow a regular pattern but become lowest for 8 hours sintering duration while that of bare samples are lowest except 8 hours sintering duration.

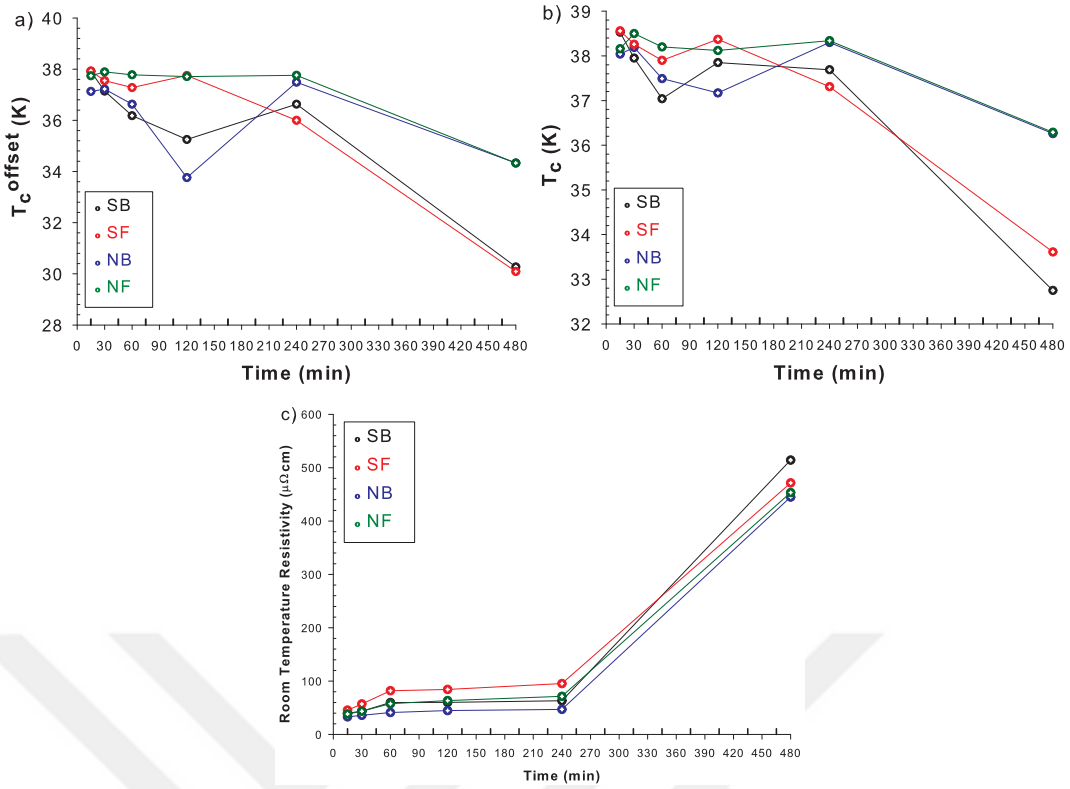

Figure 5.21. a) T_c^{offset}, b) T_c and c) ρ_{300K} behaviours for Fe coated and bare MgB_2 samples sintered for different times.

Besides, room temperature resistivity values exhibit slightly different behaviour. Room temperature resistivity values of all samples linearly increase up to 1 hr sintering duration then remain almost same up to 4 hours, and there is sharp increase from 4 hours to 8 hours.

Critical offset temperatures of Fe coated samples are higher for sintering times up to 2 hours although this effect is less pronounced in samples sintered before coating and sintered for longer time (up to 2 hours).

Diffusion of iron seems to be more critical for resistive superconducting transition temperatures in pre-sintered MgB_2 samples. As the annealing time increases from 15 min to 4 hr for Set 2S group of the room temperature resistivity value increase from 39.8 $\mu\Omega$cm to 95.4 $\mu\Omega$cm, respectively. Likewise, the room temperature resistivity values of Set 2N samples increase from 33 $\mu\Omega$cm to 71.4 $\mu\Omega$cm.

The ρ_{300K} is found to exhibit a linear increase with two different rates from 15 minutes to 4 hours sintering time and a sharp increase for 8 hours annealing duration. Fe coated samples exhibit much broader superconducting transitions and higher room temperature resistivity when sintered at 900°C for 8 hours. This degradation can not be attributed to the modified grain boundary properties alone.

As given in Table 5.7 and Figure 5.21b, SF1590 samples had highest critical temperature value, as T_c=38.56 K. On the other hand, SB890, SF890, NB890 and NF890 samples have lower T_c values of 32.75 K, 33.61 K, 36.26 K and 36.29 K, respectively. Thus, the MgB_2 superconducting material has an optimum annealing duration. When the sintering time is longer, both physical and superconducting properties of the material deteriorate.

Table 5.8 summarizes the residual resistivity ratio, difference between resistivities at 40 K and 300 K, and active area fraction for the Fe coated and bare MgB_2 samples. Since higher A_F values mean better connectivity, the increased A_F values reveal that the inter grain connectivity has been improved due to Fe diffusion, irrespective of the production route, although Fe coated samples show better improvement than the bare samples, as seen in Figure 5.22a.

Increased electrical conductivity have resulted in a higher A_F for SF1590 samples. As seen from Table 5.8, the sample SF1590 has highest A_F value of 0.60 and this sample also has a better critical temperature of T_c=38.56 K. On the other hand, this sample has a very small RRR value and lowest $\Delta\rho$ value of 8.1 $\mu\Omega$cm. The lowest A_F values were obtained for the samples annealed at 900°C for 8 hours.

The ratio of the resistivity causes a reduction, when the electron scattering is high. The RRR values of Fe coated samples are smaller than that of the bare samples as seen in Figure 5.22b. Therefore, variations in the resistivity of the bare and coated samples depend on the combined effect of the connectivity factor due to Fe and MgB_2.

Table 5.8. Residual resistivity ratio, resistivity difference between 300 K and 40 K, and active area fraction of Set 2S and Set 2N samples.

Set 2S Samples	RRR	$\Delta\rho$ ($\mu\Omega$cm)	A_F	**Set 2N Samples**	RRR	$\Delta\rho$ ($\mu\Omega$cm)	A_F
SB1590	1.221	8.2	0.597	**NB1590**	1.299	8.6	0.566
SB3090	1.356	11.5	0.374	**NB3090**	1.260	8.4	0.581
SB190	1.223	10.9	0.394	**NB190**	1.230	8.7	0.558
SB290	1.204	10.2	0.422	**NB290**	1.215	8.9	0.544
SB490	1.229	11.8	0.364	**NB490**	1.187	8.4	0.581
SB890	1.658	204.1	0.021	**NB890**	1.526	153.4	0.028
SF1590	1.184	8.1	0.606	**NF1590**	2.824	11.8	0.364
SF3090	1.459	18.0	0.239	**NF3090**	1.201	8.3	0.589
SF190	1.376	22.4	0.192	**NF190**	1.223	10.5	0.410
SF290	1.180	12.9	0.333	**NF290**	1.200	10.6	0.406
SF490	1.334	13.9	0.180	**NF490**	1.152	9.4	0.457
SF890	1.450	145.0	0.029	**NF890**	1.765	196.5	0.022

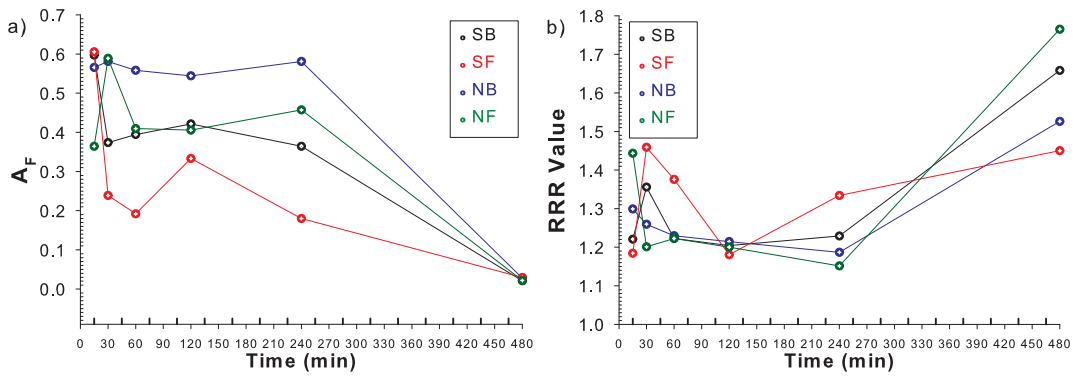

Figure 5.22. a) Active area fraction and b) Residual resistivity ratio value behaviours for Fe coated and bare MgB_2 samples sintered for different times.

5.4 Calculations of Diffusion Coefficient and Activation Energy

This section contains the results of Fe diffusion effects on MgB_2 superconducting samples for different sintering times and temperatures. These results were obtained by monitoring the changes in lattice parameters and room temperature resistivity values. The active diffusivity may be presented by the diffusion in condensed matter and the pore space of porous media (Grathwohl, 1998). The most common methods for studying diffusion in superconductors are resistivity measurements including successive removal of thin layers and measurements of lattice parameters from XRD patterns and EDXRF methods (Abdullaev and Dzhafarov, 1987).

Here, XRD and room temperature resistivity methods are employed to determine the diffusion coefficient of Fe into MgB_2 superconductor. We studied depth profile for the changes in these physical quantities by successive removal of thin layers (about of 25 μm) from Fe diffused surface of the samples.

The data about the concentration profile of the diffusing impurity in the Fe-diffused sample can be found by measuring the distribution of deformation ($\Delta c/c_0$) over a certain thickness of the samples. Δc is the change in the value of lattice parameter c with respect to each step and c_0 is lattice parameter c value of bare MgB_2 pellets. The ratio of $\Delta c/c_0$ is related with Fe diffusion concentration profile.

Another technique for studying diffusion is to determine the changes in room temperature resistivity ($\Delta\rho/\rho_0$) over the thickness of the samples, where $\Delta\rho$: change in ρ_{300K} for each step and ρ_0: ρ_{300K} value of bare MgB_2 pellets. The process for removal of thin layers was repeated eight times in total, and as a result the Fe diffused MgB_2 samples were excavated to a depth of 200 μm on average.

Lattice parameter c and ρ_{300K} values were used to estimate the shallow surface concentration of Fe diffusion into MgB_2. XRD and room temperature resistivity methods are employed to determine the diffusion coefficient of Fe into MgB_2 superconductor.

The finally in this section, diffusion coefficient versus $1/T$ can be used to determine the activation energy required for diffusion of Fe atoms into MgB_2. In the Arrhenius plot, D represents the rate of the diffusion process.

5.4.1 Temperature Dependence of Fe Diffusion into MgB_2

In this study, we have calculated the diffusion coefficients of Fe diffusion in MgB_2 superconductors at different sintering temperatures. The XRD patterns of Fe coated samples sintered temperature between 650°C and 900°C for 1 hour were shown in Figure 5.23 and Figure 5.24 analyzed at each step. As shown in these figure, below a depth of about 50 μm the peak near 45° which represents Fe_2B disappears in these samples, while lattice parameter c values continue to change.

Table 5.9 summarizes the lattice parameter c and room temperature resistivity for samples of Set 1S and Set 1N. The refinement results reveal that the a-parameter does not have significant changes, so lattice parameter a value of coated sample at all step are close and approximately around 3.08 Å; on the other hand, the lattice parameter c of coated MgB_2 samples varies between 3.523 Å and 3.540 Å, as can be seen Table 5.9.

For all samples, I−V characterizations were measured at room temperature, and the ρ_{300K} were determined. To obtain the resistivity at the room temperature, potential difference was recorded while a DC current was applied and gradually increased. ρ_{300K} values were determined to be between 37.45 $\mu\Omega$cm and 82.07 $\mu\Omega$cm. The ρ_{300K} of coated MgB_2 samples are listed in Table 5.9.

We calculated concentration profile of Fe in MgB_2 at the initial and final stages of impurity diffusion from a constant source into semi-infinite solid. We obtained profile of the lattice parameter c and room temperature resistivity in 8 steps within the 200 μm depth from the coated surface of our samples, as shown Figure 5.25 and Figure 5.26.

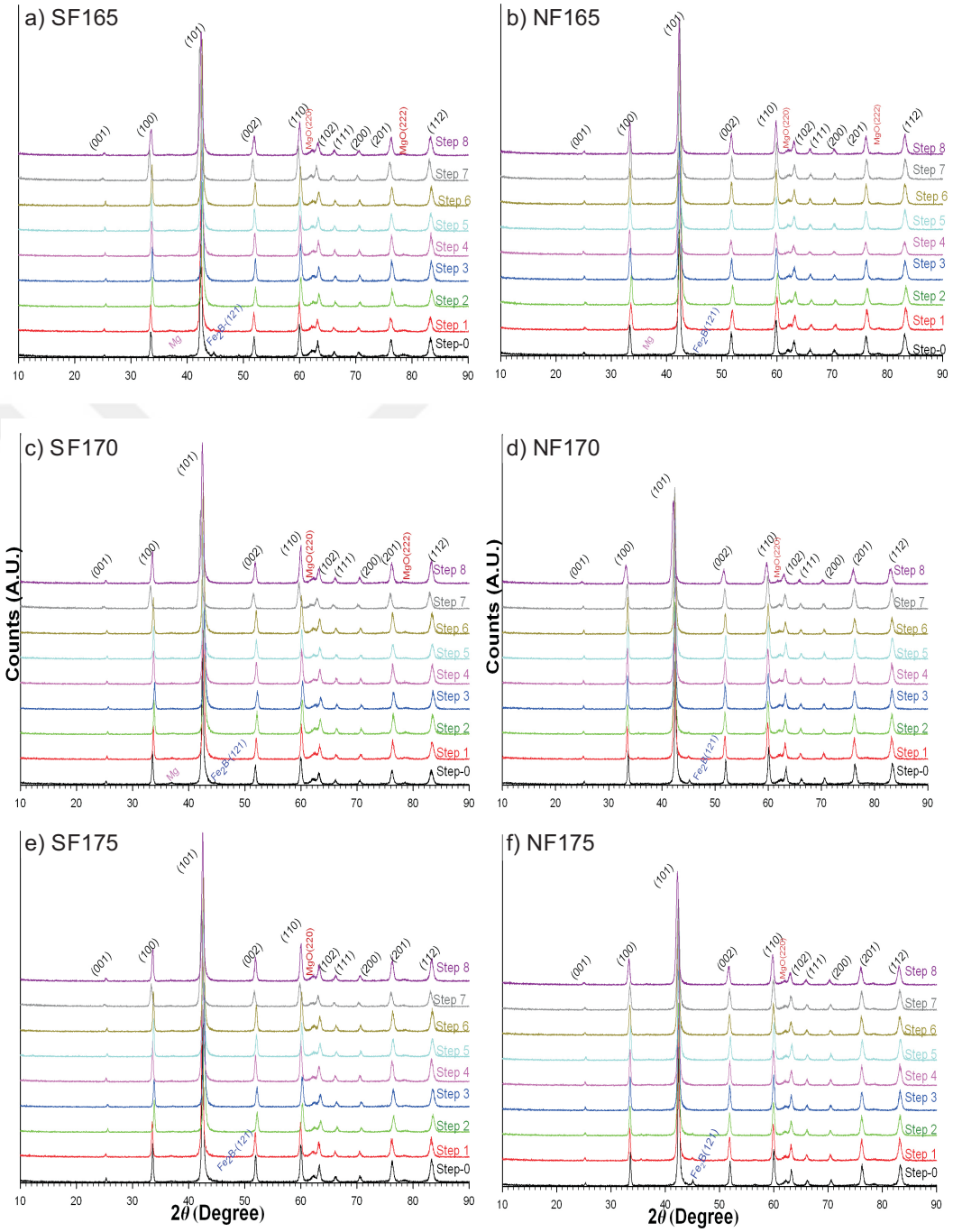

Figure 5.23. XRD patterns of Fe diffused samples of sintered between 650 and 750°C for 1 hour.

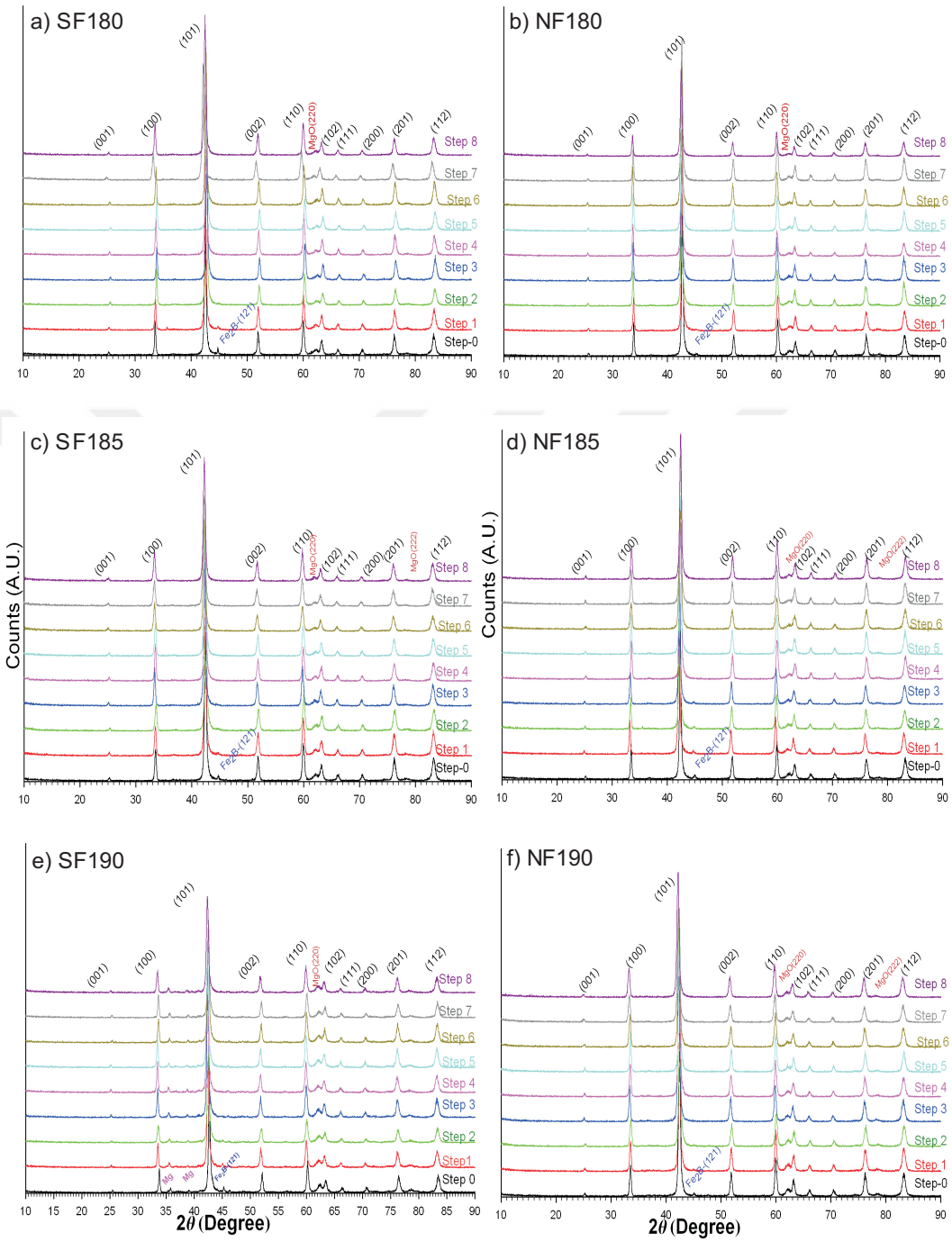

Figure 5.24. XRD patterns of Fe diffused samples of sintered between 800 and 900°C for 1 hour.

Table 5.9. Lattice parameter c (Å) and room temperature resistivity ($\mu\Omega$cm) values at successive steps.

Steps	SF165	NF165	SF170	NF170	SF175	NF175	SF180	NF180	SF185	NF185	SF190	NF190
	Prm. c	Prm. c	Prm. c	Prm. c	Prm. c	Prm. c	Prm. c	Prm. c	Prm. c	Prm. c	Prm. c	Prm. c
Step0	3.525	3.531	3.523	3.529	3.524	3.530	3.531	3.526	3.538	3.540	3.533	3.528
Step1	3.524	3.531	3.522	3.527	3.523	3.529	3.529	3.525	3.536	3.539	3.531	3.526
Step2	3.522	3.528	3.521	3.525	3.522	3.528	3.528	3.524	3.534	3.538	3.528	3.526
Step3	3.521	3.527	3.520	3.525	3.520	3.524	3.527	3.522	3.533	3.537	3.527	3.524
Step4	3.521	3.524	3.520	3.522	3.519	3.521	3.526	3.518	3.532	3.533	3.524	3.523
Step5	3.520	3.524	3.520	3.522	3.519	3.521	3.525	3.518	3.532	3.532	3.523	3.520
Step6	3.520	3.524	3.519	3.521	3.518	3.520	3.524	3.517	3.530	3.530	3.522	3.517
Step7	3.520	3.524	3.519	3.520	3.518	3.520	3.524	3.517	3.530	3.530	3.522	3.517
Step8	3.520	3.524	3.519	3.520	3.518	3.520	3.524	3.516	3.530	3.530	3.522	3.517

Steps	ρ_{300K}	ρ_{300K}	ρ_{300K}	ρ_{300K}	ρ_{300K}	ρ_{300K}	ρ_{300K}	ρ_{300K}	ρ_{300K}	ρ_{300K}	ρ_{300K}	ρ_{300K}
Step0	43.99	37.45	51.46	41.49	55.78	40.55	68.61	47.22	71.80	43.06	82.07	57.68
Step1	43.08	36.29	50.41	38.84	52.70	40.55	64.41	43.20	66.91	42.06	74.70	55.37
Step2	42.02	35.93	48.39	38.71	51.56	40.13	63.19	41.47	62.93	41.71	69.44	51.27
Step3	41.45	35.84	47.88	38.16	51.10	39.76	61.33	40.28	62.28	41.11	63.46	46.88
Step4	40.64	35.82	47.33	37.89	50.41	38.72	59.56	39.66	60.91	40.82	61.48	46.18
Step5	40.59	35.78	46.38	37.08	49.50	37.88	58.42	39.04	58.75	40.71	60.52	43.71
Step6	40.58	35.74	46.07	37.05	48.32	37.86	57.85	39.04	58.24	40.70	59.98	42.86
Step7	40.57	35.74	45.85	37.04	48.30	37.71	57.80	39.03	58.20	40.70	59.86	42.42
Step8	40.57	35.73	45.70	37.04	48.30	37.71	57.80	39.03	58.20	40.70	59.86	42.16

The concentration profile depends on the sintering temperature (650-900°C/1h). Figure 5.25 and Figure 5.26 give the variation of lattice parameter ($\Delta c/c_o$), and the variation of room temperature resistivity ($\Delta\rho/\rho_o$) as a function of thickness of sample subjected to iron diffusion at different temperatures, respectively.

Fe diffusion in the MgB_2 superconductor materials depends strongly on the diffusion-sintering temperature. Fe diffusion coefficients for MgB_2 samples sintered at different temperatures were obtained by using changes in lattice parameter c and room temperature resistivity values. Then we calculated diffusion coefficients from these profiles using the Equation 2.7, values of these coefficients are given in Table 5.10.

The data in Figure 5.25 and Figure 5.26 are fitted to Equation 2.7 by using a non-linear least-square fit procedure, the resulting concentration profile is plotted with the solid curve in this figure. Fe diffusion coefficients for samples of Set 1S and Set 1N in this table were obtained by using lattice parameter c values and room temperature resistivity values.

Table 5.10. Fe diffusion coefficients (D) for different sintering temperatures for 1 hour.

MgB_2 Sample Code	Calculated c value D_1 (cm^2/s)	Calculated ρ_{300K} value D_2 (cm^2/s)	**MgB_2 Sample Code**	Calculated c value D_3 (cm^2/s)	Calculated ρ_{300K} value D_4 (cm^2/s)	Sintering Temp. (°C)
SF165	5.4882E-10	6.0840E-10	**NF165**	8.8660E-10	5.0561E-10	650
SF170	2.0100E-09	2.2285E-09	**NF170**	3.0789E-09	2.8322E-09	700
SF175	3.4071E-09	4.1320E-09	**NF175**	5.3192E-09	1.3276E-09	750
SF180	5.1247E-09	6.5374E-09	**NF180**	7.2495E-09	6.4196E-09	800
SF185	7.0644E-09	7.8876E-09	**NF185**	9.7812E-09	8.3131E-09	850
SF190	9.3032E-09	9.5373E-09	**NF190**	1.1466E-08	1.0179E-08	900

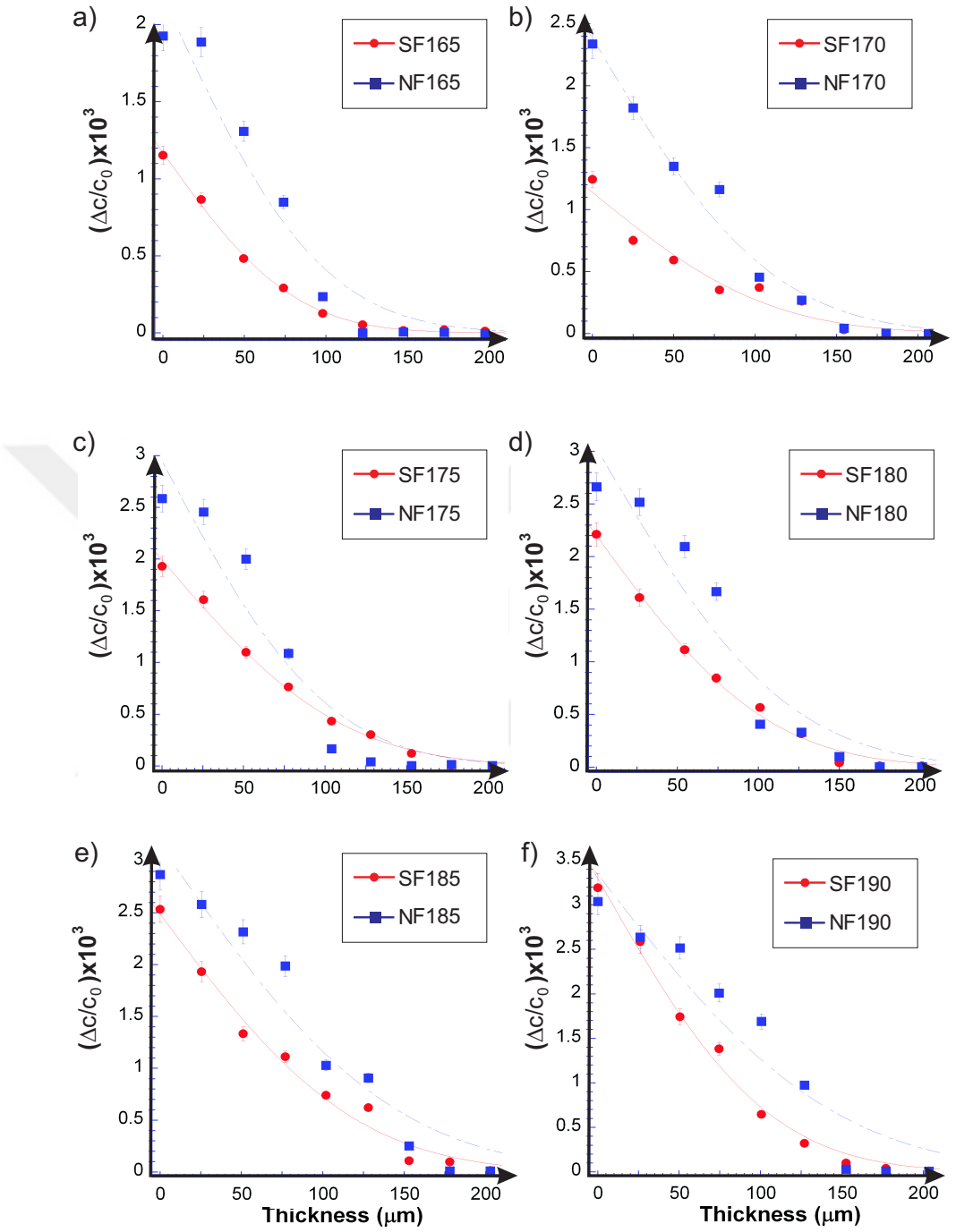

Figure 5.25. Concentration profile of Fe versus the thickness for a) SF165-NF165, b)SF170-NF170, c) SF175-NF175, d) SF180-NF180, e) SF185-NF185 and f) SF190-NF190 samples calculated by changes in lattice parameter *c*.

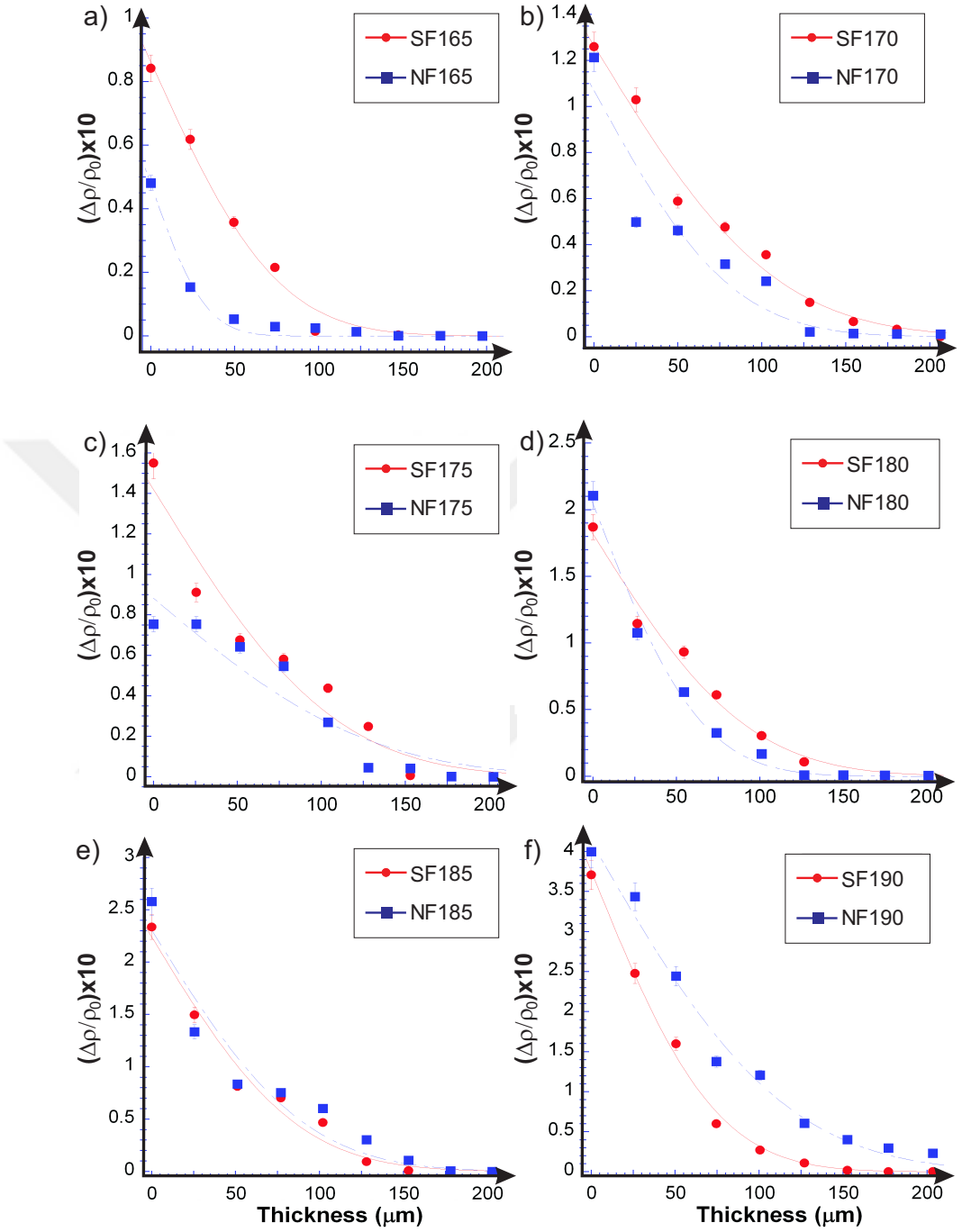

Figure 5.26. Concentration profile of Fe versus the thickness for a) SF165-NF165, b)SF170-NF170, c) SF175-NF175, d) SF180-NF180, e) SF185-NF185 and f) SF190-NF190 samples calculated by changes in ρ_{300K}.

5.4.2 Time Dependence of Fe Diffusion into MgB_2

Figure 5.27 and Figure 5.28 show the X-ray diffraction patterns between 10° and 90° for the Fe diffused MgB_2 sample sintered at different temperatures in eight steps. All samples studied in this work exhibite polycrystalline superconducting phase. After a depth of about 50 μm (second or third step), these figure shows that the peaks near 45° which represent Fe_2B are not observed in these samples. In range of fourth to eight steps, after the $\sim 100-120$ μm depth, both lattice parameter c and room temperature resistivity measurements produce very close values.

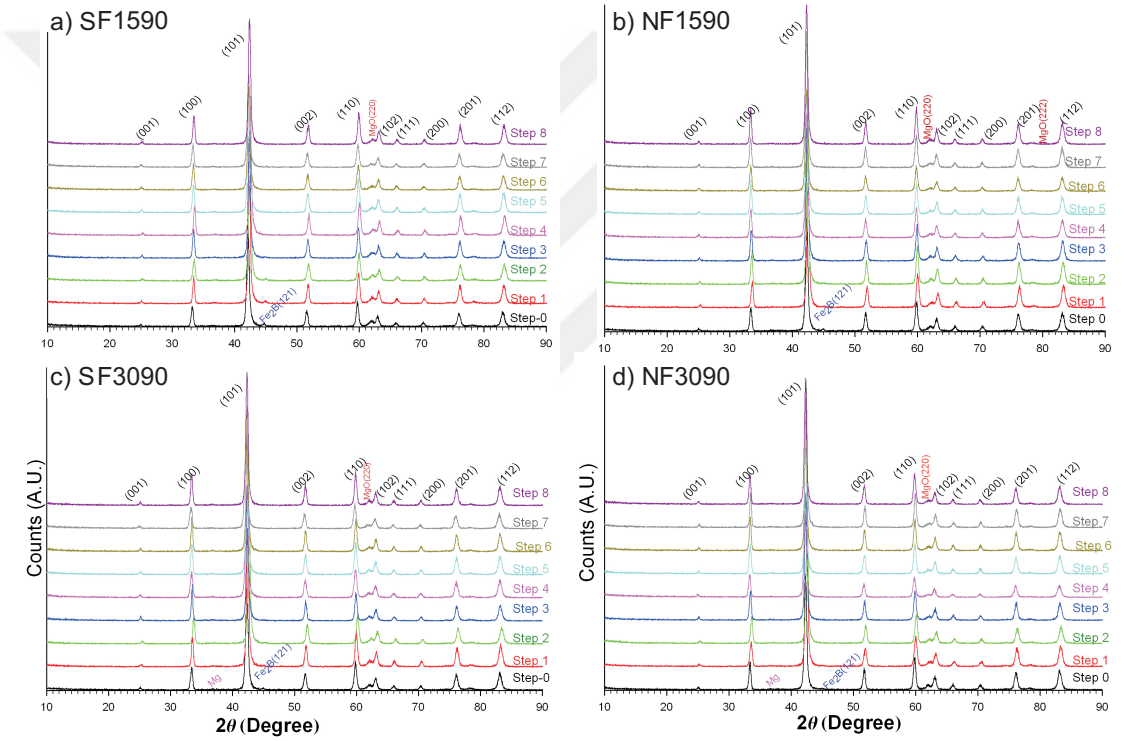

Figure 5.27. XRD patterns for all steps belonging to the samples a) SF1590, b) NF1590, c) SF3090 and d) NF3090.

Table 5.11 summarizes the lattice parameter c and room temperature resistivity for different sintering time durations. Careful examination of our results (not included in this thesis) revealed that the a-parameter tends to remain almost constant along the depth of the samples, so the lattice parameter a value of coated sample at all steps are close and approximately around 3.08 Å.

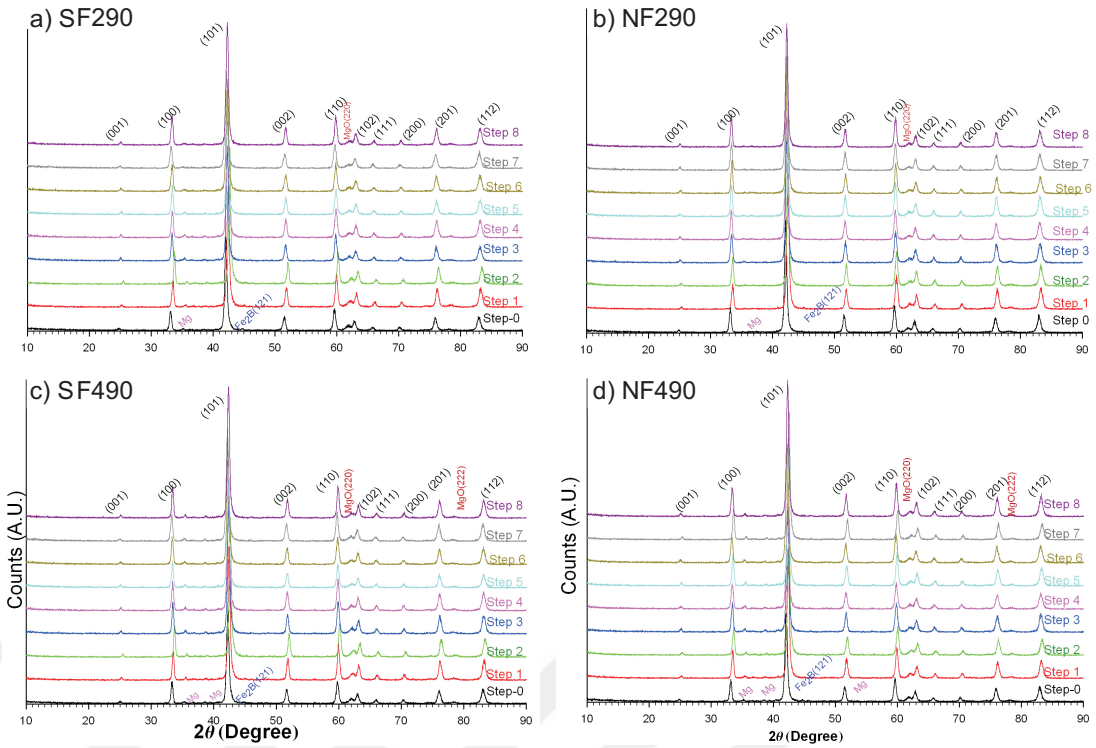

Figure 5.28. XRD patterns for all steps belonging to the samples a) SF290, b) NF290, c) SF490 and d) NF490.

The lattice parameter c of Fe diffused samples varies between 3.521 Å and 3.547 Å, Fe coated samples having larger c parameter. In addition, the value of resistivity at room temperature varies between 33.01 $\mu\Omega$cm and 95.40 $\mu\Omega$cm.

We have calculated concentration profile of Fe in MgB_2 at the initial and final stages of impurity diffusion from a constant source into semi-infinite solid. We obtained profiles of the lattice parameter c and room temperature resistivity with the depth from the coated surface of our samples, as given in Figure 5.29 and Figure 5.30, respectively. Fe concentration decreases with depth down to 200 μm. We calculated diffusion coefficients from these profiles using the Equation 2.7.

The data in Figure 5.29 and Figure 5.30 are fitted to Equation 2.7 by using a nonlinear least-square fit procedure, the resulting concentration profile is plotted with the solid curve in these figures. Then we calculated diffusion coefficients from these profiles using the Equation 2.7, the obtained diffusion coefficient values for different sintering times are given in Table 5.12.

Table 5.11. Lattice parameter c (Å) and room temperature resistivity ($\mu\Omega$cm) values obtained in eight steps by successive removal of thin layers.

Steps	SF1590	NF1590	SF3090	NF3090	SF190	NF190	SF290	NF290	SF490	NF490	SF890	NF890
	Prm. c	Prm. c	Prm. c	Prm. c	Prm. c	Prm. c	Prm. c	Prm. c	Prm. c	Prm. c	Prm. c	Prm. c
Step0	3.532	3.529	3.537	3.532	3.533	3.527	3.548	3.539	3.539	3.547	3.521	3.525
Step1	3.531	3.527	3.536	3.529	3.531	3.526	3.546	3.538	3.537	3.543	—	—
Step2	3.529	3.526	3.534	3.526	3.528	3.525	3.545	3.537	3.536	3.541	—	—
Step3	3.529	3.525	3.533	3.525	3.527	3.524	3.541	3.533	3.533	3.540	—	—
Step4	3.526	3.522	3.530	3.525	3.524	3.523	3.539	3.533	3.529	3.537	—	—
Step5	3.524	3.521	3.527	3.524	3.523	3.520	3.537	3.529	3.528	3.532	—	—
Step6	3.523	3.521	3.527	3.523	3.522	3.517	3.537	3.527	3.527	3.532	—	—
Step7	3.523	3.520	3.527	3.523	3.522	3.517	3.536	3.527	3.527	3.532	—	—
Step8	3.523	3.520	3.527	3.522	3.522	3.517	3.536	3.527	3.527	3.532	—	—

Steps	ρ_{300K}	ρ_{300K}	ρ_{300K}	ρ_{300K}	ρ_{300K}	ρ_{300K}	ρ_{300K}	ρ_{300K}	ρ_{300K}	ρ_{300K}	ρ_{300K}	ρ_{300K}
Step0	43.69	38.49	57.26	43.62	82.07	57.68	84.42	63.50	95.40	71.42	20279	20956
Step1	42.07	36.33	50.08	42.04	74.70	55.37	80.99	61.74	89.30	69.09	—	—
Step2	41.02	35.07	47.56	40.09	69.44	51.27	75.17	56.62	85.49	63.96	—	—
Step3	40.41	34.02	45.75	38.94	63.46	46.88	68.53	52.14	76.71	58.65	—	—
Step4	40.15	33.47	44.56	37.06	61.48	46.18	65.85	49.78	70.95	53.42	—	—
Step5	39.98	33.23	44.09	36.34	60.52	43.71	63.39	47.62	66.72	49.41	—	—
Step6	39.91	33.05	43.94	36.11	59.98	42.86	61.78	46.80	65.56	48.09	—	—
Step7	39.88	33.02	43.93	36.02	59.87	42.42	60.77	46.01	64.55	47.82	—	—
Step8	39.85	33.01	43.90	35.91	59.86	42.16	60.57	45.50	63.51	47.50	—	—

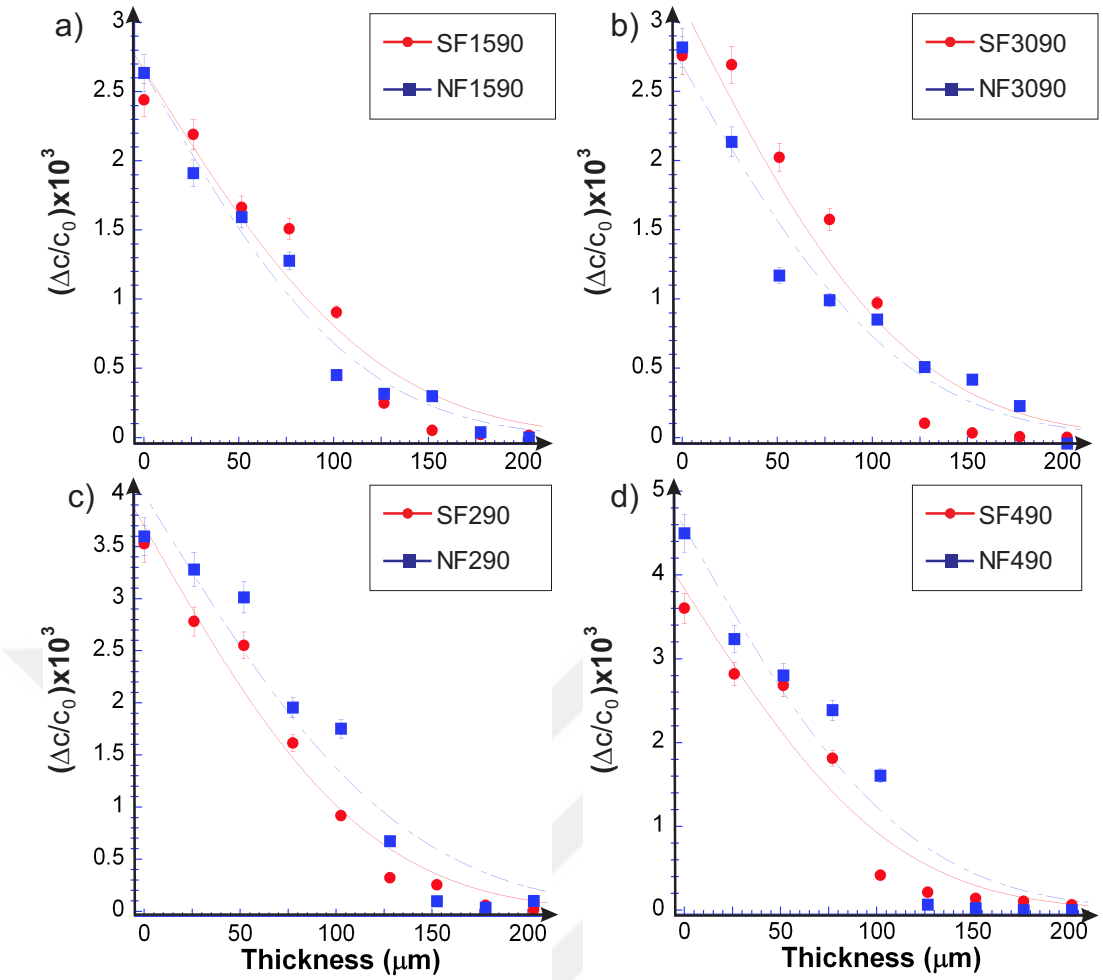

Figure 5.29. Concentration profiles of Fe versus the thickness for a) SF1590-NF1590, b)SF3090-NF3090, c) SF290-NF290 and d) SF490-NF490 samples calculated by changes in lattice parameter *c*.

Fe diffusion coefficients for samples of Set 2S (second and third column) and Set 2N (fifth and sixth column) in this table were calculated using lattice parameter *c* and room temperature resistivity values. It is found that the Fe diffusion coefficient decreases with increasing sintered time, as expected (Loskutov, 2012 and Gao, 2013). The mean values of the diffusion coefficients of Fe diffused MgB_2 as a function of time are given in Figure 5.31.

In Table 5.12, Fe diffusion coefficients represent diffusion coefficients of Set 2S and Set 2N which were calculated for lattice parameter and room temperature resistivity of Set 2N, respectively.

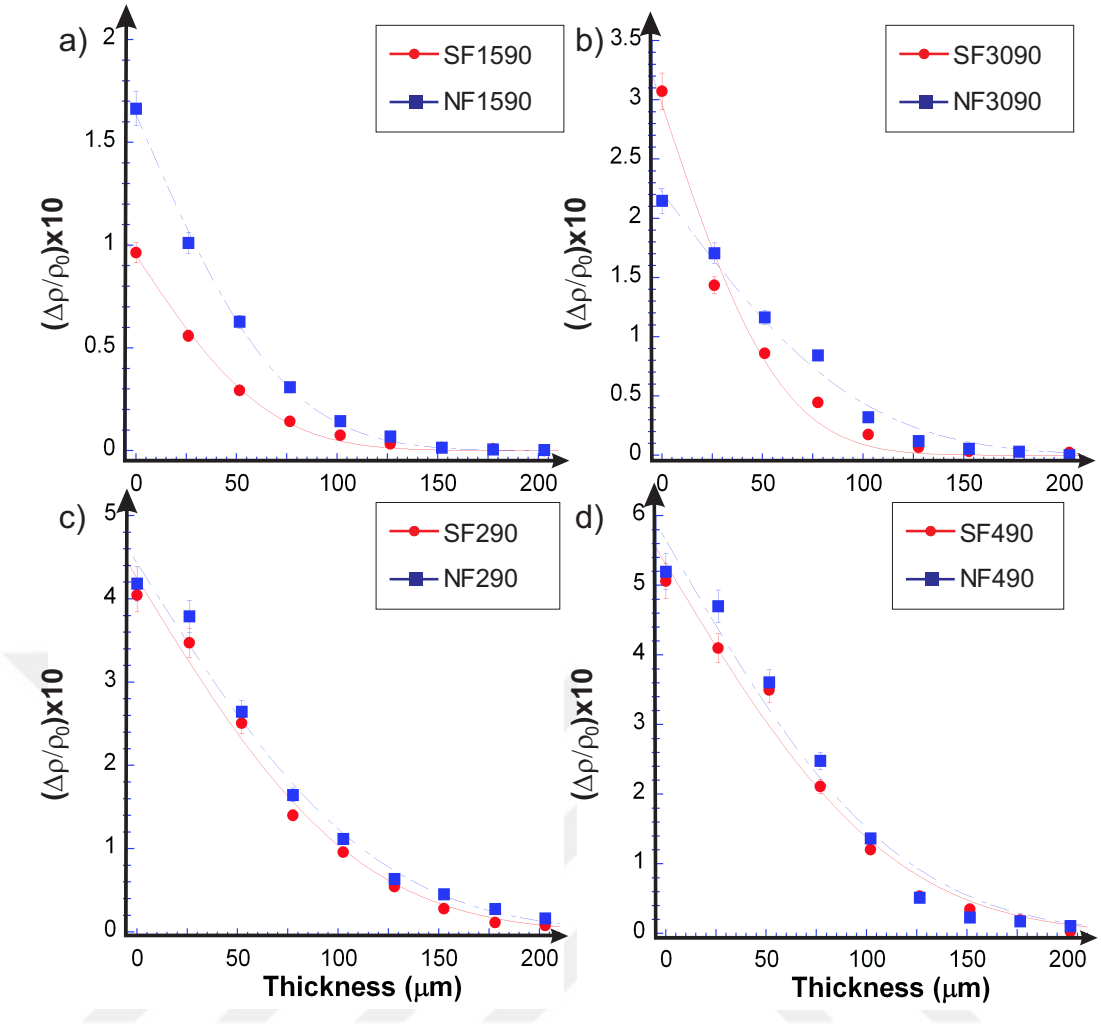

Figure 5.30. Concentration profiles of Fe versus the thickness for a) SF1590-NF1590, b)SF3090-NF3090, c) SF290-NF290 and d) SF490-NF490 samples calculated by changes in ρ_{300K}.

In case of the sintering at 900°C for 8 hour, the Fe_2B phase vanish to a large extend, while both the Mg and MgO peaks become much more significant in the spectrum. Fe diffusion coefficients for SF890 and NF890 samples were not calculated, since Mg is ductile, melts at 650°C and is easily vaporized (boiling point is 1050°C). It has been reported in literature that phase diagram for single crystals of MgB_2 at 3 GPa shows a Mg-MgB_2 eutectic at 840 K and MgB_2 melting point around 2500 K (Turkevich et al., 2003 and Karpinski et al., 2007).

Table 5.12. Fe diffusion coefficients for different sintering times at 900°C.

MgB_2 Sample Code	Calculated c value $D^{(1)}$ (cm^2/s)	Calculated ρ_{300K} value $D^{(2)}$ (cm^2/s)	MgB_2 Sample Code	Calculated c value $D^{(3)}$ (cm^2/s)	Calculated ρ_{300K} value $D^{(4)}$ (cm^2/s)	Sintering Time (hours)
SF1590	2.3763E-08	2.6413E-08	**NF1590**	2.5001E-08	5.8636E-08	0.25
SF3090	1.9180E-08	1.5100E-08	**NF3090**	1.8366E-08	5.5212E-08	0.50
SF190	9.3032E-09	9.5373E-09	**NF190**	1.1466E-08	1.1092E-08	1
SF290	9.0343E-09	9.2665E-09	**NF290**	1.1108E-08	1.0862E-09	2
SF490	7.3348E-09	8.3798E-09	**NF490**	1.0630E-08	8.7873E-09	4
SF890	-	-	**NF890**	-	-	8

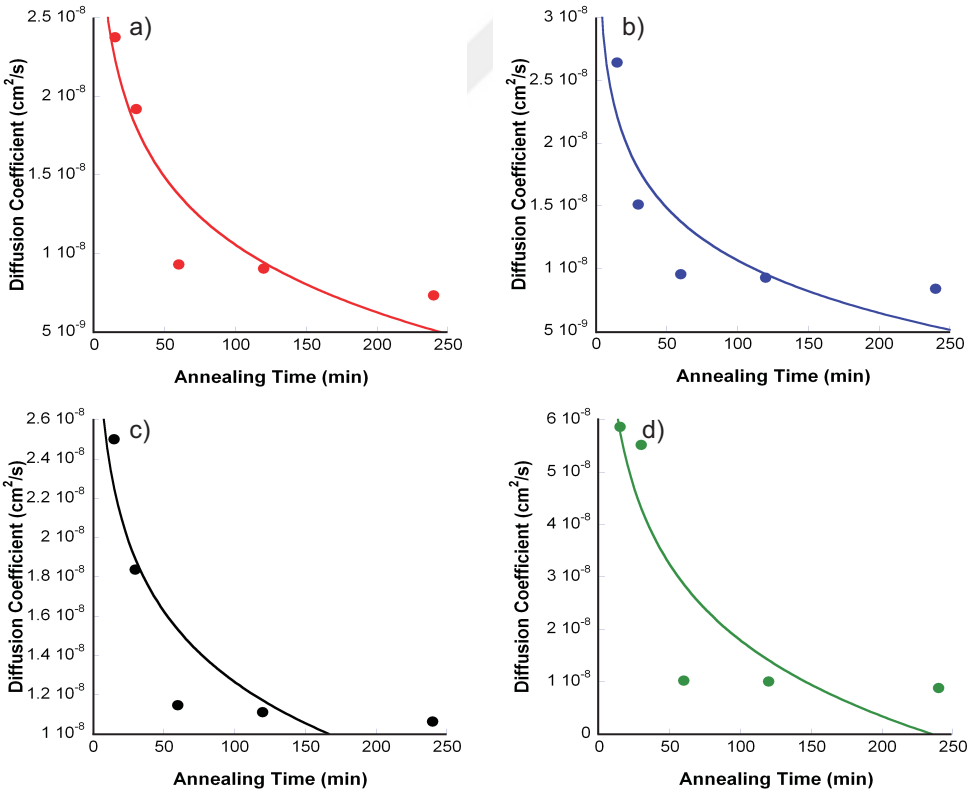

Figure 5.31. The dependence of Fe diffusion coefficient on sintering time duration; a) $D^{(1)}$ SF/Latt. prm. c, b) $D^{(2)}$ SF/ρ_{300K}, c) $D^{(3)}$ NF/Latt. prm. c and d) $D^{(4)}$ NF/ρ_{300K}.

5.4.3 Activation Energy of Fe Diffusion into MgB_2

Activation energy can be calculated only for temperature dependence of Fe diffusion. The diffusion coefficient of the Fe varies with the sintering temperature and sintering time. The annealing temperature of 900°C that is more effective compared to other sintering temperatures, that's why we carried out experiments for time dependence of Fe diffusion at 900°C. Fe diffusion into the bulk MgB_2 superconductor depends strongly on the diffusion sintering temperature and time. The mean values of the diffusion coefficients of Fe coated MgB_2 as a function of temperature are given in Figure 5.32.

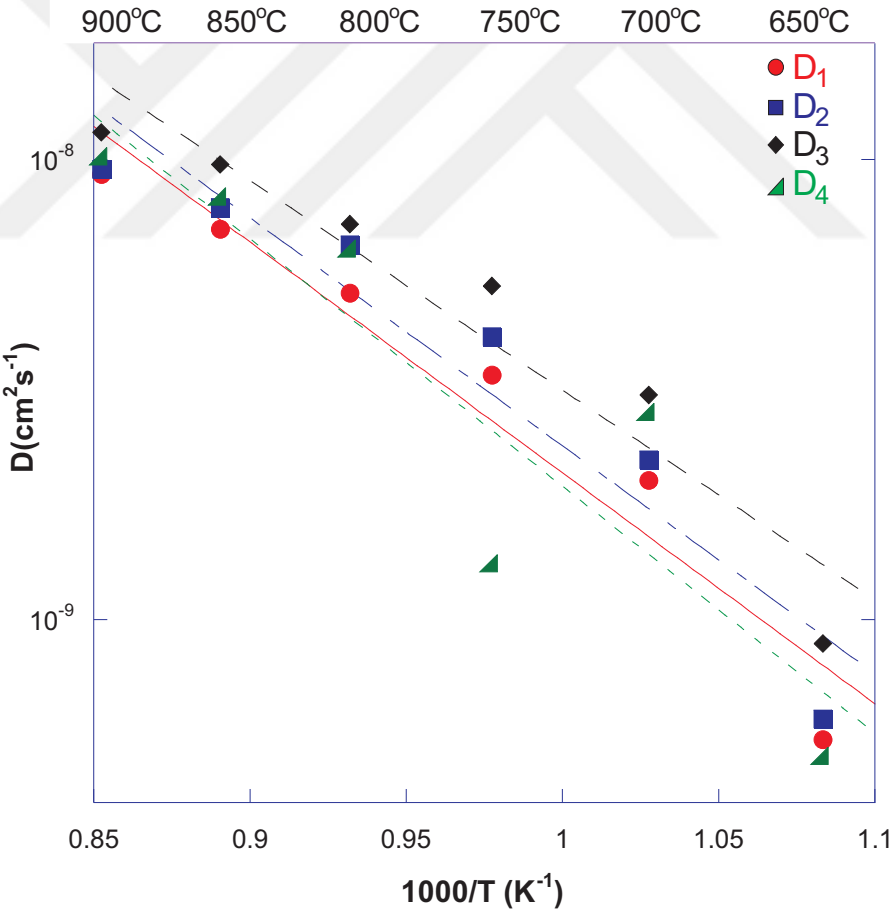

Figure 5.32. Dependence of diffusion coefficient on sintering temperature.

Based on the results given in Table 5.10, Fe diffusion in MgB_2 superconductor depends strongly on the diffusion-annealing temperature and sintering at 650°C is insufficient for diffusion. $D_{(1)}$, $D_{(2)}$, $D_{(3)}$ and $D_{(4)}$ express the Arrhenius relation between activation energies and diffusion coefficients which were calculated for lattice parameter c and room temperature resistivity values.

The results of these studies showed that the Fe diffusion coefficient for MgB_2 bulk superconducting in the temperature range $650-900$°C increases in accordance with the Arrhenius relation;

$$D_{(1)} = 2.18\times10^{-4}\exp\Big(\frac{-0.990\pm0.01eV}{\mathrm{k_B T}}\Big),$$

$$D_{(2)} = 2.16\times10^{-4}\exp\Big(\frac{-0.983\pm0.01eV}{\mathrm{k_B T}}\Big),$$

$$D_{(3)} = 1.14\times10^{-4}\exp\Big(\frac{-0.904\pm0.01eV}{\mathrm{k_B T}}\Big),$$

$$D_{(4)} = 1.63\times10^{-4}\exp\Big(\frac{-1.067\pm0.01eV}{\mathrm{k_B T}}\Big).$$

These relations are seen in Figure 5.32 as lines approximated from measured diffusion coefficients given in Table 5.10. Also, $D_{(1)}$, $D_{(2)}$, $D_{(3)}$ and $D_{(4)}$ express activation energies values 0.99, 0.983, 0.904 and 1.067 eV, respectively. The low activation energies may be related with individual Fe atoms migrating into the bulk of MgB_2 samples through the defects such as inner surfaces of voids and grain boundaries, slightly changing the lattice parameter c (Ulgen and Belenli, 2016a).

Diffusion rate depends on the number of vacancy-like defects in the crystal structure, temperature and activation energy.

6. CONCLUSION

In this work the effect of Fe diffusion on MgB_2 superconductor bulk samples has been studied. The critical transition temperature of bulk samples was improved by a 50 micron Fe coating and diffusion. The diffusion coefficients and activation energies of Fe diffusion into the MgB_2 bulk samples are inferred from the lattice parameters calculated with the aid of the XRD patterns and resistivity measurements along the depth profile.

The *c* parameter of the unit cell increases with coating/diffusion of Fe and *c* value is bigger in Fe diffused samples compared to bare samples. The Fe coated MgB_2 samples have slightly larger grain size of 300 $\AA$ with up to 10% increase compared to bare samples. Increasing of sintering temperature causes the diffusion coefficient and the grain size to increase.

T_c values of Fe coated/diffused samples were found to be higher than that of bare samples prepared under same conditions. Besides, the room temperature resistivity values increase with Fe diffusion in MgB_2 bulk samples.

Fe diffusion into bulk MgB_2 was monitored with changes in lattice parameter c and room temperature resistivity. We have determined the Fe diffusion coefficient in MgB_2 superconductor samples using these two techniques. Fe diffuses with an activation energy of highest 1.067 $\pm$0.001 eV in the temperature range $650-900^{\circ}$C. Relatively low activation energy values of Fe diffusion into MgB_2 may be attributes to Fe atoms easily diffusing through defects in the polycrystalline samples.

Fe diffusion coefficient spans between $5.0561\text{x}10^{-10}\text{cm}^2/\text{s}$ and $1.0179\text{x}10^{-8}\text{cm}^2/\text{s}$ for different sintering temperatures. As a result, diffusion Fe in solid MgB_2 superconducting materials is very slow process and it has a strong temperature dependence.

The diffusion coefficient is a sintering time dependent phenomenon. We have determined the Fe diffusion coefficient in MgB_2 to be between $9.3032\text{x}10^{-9}\text{cm}^2/\text{s}$ and $5.8636\text{x}10^{-8}\text{cm}^2/\text{s}$ for different sintering time durations. The diffusion coefficient decreases with increasing sintering time. We have shown that resistivity measurements can be utilized for determination of diffusion coefficient for Fe diffusion in bulk MgB_2.

The main interaction between the superconducting MgB_2 material and Fe is of diffusion nature and can not be achieved below a certain temperature without allocation of very long durations. Since diffusion coefficient increases with rising annealing temperature and decreases with increasing sintering time, heat treatment processes for Fe clad superconductors should be considered comprehensively.

MgB_2 bulk and wire/tape samples with high performances can be produced by sintering at low-temperatures for longer duration provided that the process is optimized.

REFERENCES

Abdullaev GB, Dzhafarov TD (1987) "Atomic diffusion in semiconductor structures", Harwood, New York.

Abe H, Nishida K, Imai M, Kitazawa H, Yoshii K (2004) "Superconducting properties of MgB_2 films electroplated to stainless steel substrates", Applied physics letters, 85:6197.

Abrikosov AA (1957) "On the magnetic properties of superconductors of the second group", Soviet Physics JETP, 5:1174.

Akdogan M, Yetis H, Gajda D, Karaboga F, Ulgen AT, Demirturk E, Belenli I (2015) "Effect of the initial filling density on the critical current of in-situ Fe/MgB_2 wires", Journal Of Alloys And Compounds, Vol:649:1007-1010.

Altin S, Aksan MA, Yakinci ME (2011) "MgB_2 fabrication by diffusion-controlled three layered (B-Mg-B) technique", Journal of Physics and Chemistry of Solids, 72(9):1070-1076.

Ansari IA, Shahabuddin M, Alzayed NS, Ziq KA, Salem AF, Awana VPS, Kishan H (2013) "Enhancement of critical current density for nano (n)-ZnO doped MgB_2 superconductor", PHYSICA C, Volume: 495:208-212.

Arrhenius, SA (1889) "Influence of temperature on the rate of inversion of sucrose", Z Phys. Chem., 4:226.

Arzt E (1998) "Size effects in materials due to microstructural and dimensional constraints: a comparative review", Acta materialia, 46(16):5611-5626.

Avaeva I, Kravchenko V (1972), Izvestija Akad. Nauk SSSR, 8(N7):1330.

Balluffi RW, Allen S, Carter WC (2005) "Kinetics of materials", John Wiley.

Bardeen J, Cooper LN, Schrieffer JR (1957) "Theory of superconductivity", Physical Review, 108(5):1175.

Bardeen J, Herring CI (1951) "Atom movements", Cleveland, OH:The American Society for Metals, 87.

Barth C (2013) "High Temperature Superconductor Cable Concepts for Fusion Magnets", KIT Scientific Publishing, Germany.

Bauer M, Heidernatsch M, Tauber D, von Borczyskowski C, Radons G (2009) "Investigations of heterogeneous diffusion based on the probability

density of scaled squared displacements observed from single molecules in ultra-thin liquid films", Diffusion Fundamentals Journal, Vol.11:104(14).

Bhatia M, Sumption MD, Tomsic M, Collings EW (2004) "Influence of heat-treatment schedules on the transport current densities of long and short segments of superconducting MgB_2 wire", Physica C, Superconductivity, 407(3):153-159.

Bednorz JG, Muller KA, (1986) "Possible highTc superconductivity in the Ba-La-Cu-O system", Z.Phys.B 64(1):189-193.

Bretz EA (2004) "Superconductors on the high seas", IEEE Spectrum 41:52.

Buzea C, Yamashita T, (2001) "Review of the superconducting properties of MgB_2", Supercond.Sci.Technol. 14:R115-R146.

Canfield PC, Finnemore DK, Bud'Ko SL, Ostenson JE, Lapertot G, Cunningham CE, Petrovic C (2001) "Superconductivity in dense MgB_2 wires", Physical Review Letters, 86(11):2423.

Chen W, Liu W, Chen C, Wang R, Feng Q, (2011) "Single-crystal MgB_2 hexagonal microprisms via hybrid physical-chemical vapor deposition", Cryst.Eng.Comm, 13(12):3959-3961

Chen XH, Wu T, Wu G, Liu RH, Chen H, Fang DF (2008) "Superconductivity at 43 K in SmFeAsO1-xFx", Nature, 453(7196):761-762.

Crank J (1975) "The Mathematics of Diffusion", 2nd edn, Clarendon, Oxford.

DeFouw JD, Quintana JP, Dunand DC, (2008) "In situ X-ray synchrotron diffraction study of MgB_2 synthesis from elemental powders", Acta Materialia, 56(8):1680-1688.

De Lima OF, Ribeiro RA, Avila MA, Cardoso CA, Coelho AA (2001) "Anisotropic superconducting properties of aligned MgB_2 crystallites", Physical review letters, 86(26):5974.

Devadas KM (2015) "Studies on development of MgB_2 based Superconducting current leads", Doctor of Philosophy in Physics, National Institute for Interdisciplinary Science and Technology (CSIR), Trivandrum.

Dogruer M, Zalaoglu Y, Gorur O, Ozturk O, Yildirim G, Varilci A, Terzioglu C (2013) "Influence of diffusion-annealing temperature on physical and mechanical properties of Cu-diffused bulk MgB_2 superconductor", Journal of Materials Science, Materials in Electronics, 24(2):776-783.

Dogruer M, Zalaoglu Y, Yildirim G, Varilci A, Terzioglu C (2013) "Effect of diffusion-annealing time on the mechanical and superconducting properties of Cu-diffused bulk MgB_2 superconductors by use of experimental and different theoretical models", Journal of Materials Science: Materials in Electronics, 24(6):2019-2026.

Dou SX, Soltanian S, Zhao Y, Getin E, Chen Z, Shcherbakova O, Horvat J (2005) "The effect of nanoscale Fe doping on the superconducting properties of

MgB_2", Superconductor Science and Technology, 18(5):710.

Dou SX, Shcherbakova O, Yeoh WK, Kim JH, Soltanian S, Wang XL, Senatore C, Flukiger R, Dhalle M, Husnjak O, Babic E (2007), Physical Review Letters, 98, 097002.

Du W, Xu D, Zhang H, Wang X, Zhang G, Hou X, Liu H, Wang Y (2004) "Single crystal growth of MgB_2 by using Mg-self-flux method at ambient pressure", Journal of Crystal Growth, 268:123-127.

Dzhafarov TD, Cömert H, Altunbas M, Küçükoğlulu T, Kopya A (1995) "Diffusion of Ag in Bi(Pb)-Sr-Ca-Cu-O superconductors", Journal of Alloys and Compounds 221:264-266.

Dzhafarov TD (1997) "Diffusion in High-Temperature Superconductors", physica status solidi (a), 158(2):335-358.

Einstein A (1905) "Does the inertia of a body depend upon its energy-content", Annalen der Physik, 18(13):639-641.

Einstein A (1906) "Eine neue bestimmung der moleküldimensionen", Annalen der Physik, 324(2):289-306.

Eisterer M, Zehetmayer M, Weber HW (2003) "Current Percolation and Anisotropy in Polycrystalline MgB_2", Physical review letters, 90(24):247002.

Eom CB, Lee MK, Choi JH, Belenky LJ, Song X, Cooley LD, Naus MT, Patnaik S, Jiang J, Rikel M, Polyanskii A, Gurevich A, Cai XY, Bu SD, Babcock SE, Hellstrom EE, Larbalestier DC, Rogado N, Regan KA, Hayward MA, He T, Slusky JS, Inumaru K, Haas MK, Cava RJ (2001), Nature 411:558.

Fagaly RL (2006) "Superconducting quantum interference device instruments and applications", Rev. Sci. Instrum. 77:101101.

Falk B, Garramone S, Shivkumar S (2004) "Diffusion coefficient of paracetamol in a chitosan hydrogel" Materials Letters, 58(26):3261-3265.

Fick A (1855), Annalen der Physik und Chemie 94:59.

Finnemore DK, Ostenson JE, Bud'Ko SL, Lapertot G, Canfield PC (2001) "Thermodynamic and transport properties of superconducting $Mg^{10}B_2$", Fischer C, Habler W, Roding C, Perner O, Behr G, Schubert M, Nenkov K, Eckert J, Holzapfel B, Schultz L (2004) "Critical current densities of superconducting MgB_2 tapes prepared on the base of mechanically alloyed precursors", Physica C, 406:121.

Fofanov D (2009) "Synthesis, characterization and physical properties of metal borides". Physical review letters, 86(11):2420.

Frenkel JI (1926) "Thermal agitation in solids and liquids" Z Physic, 35:652-669.

Gao J (2013) "Time dependent chloride diffusion coefficient in concrete", Journal of Wuhan University of Technology-Mater. Sci. Ed., 28(2):314-319.

Gibbons JH (1983) "U.S. Passenger Rail Technologies", Washington, D.

C.: U.S. Congress, Office of Technology Assessment, OTA-STI-222.

Ginzburg VL, Landau LD, (1950), Zh. Eksp.i Teor.Fiz.(Rus.) 20:1064.

Giunchi G, Ripamonti G, Cavallin T, Bassani E (2006) "The reactive liquid Mg infiltration process to produce large superconducting bulk MgB_2 manufacts", Cryogenics, 46(2):237-242.

Glowacki BA, Majoros M, Vickers M, Evetts JE, Shi Y, McDougall I (2001) "Superconductivity of powder-in-tube MgB_2 wires", Superconductor Science and Technology, 14(4):193.

Goretta KC, Chen N, Lanagan MT, Wu W, Singh JP, Olson RA, Routbort JL, Poeppel RB (1992) "In Advances in Power Metallurgy", Properties of Emerging P/M Materials, Vol8:271.

Goretta K, Chen N, (2000) "Diffusion and Heat Treatment of High Temperature Superconductors", In Superconducting Materials: Advances in Technology and Applications:218-228.

Gorur O, Terzioglu C, Varilci A, Altunbas M (2005) "Investigation of some physical properties of silver diffusion-doped Y123 superconductors", Superconductor Science and Technology, 18(9):1233.

Gorur O, Küçükömeroglu T, Terzioglu C, Varilci A, Altunbas M (2005) "The effect of Ag diffusion on properties of YBa 2 Cu 3 O 7- x thin films produced by electron beam deposition techniques", Physica C, Superconductivity, 418(1):35-42.

Grasso G, Malagoli A, Ferdeghini C, Roncallo S, Braccini V, Siri AS, Cimberle MR (2001) "Large transport critical currents in unsintered MgB_2 superconducting tapes", Applied Physics Letters, 79:230.

Grathwohl P (1998) "Diffusion in natural porous media: contaminant transport, sorption/desorption and dissolution kinetics", Kluwer Academic, Dordrecht.

Grey HJ, Isaacs A (1991) "Dictionary of Physics", 3rd ed., edited Longman, Singapore.

Groh J, von Hevesy G (1920) "Die Selbstdiffusionsgeschwindigkeit des geschmolzenen Bleis", Ann. Physik 63:85.

Groh J, von Hevesy G (1921) "Die Selbstdiffusion in festem Blei", Ann. Physik 65:216.

Gurevich A (2007) "Limits of the upper critical field in dirty two-gap superconductors", Physica C, 456:160.

Habler W, Birajdar B, Gruner W, Herrmann M, Penner O, Roding C, Schubert M, Holzapfel B, Eibl O, Schultz L (2006) "MgB_2 bulk and tapes prepared by mechanical alloying: influence of the boron precursor powder", Superconductor Science and Technology, 19, 512.

Habler W, Herrmann M, Rodig C, Schubert M, Nenkov K, Holzapfel B (2008) "Further increase of the critical current density of MgB_2 tapes with

nanocarbon-doped mechanically alloyed precursor", Superconductor Science and Technology, 21: 062001.

Heitjans P, Karger J (2005) "Diffusion in Condensed Matter", Düsseldorf: Springer.

Heumann T, Walther G (1957) "Der Kirkendall-Effekt in Silber-Gold-Legierungen im gesamten Konzentrationsbereich", ZEITSCHRIFT FUR METALLKUNDE, 48(4): 151-157.

Hoffman RE, Turnbull D (1951) "Lattice and Grain Boundary Self-Diffusion in Silver", J. Appl. Phys. 22:634.

Holübek T (2008) "Current transfer and thermal stability of composite MgB_2 superconductors", Ph.D Thesis, Slovak Academy of Sciences, Slovak Republic:16.

Hott R, Kleiner R, Wolf T, Zwicknagl G (2005) "Frontiers in Superconducting Materials", (Editor:A. V. Narlikar) Springer-Verlag Berlin Heidelberg.

Iavarone M, Karapetrov G, Koshelev AE, Kwok WK, Crabtree GW, Kang WN, Choi EM, Kim HJ, Lee SI (2004) "STM tunnelling spectroscopy in MgB_2 thin films: the role of band structure in tunnelling spectra", Supercond. Sci. Technol. 17:106.

Jaklevic RC, Lambe J, Silver AH, Mercereau JE (1964) "Quantum interference effects in Josephson tunneling", Physical Review Letters, 12(7):159.

Jiang CH, Hatakeyama H, Kumakura H (2005) "Effect of nanometer MgO addition on the in situ PIT processed MgB_2/Fe tapes", Physica C, 423: 45.

Jiang J, Senkowicz BJ, Larbalestier DC, Hellstrom EE (2006) "Influence of boron powder purification on the connectivity of bulk MgB_2" Superconductor Science and Technology, 19(8):L33.

Jiang CH, Dou SX, Cheng ZX, Wang XL (2008) "Light carbon doping by oxygen-free paraffin wax to enhance the current density of MgB_2 in the entire field regime", Superconductor Science and Technology, 21(6):065017.

Jiang J, Senkowicz BJ, Larbalestier DC, Hellstrom EE (2006) "Influence of boron powder purification on the connectivity of bulk MgB_2", Superconductor Science and Technology, 19(8):L33.

Jones ME, Marsh RE (1954) "The Preparation and Structure of Magnesium Boride, MgB_2", Journal of the American Chemical Society 76(5):1434.

Joubert J, Shirk T (1968) "Stability, infrared spectrum and magnetic properties of $FeBO_3$", Mat. Res. Bull., 3:671.

Karpinski J, Zhigadlo ND, Katrych S, Puzniak R, Rogacki K, Gonnelli R (2007) "Single crystals of MgB_2: synthesis, substitutions and properties" Physica C: Superconductivity, 456(1):3-13.

Kim KHP, Choi JH, Jung CU, Chowdhury P, Lee HS, Park MS, Kim HJ, Kim JY, Du Z, Choi EM, Kim MS, Kang WN, Lee SI, Sung GY, Lee JY

(2002)"Superconducting porperties of well-shaped MgB_2 single crytals", Phys. Rev. B, 65:100510.

Kim JH, Yeoh WK, Qin MJ, Xu X, Dou SX, Munroe P, Jiang CH (2006) "Enhancement of in-field Jc in MgB_2/Fe wire using single and multi-walled nanotubes", arXiv preprint cond-mat/0607540.

Kim JH, Oh S, Heo YU, Hata S, Kumakura H, Matsumoto A, MacManus-Driscoll JL (2012) "Microscopic role of carbon on MgB_2 wire for critical current density comparable to NbTi", NPG Asia Materials, 4(1):e3.

Korkus J, Mazin II, Belashchenko KD, Antrapov PV, Boyer LL (2001) "Superconductivity of metallic boron in MgB_2", Phys. Rev. Lett. 86:4656.

Kovac P, Husek I, Skakalova V, Meyer J, Dobrocka E, Hirscher M, Roth S (2007) "Study of MgO formation and structural defects in in situ processed MgB_2/Fe wires", Supercond. Sci. Technol., 20: 150.

Kumakura H, Matsumoto A, Fujii H, Kitaguchi H, Togano K (2002) "Microstructure and superconducting properties of powder-in-tube processed MgB_2 tapes." Physica C: Superconductivity, 382(1):93-97.

Kumakura H, Matsumoto A, Nakane T, Kitaguchi H (2007) "Fabrication and properties of powder-in-tube-processed MgB_2 tape conductors", Physica C 456: 196.

Larbalestier D, Gurevich A, Feldmann DM, Polyanskii A (2001) "High-Tc superconducting materials for electric power applications", NATURE, VOL414.

Laughlin DE, Hono K, (2014) " Physical Metallurgy, 5th Edition: 3-Volume Set". Elsevier, Waltham, USA.

Lee S, (2003) "Crystal growth of MgB_2", Physica C, vol:385, no1-2:31-41.

Leiro JA, Kokko K, Kulmala V (2004) "Polarization dependent X-ray spectra of MgB_2", Journal of Alloys and Compounds 362:139-142.

Li J, Lin H, Chen Y, Su Q, Huang Q (2011) "The effect of iron oxide on the formation of boron nitride nanotubes" Chemical Engineering Journal, 174(2):687-692.

Liu ZK, Schlom DG, Li Q, Xi XX (2001) "Thermodynamics of the Mg-B system: Implications for the deposition of MgB_2 thin films", Applied Physics Letters, 78(23):3678-3680.

Liu CF, Yan G, Du SJ, Xi W, Feng Y, Zhang PX, Wu XZ, Zhou L (2003) "Effect of heat-treatment temperatures on density and porosity in MgB_2 superconductor", Physica C:Superconductivity, 386:603.

London F, London H (1935) "The electromagnetic equations of the supraconductor", Proc. Roy. Soc., A149:71.

Loskutov VV (2012) "Empirical time dependence of liquid self-diffusion coefficient in porous media", Journal of Magnetic Resonance, 216:192-196.

Lubkin GB (1996) ”Power applications of high-temperature superconductors”, Physics Today, 49(3).

Maeda H, Tanaka Y, Fukutomi M, Asano T (1988) ”A new high-Tc oxide superconductor without a rare earth element”, Japanese Journal of Applied Physics, 27(2A):L209.

Malagoli A, Braccini V, Bernini C, Romano G, Vignolo M, Putti M, Ferdeghini C (2010), Superconductor Science and Technology, 23:025032.

Massalki T (1990) ”Binary Alloy Phase Diagrams”, A.S.M. International, Materials Park, OH.

Matthias BT, Geballe TH, Geller S, Corenzwit E (1954) ”Superconductivity of Nb_3Sn”, Physical Review, 95(6):1435.

Mehrer H (2007) ”Diffusion in Solids: Fundamentals, Methods, Materials, Diffusion-Controlled Processes” Berlin: Springer-Verlag.

Meissner W, Ochsenfeld R (1933) ”Ein neuer effekt bei eintritt der supraleitfahigkeit”, Naturwissenschaften, 21(44):787-788.

Mueller M, Polinder H (2013) ”Electrical Drives for Direct Drive Renewable Energy Systems (Woodhead Publishing Series in Energy)”, Woodhead Publishing, Ltd., Cambridge, UK.

Mustapic M, Pajic D, Novosel N, Babic E, Zadro K, Cindric M, Shcherbakov A (2010) ”Synthesis, structural characterization and magnetic properties of iron boride nanoparticles with or without silicon dioxide coating”, Croatica chemica acta, 83(3):275-282.

Nagamatsu J, Nakagawa N, Muranaka T, Zenitani Y, Akimitsu J (2001) ”Superconductivity at 39 K in magnesium diboride”, Nature, 410(6824):63-64.

Novosel N, Pajic D, Mustapic M, Babic E, Shcherbakov A, Horvat J, Zadro K (2010) ”Flux pinning and inhomogeneity in magnetic nanoparticle doped MgB_2/Fe wires”, In Journal of Physics: Conference Series, Vol. 234, No. 2:022027.

Novosel N, Pajic D, Skoko Z, Mustapic M, Babic E, Zadro K, Horvat J (2012) ”The Influence of $CuFe_2O_4$ Nanoparticles on Superconductivity of MgB_2”, Physics Procedia, 36:1498-1503.

Onnes HK (1911), Commun. Phys. Lab. Univ. Leiden. Suppl. 29.

Onnes HK (1913) ”Heike Kamerlingh Onnes-Nobel Lecture”, Nobelprize.org. http://www.nobelprize.org/nobel_prizes/physics/laureates/1913/onnes-lecture.html

Ozturk O, Asikuzun E, Kaya S, Coskunyurek M, Yildirim G, Yilmazlar M, Terzioglu C (2012) ”Physical Properties and Diffusion-Coefficient Calculation of Iron Diffused Bi-2223 System”, Journal of superconductivity and novel magnetism, 25(7):2481-2487.

Pachla W, Presz A, Kovac P, Husek I, Diduszko R (2004) "Structural characterization of multifilament heat treated ex situ MgB_2 superconducting wires with Cu and Fe sheaths", Superconductor Science and Technology, 17(11):1289.

Pachla W, Kovac P, Husek I, Melisek T, Müler M, Strbik V, Mazur A, Presz A (2005) "The effect of hydrostatic extrusion on the Jc(B) characteristic of ex situ MgB_2 wires", Superconductor Science and Technology, 18:552.

Pan AV, Zhou S, Liu HK, Dou SX (2003) "Effect of the processing parameters of $MgB_{1.8}(SiC)_{0.1}$/Fe tapes on the critical current density", Superconductor Science and Technology, 16:639.

Pan AV, Dou SX (2004) "Overcritical state in superconducting round wires sheathed by iron", J. Appl. Phys., 96, 1146.

Petaccia L, Cepek C, Lizzit S, Larciprete R, Macovez R, Sancrotti M, Goldoni A (2006) "Characterization of high-quality $MgB_2(0001)$ epitaxial films on Mg(0001)", New Journal of Physics, Vol 8:12.

Prabitha VG, Biju A, Kumar RGA, Sarun PM, Aloysius RP, Syamaprasad U (2005) "Effect of Sm addition on (Bi,Pb)-2212 superconductor", Physica C, 433: 28.

Prikhna T, Gawalek W, Savchuk Y, Sergienko N, Moshchil V, Dub S, Sverdum V, Kovalev L, Penkin V, Zeisberger M, Wendt M, Fuchs G, Habisreuther T, Litzkendorf D, Nagorny P, Melnikov V (2007) "High-pressure-high-temperature synthesis of magnesium diboride with different additions", Physica C, 460: 595.

Putti M, Braccini V, Galleani E d'Agliano, Napoli F, Pallecchi I, Siri AS, Manfrinetti P, Palenzona A (2003) "Thermal conductivity of MgB_2 in the superconducting state", Phys. Rev. B 67:064505.

Radebaugh R, Keesom PH (1965), Bull. Amer. Phys. Soc. J0:358.

Roberts-Austen WC (1896) "Bakerian Lecture on the Diffusion in Metals", Phil. Trans. Roy. Soc. A 187:383.

Rogalla H, Kes PH (2011) "100 Years of Superconductivity", CRS Press, London, New York, p355.

Routbort JL, Chen N, Goretta KC, Rothman SJ (1991) "in High Temperature Superconductors: Materials Aspects", Edited by H.C.Freyhardt, R.Flükiger and M.Peuckert (DGM Informations, Oberursel, Germany.) p.569.

Rowell JM (2003) "The widely variable resistivity of MgB_2 samples", Sup. Sci. and Tech. 16:R17-R27.

Samuely P, Szabo P, Pribulova Z, Angst M, Bud'ko SL, Canfield PC, Kang BW (2007) "Aluminum and carbon substitution in MgB_2", Electron doping and scattering effects. Physica C: Superconductivity and its applications, 460:84-88.

Saritekin NK, Dogruer M, Yildirim G, Terzioglu C (2014) "Research on MgB_2 bulk superconductors exposed to Ag nanoparticles diffusion." Journal of Materials Science: Materials in Electronics, 25(7):3127-3136.

Schilling A, Cantoni M, Guo JD, Ott HR (1993) "Superconductivity above 130 K in the Hg-Ba-Ca-Cu-O system", Nature, 363(6424):56-58.
Schmauch J, Markmann J, Grewer M, Birringer R, (2009) "Determination of grain size and grain size distributions from the nano to the micro scale by means of EBSD", MC2009:I5.P522.

Schneider T, Castro DD (2005) "Pressure and isotope effect on the anisotropy of MgB_2", Physical Review B, 72, 054501.

Shcherbakova O, Dou SX, Soltanian S, Wexler D, Bhatia M, Sumption M, Collings EW (2006) "Identification of factors limiting the critical current density in $MgB_{2-x}C_x$ superconductors at low magnetic fields", Journal of Applied Physics 99: 08M510.

Senkowicz BJ, Moyet RP, Mungall RJ, Hedstrom J, Uwakwch ONC, Hellstrom EE, Larbalestier DC (2006) "Atmospheric conditions and their effect on ball-milled magnesium diboride", Supercond. Sci. Technol., 19, 1173.

Simsek T, Baris M, Akkurt A (2014) "Mechanochemical Synthesis of Pure Fe_2B Nanoparticles".

Stefan J (1879) Sitzungsberichte d. Kaiserl. Akad. d. Wissenschaften II 79:161-214.

Stromberg TF, Swenson CA, (1962) "Negative Surface Free-Energy Effects in Superconducting Niobium", Phys. Rev. Letters 9:370.

Suo HL, Lezza P, Uglietti D, Beneduce C, Abacherli V, Flukiger R (2003) "Transport critical current densities and n factors in mono-and multifilamentary MgB_2/Fe tapes and wires using fine powders", IEEE Trans. Appl. Supercond., 13: 3265.

Takahashi H, Igawa K, Arii K, Kamihara Y, Hirano M, Hosono H (2008) "Superconductivity at 43 K in an iron-based layered compound LaO1-xFxFeAs" Nature, 453(7193):376-378

Takano Y, Takeya H, Fujii H, Kumakura H, Hatano T, Togano K, Kito H, Ihara H (2001) "Superconducting properties of MgB_2 bulk materials prepared by high pressure sintering", Appl. Phys. Lett. 78:2914.

Tarantini C, Aebersold HU, Braccini V, Celentano G, Ferdeghini C, Ferrando V, Gambardella U, Gatti F, Lehmann E, Manfrinetti R, Marr D, Palenzona A, Pallecchi I, Sheikin I, Siri AS, Putti M (2006) "Effects of neutron irradiation on polycrystalline $Mg^{11}B_2$", Physical Review B, 73:134518.

Terzioglu C, Ozturk O, Belenli I (2009) "The effect of Au diffusion on some physical properties of Bi2223 superconductors." Journal of Alloys and Compounds, 471(1):142-146.

Tobin JR (2008) "Superconductivity Research Developments", Nova Science Publishers Inc, ISBN-10: 1600218482, pp-248.
Turkevich VZ, Kulik OG, Itsenko PP, Sokolov AN, Lutsenko AN, Vashchenko AN (2003) "Phase diagram of the Mg-B system at high pressures", Sverkhtverdye Materialy, (1):9-14.

Ueda S, Shimoyama JI, Iwayama I, Yamamoto A, Katsura Y, Horri S, Kiskio K (2005) "High critical current properties of MgB_2 bulks prepared by a diffusion method", Applied Physics Letters, 86(22):2502.

Ulgen AT, Belenli I (2016) "Effect of Pressing & Annealing on Superconducting Properties of in-situ Processed MgB_2/Fe Monofilament Wires", Superconducting Materials on Their Way from Physics to Applications Seminar.

Ulgen AT, Belenli I (2016a) "The Effect of Fe Diffusion on Some Physical and Superconducting Properties of MgB_2", Journal of Superconductivity and Novel Magnetism, DOI: 10.1007/s10948-016-3780-z

Ulgen AT, Belenli I (2016b) "Time Dependent Diffusion Coefficient of Fe MgB_2 Superconductors", Journal of Materials Science: Materials in Electronics, under-review no: JMSE-D-16-03266.

Vinod K, Varghese N, Syamaprasad U (2007) "Superconductivity of MgB_2 in the BCS framework with emphasis on extrinsic effects on critical temperature", Supercond. Sci. Technol. 20:R31-R45.

Wagner C, Schottky W (1930) "Theorie der geordneten Mischphasen", Z. Phys. Chem. B 11: 163

Wang XL, Soltanian S, James M, Qin MJ, Horvat J, Yao QW, Liu HK, Dou SX (2004) "Significant enhancement of critical current density and flux pinning in MgB_2 with nano-SiC, Si, and C doping", Physica C, 408:63.

Warren BE (1990) "X-ray diffraction", Chapter 13, p251, Dover Publications, New York.

Werner M, Mehrer H (1983) in: DIMETA-82, "Diffusion in Metals and Alloys, F.J. Kedves, D.L. Beke (Eds.), Trans Tech Publications, Diffusion and Defect Monograph Series No.7:392.

West AR (1999) "Basic Solid State Chemistry, John Wiley & Sons.

Wollenberger HJ (1996) "In: Physical Metallurgy, part 2, ed" by R.W. Cahn, P. Haasen, North Holland, Amsterdam.

Wu MK, Ashburn JR, Torng CJ (1987) "Superconductivity at 93-k in a new mixed-phase y- ba-cu-o compound system at ambient pressure", Physical Review Letters, 58(9):908-910.

Xi XX, (2008) "Two-band superconductor magnesium diboride", Rep. Prog. Phys., 71:116501.

Xu X, Kim JH, Dou SX, Choi S, Lee JH, Park HW, Rindfleish M, Tomsic M (2009) "A correlation between transport current density and grain connectivity in MgB_2/Fe wire made from ball-milled boron", Journal of Applied Physics 105:103913.

Xu M, Kitazawa H, Takano Y, Ye J, Nishida K, Abe H, Matsushita A, Tsuji N, Kido G (2001) "Anisotropy of superconductivity from MgB_2 single crystals", Appl. Phys. Lett., 79:2779.

Yamada H, Hirakawa M, Kumakura H, Kitaguchi H (2006) ”Effect of aromatic hydrocarbon addition on in situ powder-in-tube processed MgB_2 tapes”, Superconductor Science and Technology, 19(2):175.

Yamamoto A, Shimoyama J, Ueda S, Katsura Y, Iwayama I, Horii S, Kishio K (2005) ”Universal relationship between crystallinity and irreversibility field of MgB_2”, Applied Physics Letters, 86, 212502.

Yeoh WK, Horvat J, Kim JH, Xu X, Dou SX (2007) ”Effect of processing temperature on high field critical current density and upper critical field of nanocarbon doped MgB_2”.

Zhang Y, Xu X, Zhao Y, Kim JH, Lu C, Zhou SH, Dou SX (2008) ”Significant improvement of Jc in MgB_2 bulk superconductor using ball-milled high-purity crystalline boron”, Superconductor Science and Technology, 18:1473.

Zhi-An R, Wei L, Jie Y, Wei Y, Xiao-Li S, Guang-Can C, Zhong-Xian Z (2008)”Superconductivity at 55 K in iron-based F-doped layered quaternary compound Sm [O1-xFx] FeAs”, Chinese Physics Letters, 25(6):2215.

Zhou S, Dou S (2010) ”Properties of MgB_2 bulks after combined doping with Fe and C by adding Iron (II) lactate ($C_6H_{10}FeO_6$)”, Solid State Sciences, 12(1):105-110.

CURRICULUM VITAE

Asaf Tolga ÜLGEN

Address:

Abant İzzet Baysal University

Department of Physics

14280 Bolu, Turkey

Phone: +90 374 2541000

Fax: +90 374 2534642

Email: ulgen_at@ibu.edu.tr & asaftolgaulgen@gmail.com

Personal Details:

Gender: Male

Date of Birth: May 24th, 1984

Place of Birth: Mersin, Turkey

Education:

2003-2007 Undergraduate Studies in Physics at the Gaziosmanpaşa University

2007-2010 MSc in Physics at the Gaziosmanpaşa University

MSc Thesis: Calculation of Macroscopic State Equations in Blume Capel Model by Using Time-Series Methods

2010-2016 PhD in Physics at the Abant İzzet Baysal University

PhD Thesis: The Diffusion of Iron in the Superconducting MgB_2 Polycrystalline Solid Samples

Publications:

- **Asaf Tolga Ulgen** and İbrahim Belenli, (2016). ”Time Dependent Diffusion Coefficient of Fe/MgB_2 Superconductor”, ournal of Materials Science: Materials in Electronics, under-review no: JMSE-D-16-03266.

- **Asaf Tolga Ulgen** and İbrahim Belenli, (2016). ”The Effect of Fe Diffusion on Some Physical and Superconducting Properties of MgB_2”, Journal of Superconductivity and Novel Magnetism, DOI: 10.1007/s10948-016-3780-z.

- **Asaf Tolga Ulgen** and İbrahim Belenli, (2016). ”Sintering Time Dependence of Iron Diffusion in MgB_2 and Its Effect on Superconducting Properties”, The American Institute of Physics (AIP) Turkish Physics Society 32th International Physics Congress Series.

- M. Akdogan, H. Yetis, D. Gajda, F. Karaboga, **A. T. Ulgen**, E. Demirturk, and İ. Belenli, (2015). ”Effect of the Initial Filling Density on the Critical Current of insitu Fe/MgB_2 Wires”, Journal of Alloys and Compounds, 649, 15 1007-1010.

- **A. Tolga Ulgen** and N.Sünel, (2013). ”Solution of macroscopic state equations of Blume-Capel model using nonlinear dynamics concepts”, SAU J. Sci. Vol 17, No 1, p. 53-60.

- Y. Zalaoglu, F.Karaboga, G. Yildirim, C. Terzioglu, A. Serol Erturk, and **A. Tolga Ulgen**, (2011). ”Ab Initio Hartree-Fock And Density Functional Theory Study On Characterization Of 2-Nitro-N-(4- Nitrophenyl) Benzamide”, Balkan Physics Letters, 19, 191015, pp. 137-152.

- Y. Zalaoglu, G. Yildirim, **A.T. Ulgen**, B. Guner and C. Terzioğlu, (2011). ”A Characterization Study on 4-Amino-3,5-Dialkyl-1-Triazole by Density Functional

Theory and Ab Initio Hartree-Fock Calculations", ODU Journal of Science and Engineering, Vol-1, Issue 1, pp. 37-50.

- Y. Zalaoglu, **A.T. Ulgen**, C. Terzioğlu and G. Yildirim, 2010. "Theoretical Study On The Characterization Of 6-Methyl 1,2,3,4-Tetrahydroquinoline Using Quantum Mechanical Calculation Methods". SAU J. Sci. Vol 14. No 2, p. 66-76.

Selected Presentations:

- **Asaf Tolga ULGEN** and Ibrahim Belenli, (2016). "The Effect of Fe Diffusion on Structural and Superconducting Properties of MgB_2", 5th International Conference on Superconductivity and Magnetism, 24th-30th April, Fethiye/Turkey.

- **Asaf Tolga ULGEN** and Ibrahim Belenli, (2016). "Effect of Pressing & Annealing on Superconducting Properties of in-situ processed MgB_2/Fe monofilament wires", Superconducting Materials on Their Way from Physics to Applications, 17-20 February, Bad Honnef/Germany.

- F. Karaboga, E. Demirtürk, **A.T. Ulgen**, H.Yetis, M. Akdogan, M. Pakdil and I. Belenli, (2015). "Mechanical properties and uniformity of MgB_2 wires upon various wire drawing steps", The 8th Asian Conference on Applied Superconductivity and Cryogenics, November 22-25, Hangzhou/China.

- E. Demirturk, **A.T. Ülgen**, F. Karaboğa, H. Yetiş, M. Akdoğan, and İ. Belenli, (2015). "Cross Sectional Homogeneity and Inner Surface Smoothness of Iron Sheath in Fe-clad MgB_2 Wires During Drawing Process". 9th International Physics Conference of the Balkan Physical Union, 24-27 August, Istanbul/Turkey.

- **A. T. Ulgen**, M. Akdogan, H. Yetis, F. Karaboga, D. Gajda, E. Demirturk, and I. Belenli, (2015). "Investigation of superconducting properties of in-situ monofilamentary Fe/MgB_2 wires having high critical transport current density", International Conference on Magnetic and Superconducting Materials, 30 April-3 May, Antalya/Turkey.

- **A. Tolga Ulgen** and N.Sünel, (2011). ”Solution of Macroscopic State equations of Blume-Capel Model Using Nonlinear Dynamics Concepts” 28. International Physics Congress, 14-19 September, İstanbul/Turkey.

Workshops and Schools:

- 608. WE-Heraeus-Seminar on ’Superconducting Materials on Their Way from Physics to Applications’, 17-20 February (2016) at the Physikzentrum Bad Honnef/Germany.
- Spring School and Educational Courses on Superconductivity and Magnetism (SSEC2014), April 21st, (2016) Antalya/Turkey.
- Institute of Theoretical and Applied Physics (ITAP), ”Statistical Mechanics and Complexity Summer Course”, (2011) Turunç-Marmaris/Turkey.
- Institute of Theoretical and Applied Physics (ITAP), ”Nonlinear Dynamical Systems: Chaos and Fractal Geometry Summer Course” (2010) Turunç-Marmaris/Turkey.

Projects:

”MgB_2/Fe Parkur Tipi Bobin Tasarımı ve Üretimi”, Tübitak, Proje No. 113F080, 2013-2016.

”Polikristal MgB_2 Süperiletken Katı Örneklere Altın ve Kobalt Difüsyonu”, Abant İzzet Baysal Üniversitesi, Bilimsel Araştıma Projesi no: 2016.03.02.1067.

Working Experience:

2008-2009 Worked as a Student Assistant at the Physics Department of Gaziosmanpaşa University.

2010-2011 Worked as a Teaching Assistant at the Electrical and Electronics Engineering Department of Şırnak University.

2011-2016 Working as a Research Assistant at the Physics Department of Abant Izzet Baysal University.